The Sky as a Laboratory

2011-2012

Project Director
Prof. Piero Rafanelli
Dept. of Physics and Astronomy, Padova University

Scientific Coordinators
Stefano Ciroi
Valentina Cracco
Alessandra Frassati

Project Secretary
Rossella Spiga

Preface

This book collects the final scientific reports of the students, who took part in the observational training periods organized in February 2012 at the Asiago Astrophysical Observatory in the frame of the XI Edition of The Sky as a Laboratory, the educational project of the Department of Astronomy of Padova University, addressed to the Secondary Schools of the Veneto Region (Italy). Created by Prof. Piero Rafanelli and carried out by means of a close cooperation between the scientific and technical staff of the former Dept. of Astronomy, and the teachers of the participating schools, every year this project involves about 300-350 Secondary School students, 40-45 teachers and 35 institutes.

The main aim of The Sky as a Laboratory is to introduce a new approach in teaching and learning astronomy, through the interpretation of the observed celestial phenomena and the use of the physical and mathematical tools available to the students. This project allows the students to deepen the issues studied at school and makes a link among astronomy, physics, mathematics, and chemistry. In addition it guides the students to the university choice, since it allows them to be exposed to the university environment and scientific research.

The first part of the project consists of 7 lectures of fundamentals of astrophysics given by the teachers of the 10 reference schools and by the scientific staff of the Dept. Then, a competitive test allows to select the 50 most eligible and motivated students, who will attend a training period of 3 days and 3 nights at the 122 cm Galileo Telescope of the Asiago Astrophysical Observatory. This training gives the students a chance to deepen the knowledge they acquired during astronomy classes both at school and during the project. In addition, they receive 1 or 2 ECTS from the Science Faculty of Padova University.

The project ended on April 13th, 2012 with the official presentation of the scientific reports by the students at the Dept. of Astronomy.

Il Cielo come Laboratorio, 1
A.S. 2011-2012

Spectral classification of stars in the open cluster 2420

Giacomo Coran, Nicolò Forcellini, Giulio Pegorer

Liceo Scientifico *L. Da Vinci*, Treviso

Abstract. We analyzed the open cluster NGC 2420, classifying the spectra of 351 stars of the cluster through the study of a sample of 30 of them, and obtaining an estimate of the age of the cluster through the analysis of the H-R diagram. In order to classify the spectra of our sample, we normalized them at 5500 Å and compared them to standard stars' spectra we had available, also computing the residuals to understand the reliability of our classification. Then we checked the relation between spectral classes and color index (r-i) and between spectral classes and temperature: our relations were statistically significant and in good agreement with the theory. Then we calculated the temperature of the 351 stars with the relation between temperature and color index (r-i) determined by Affili, Casarin & Maguolo (2012), in this way we were able to build the H-R diagram of the cluster. Lastly, we estimated the age of the cluster using a set of isochrones, with a metallicity Z=0.008, inferring that the age is between 1.58 and 2.8 Gyr.

1. Introduction

Open clusters are groups of stars, kept together by mutual gravitonational forces, that were born at the same time from large cosmic gas and dust clouds in the arms of spiral galaxies or in irregolar galaxies. These clusters have a similar initial composition and their stars are at the same distance from the Earth. Therefore the analysis of their stellar evolution is very interesting because only the initial mass of the stars is different. Open clusters have a shorter life, as a cluster, than their stars. This is due to tidal forces in the galactic gravitational field, evaporation and encounters with stars and interstellar clouds crossing their path around the galaxy. NGC 2420 is a very populated open cluster as it is constituted by more than three hundred stars, strongly concentrated in the centre and with a similar brightness. The H-R diagram of an open cluster depends on the age of the object. It shows only the main sequence (MS) if it is less than 500 Myr old. On the contrary, if the cluster is older, it shows other features, for example the turn-off point (TO), where stars "leave" the MS, which can be used to infer the age of the cluster by comparison with sets of isochrones of different metallicity and age.

2. Observational Data

NGC 2420 is an open cluster in the Gemini constellation, whose coordinate (J2000) are: RA = $07^h\ 38^m\ 24^h$, DEC = +21° 34′27″. It has an angular size of 10′.
We analysed 351 spectra of stars belonging to the open cluster, extracted from the Sloan Digital Sky Survey (SDSS) Data Release 7. These spectra were obtained with the 2.5 m f/5 telescope in Apache Point in the South-East of New Mexico (Latitude 32° 46′49.30″N, Longitude 105° 49′13.50″W, Elevation 2788m). Standard spectra were taken from the Jacoby library (Jacoby 1984).

3. Work description

In order to determine the spectral class of the 30 stars of our sample, we modified the spectra to make them comparable to those of the Jacoby library (Jacoby 1984).
We first corrected the spectra for reddening with the IRAF task DEREDDEN, using the value E(B-V) = 0.05 obtained by Jacobson et al. (2011).
Using the task SPLOT we found the average between 5450 and 5550 Å of the continuum of each of the 30 spectra and we observed that the relative error of this measure is always below 10%. This value was used to divide the spectrum, hence normalizing at 5500 Å, because the Jacoby spectra are normalized at this wavelenght.
The spectra were transformed in text files with the task WSPECTEXT to analyse them with the software TOPCAT. Using this software, we compared each spectrum of our sample with those of the library, gradually overlapping the spectra from the library to the observed ones, visually determining which of them best fitted (see Figure 1).
In the library spectra we noticed the presence of a deep absorption band, which was absent in the analyzed spectra (see Figure 2). We concluded that it was an absorption band due to the Earth's atmosphere that had

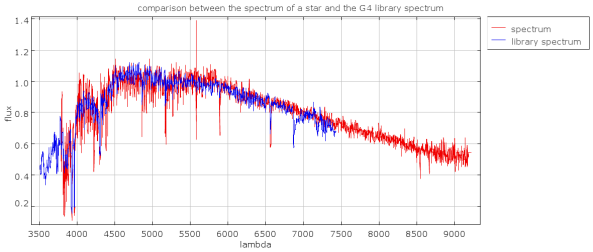

Fig. 1. Comparison between the spectrum of star 5 (red) and that of G4 star from the library (blue).

been corrected in the SDSS DR7 archive, but not in the library.

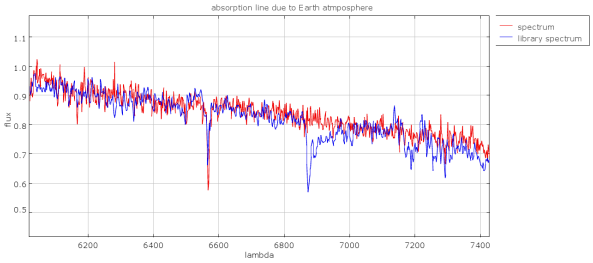

Fig. 2. Spectrum of the library (blue) overlapped to the one observed (red). It is evident the difference in the absorption band probably due to the Earth's atmosphere.

In order to verify our estimate of the spectral classes, we computed the difference between the flux of the observed star and the flux of the stars in the library. The difference ranged casually around 0 in correspondence to the spectral class that best fitted, as in Figure 3.

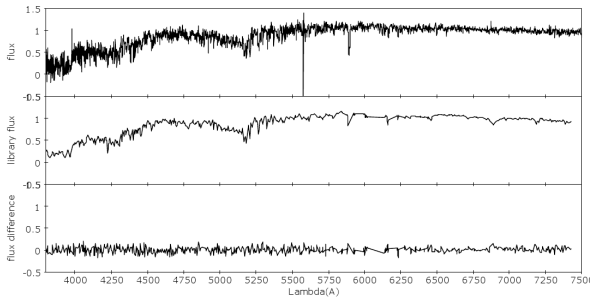

Fig. 3. Top: spectrum of the star to be classified. Center: spectrum of a K4 star from the library. Bottom: difference between the spectrum analyzed and the library spectrum. Since the residuals are around zero, the classification can be considered good.

To verify the results we compared the spectra of our stars to those of nearby spectral classes; in this way we noticed that the differences were increasing as it is shown is Figures 4 and 5. The results of our work are reported in Table 2.

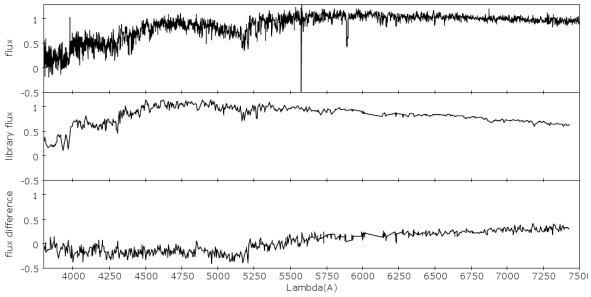

Fig. 4. Top: spectrum of the star to be classified. Center: spectrum of a G9 star from the library. Bottom: difference between the spectrum analyzed and the library spectrum. The residuals over 5500Å are above zero, therefore the classification cannot be considered good.

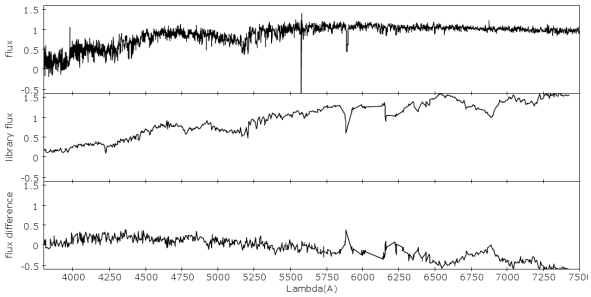

Fig. 5. Top: spectrum of the star to be classified. Center: spectrum of a M0 star from the library. Bottom: difference between the spectrum analyzed and the library spectrum. In this case the residuals are below zero and again the classification cannot be considered good.

Using the SSDD photometric data reported in Table 1, we calculated the color index (r - i) to determine the relation between these values and the spectral classes. We arbitrarily assigned a natural number from 1 to 32 to each of the spectral classes in the found range. For our sample, we plotted the value associated to the spectral class against the calculated color-index (Figure 6), finding a linear relation with correlation coefficient of 0.95. Therefore our sample proved the expected relation between color-index and spectral class for main sequence stars.

We used the same procedure to find the relation between the temperature and the spectral classes of the 30 sample stars. The values of temperature were taken from Affili, Casarin & Maguolo (2012). With these data we found a linear dependence between temperature and spectral class (see Figure 7) with a correlation coefficient r=0.98. The equation found is y = -0.0086 T + 64.81.

ID	RA (°)	DEC (°)	Spectral class
1	114.9735	21.4002	F4-F5
2	114.6514	21.4856	K2-K3
3	114.6541	21.5293	F8-G0
4	114.5458	21.4817	F0-F3
5	114.4921	21.5289	G4
6	114.5007	21.4523	F7-F8
7	114.3529	21.2430	K0
8	114.4639	21.5439	F0-F3
9	114.3934	21.2792	F8-G0
10	114.3612	21.5472	F7-F8
11	114.2716	21.4530	F3
12	114.5008	21.9307	F3
13	114.5514	21.8219	F0-F3
14	114.7915	21.6364	G4-G7
15	114.8338	21.3354	K4
16	114.8108	21.4273	K4
17	114.8214	21.5455	M0
18	114.7947	21.3329	K0-K4
19	114.7019	21.2075	K4-K5
20	114.6940	21.4959	K5-M0
21	114.5022	21.3501	K4
22	114.5346	21.4441	K0
23	114.3824	21.2302	K4-K5
24	114.3306	21.4731	K0-K4
25	114.2144	21.6947	K5-M0
26	114.3740	21.6822	K4
27	114.6812	21.9667	K4
28	114.6743	21.9474	M0-M1
29	114.7511	21.6117	K4
30	114.8330	21.9176	K0-K4

Table 1. Spectral class associated to each star and its coordinates.

ID	*g*	*r*	*i*
1	15.393	15.112	15.034
2	18.512	17.741	17.466
3	17.238	16.807	16.649
4	14.979	14.725	14.683
5	17.804	17.259	17.083
6	17.246	16.845	16.691
7	18.561	17.831	17.576
8	14.877	14.641	14.605
9	17.576	17.102	16.971
10	16.875	16.512	16.388
11	15.055	14.758	14.736
12	15.186	14.917	14.856
13	15.246	15.039	14.987
14	18.203	17.612	17.464
15	19.656	18.709	18.327
16	19.520	18.661	18.341
17	20.341	19.153	18.629
18	19.119	18.311	17.985
19	19.980	18.903	18.503
20	20.095	18.965	18.546
21	19.291	18.454	18.133
22	18.651	17.974	17.731
23	20.048	19.008	18.645
24	18.998	18.169	17.877
25	20.449	19.282	18.825
26	19.653	18.692	18.311
27	19.712	18.684	18.267
28	20.978	19.783	19.416
29	19.519	18.613	18.306
30	19.179	18.296	18.030

Table 2. Magnitudes in the photometric bands *g*, *r* and *i* for the 30 sample stars.

In order to calculate the temperature of the 351 stars in the cluster, we used the relation between color index (r-i) and temperature, given by Eq. 1:

$$T = \frac{k}{C_i - q} \quad (1)$$

We computed the color index (*r* - *i*) for all the 351 stars, and then we calculated the temperature through Eq. 1 with the values k = 3868 and q = -0.49 found by Affili, Casarin & Maguolo (2012). We noticed that the hottest stars have a temperature of about 7100 K and that the majority of the 351 stars is distributed between 4000 and 7000 K, as we can see in figure 8.

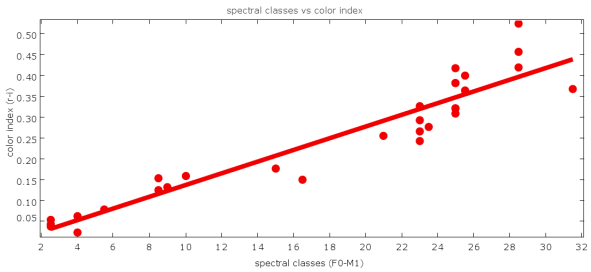

Fig. 6. Relation between spectral classes and color index (*r* - *i*). The equation of the regression line is (*r* - *i*) = 0.014x - 0.0043. It has a correlation coefficient of 0.95.

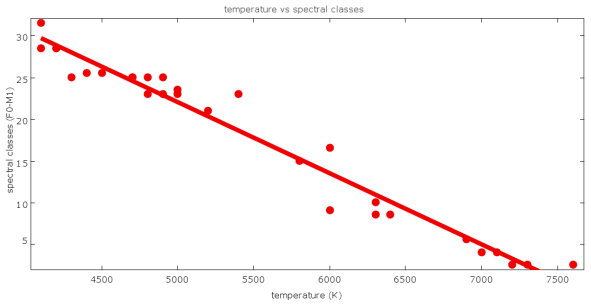

Fig. 7. Relation between temperature and spectral class. The linear relation between then two parameters is y = -0.0086 T + 64.81 and it has a correlation coefficient of 0.98.

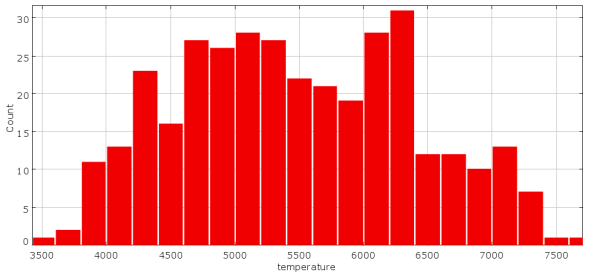

Fig. 8. Histogram of the temperature of the 351 stars. As it can be noticed most stars (95.7 % 100) have a temperature between 4000 K and 7000 K.

In order to build the H-R diagram we needed the relative brightness.

We initially converted the data from the *ugriz* photometric system to the *UBVRI* Johnson's system, obtaining the visual magnitude V from Eq. 2:

$$V = g - 0.569 \times (g - r) + 0.021 \quad (2)$$

We then calculated the absolute magnitudes with the formula:

$$M_v = V - 5\log(d) + 5 - A(V) \quad (3)$$

where V is the previously determined visual magnitude, d = 2.5 Kpc is obtained from Jacobson et al. (2011) and

A(V) = 3.1 × E(B − V) with E(B-V)=0.05. Through Pogson's equation:

$$M_v - M_v\odot = -2.5 \log \frac{L_v}{L_v\odot} \quad (4)$$

where $M_v\odot = 4.8$ is the value of the absolute magnitude of the Sun, we were able to obtain the relative brightness:

$$\log \frac{L_v}{L_v\odot} = -0.4(M_v - M_v\odot) \quad (5)$$

Then, we drew the H-R diagram of the cluster, placing on the x-axis the logarithm of the previously determined temperature and on the y-axis the logarithm of the relative brightness (see Figure 9). In the upper left corner of the diagram, some stars seem to diverge from the main sequence and this , considering that there are no stars with a temperature higher than 7100 K, made us think that these conditions indicate the turn-off point of the cluster.

Then, we estimated the age of the cluster. To do this, we

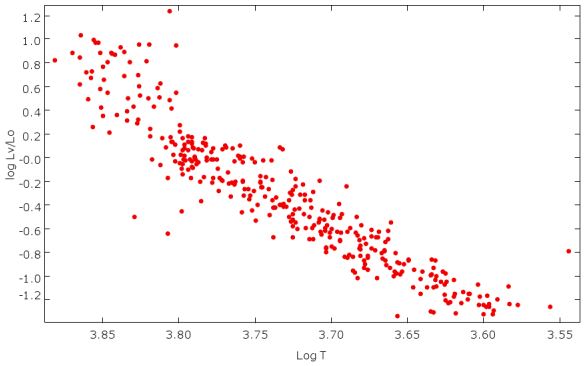

Fig. 9. H-R diagram of 351 stars of the cluster NGC 2420; on the x-axis the logarithm of the temperature on the y-axis the logarithm of the relative brightness.

found the position of the turn-off point overlapping to the H-R diagram a set of 13 isochrones with metallicity Z=0.008, value obtained by Anthony-Twarog et al. (1990) and by Saurabh Sharma et al. (2006), and with a logarithmic age between 9 and 9.65. The isochrones were taken from the Padova database of stellar evolutionary tracks and isochrones.

Through a graphical analysis we restricted the possible age of the turn-off point between the logarithmic ages of 9.25 and 9.45 (see Fig. 10). This made the age estimation of the cluster between 1.58 Gyr and 2.8 Gyr.

4. Results

We performed a spectral classification of a saample of 30 stellar spectra by graphically comparing them to library standard spectra. In order to value the reliability of our spectral evaluation, we computed the residuals between our sample and the standard stars, obtaining values around zero. We noticed that stars were included only between F0 and M1 classes, with no presence of hotter stars, indicating that the turn-off point was around 7000 K which would give an estimation of the cluster's age around a billion year. We verified the linearity of the relation between the (r - i) color index of the stars and their spectral class and between spectral class and temperature. We computed the temperature of 351 stars of the cluster, using the relation found by Affili, Casarin & Maguolo (2012) and noticing that the hottest stars have a temperature of about 7100 K. We then built the H-R diagram of the cluster, which shows the Main Sequence but few stars out of it, as well. These stars have moved to the next evolutionary step, after burning all the hydrogen in their nucleus. the comparison with a set of isochrones with Z=0.008 and the determination of the turn-off point confirmed that NGC2420 is a metal poor old open cluster: its age ranges between 1.58 and 2.80 Gyr, in agreement with the scientific literature.

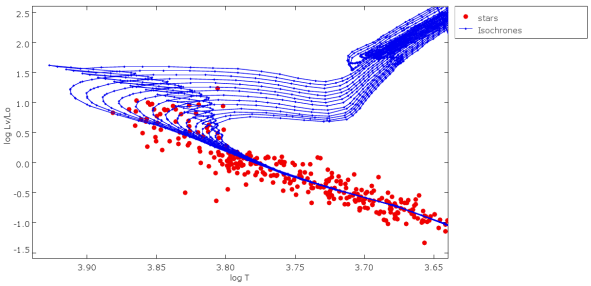

Fig. 10. H-R diagram with on the x-axis the logarithm of the temperature and on the y-axis the logarithm of the relative brightness overlapped by a set of isochrones.

References

Affili, E., Casarin, L. & Maguolo G., Temperature of the stars in the open cluster NGC 2420, The Sky As a Laboratory, 2012
Anthony-Twarog, B. et al. 1990, AJ, 1504, 99
Jacobson, H.R. et al. 2011, ApJ, 142, 59
Jacoby, 1984, ApJ, 56, 257
Padova database of stellar evolutionary tracks and isochrones, http://pleiadi.pd.astro.it/
Saurabh Sharma, et al. 2006, AJ, 1669, 132

Il Cielo come Laboratorio, 5
A.S. 2011-2012

Temperature of the stars in the open cluster NGC 2420

Elisa Affili[1], Lorenzo Casarin[2], Gianluca Maguolo[2]

[1]Liceo *G. Marconi*, sez. Scientifico, Conegliano
[2]Liceo *G. Berto*, sez. Scientifico, Mogliano Veneto

Abstract. The aim of our work was to determine the temperature and to estimate the radius and mass of 351 stars of the open cluster NGC 2420. We studied the spectra of 30 stars of the cluster to determine their temperature; then we obtained the relation between color index $(r - i)$ and temperature to calculate this variable for the other 321 stars. We also estimated the radius and mass from their relation with magnitude (Neece 1984), for all the 351 studied stars. In addition, we evaluated the statistical error of our results. Then we estimated the temperature of the turn-off point at about 7100 K and we studied the distribution of the mass and radius of the cluster's stars, which for the most part have a radius shorter than $2R_\odot$ and a mass smaller than $3M_\odot$. Our results are in accordance with the theoretical relations between the characteristic quantities of stars in a cluster's main sequence.

1. Introduction

The purpose of our analysis was to obtain data about the temperature, radius and mass of 351 stars located in the open cluster NGC 2420.

Open clusters are gravitationally related groups of stars originating from the same large cosmic gas and dust cloud; therefore they populate a limited region of space, typically much smaller than their distance from us, and they can be considered all roughly at the same distance so that the differences between apparent and absolute magnitude are the same. Moreover, the stars have similar age and chemical composition, but have different masses.

NGC 2420 is in the Gemini constellation; its position in the Galaxy is shown in Figure 1.

Since Planck curves depend only on temperature, we proceeded in a comparison between the curves and the spectra. So we determined the temperature of 30 stars and, with the given measures of apparent magnitude, we obtained a relation between color index and temperature. This relationship was useful to estimate the temperature of the other 321 stars.

Lastly, we used the theoretical relation between color index and radius and mass (Neece 1984) to calculate these quantities. From the study of the histogram we obtained statistical data about temperature, radius and mass of the cluster's stars.

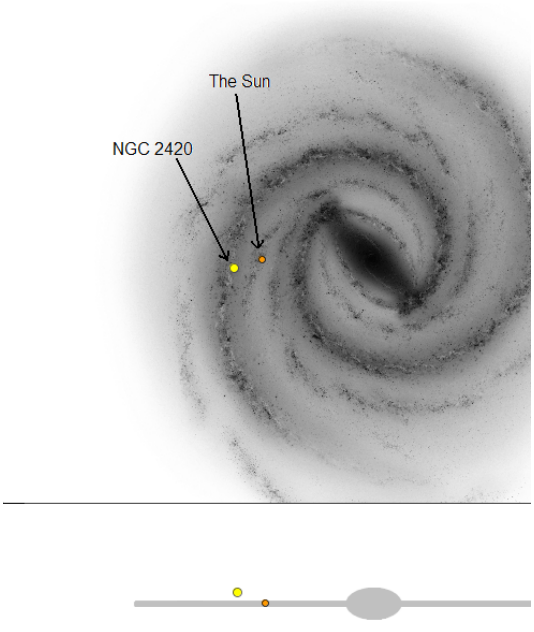

Fig. 1. Image generated by the software WHERE IS M13 showing the position of NGC 2420 in our Galaxy.

2. Observational Data

The spectra of the 30 stars and the data about magnitudes were downloaded from the archive Sloan Digital Sky Survey (SDSS) DR7. The SDSS uses a dedicated 2.5 m f/5 modified Ritchey-Chretien altitude-azimuth telescope located at Apache Point Observatory, in south eastern New Mexico (USA). The spectra are observed with a total integration time of 45-60 minutes depending on observing conditions.

Distance and color excess were taken from the article by Jacobson et al. (2011).
The cluster coordinate (J2000) are:
RA $7^h\ 38^m\ 24^s$
Dec $21°\ 34'\ 27''$
Figure 2 is an image of the cluster with the 30 stars, whose spectra we studied, shown in the circles. Their data are reported in Table 1.

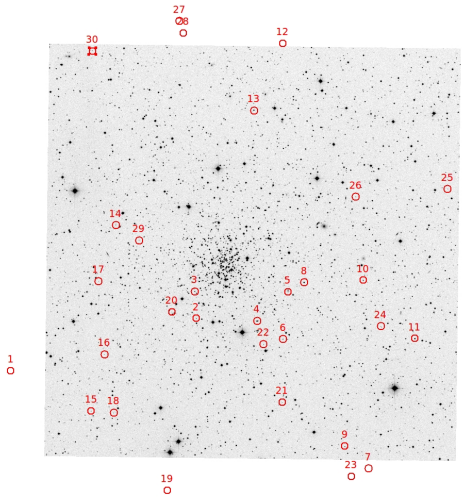

Fig. 2. Image of the cluster with the 30 stars highlighted by the circles.

ID	ra (°)	DEC (°)	g	r	i
1	114.9735	21.4002	15.393	15.112	15.034
2	114.6514	21.4856	18.512	17.741	17.466
3	114.6541	21.5293	17.238	16.807	16.649
4	114.5458	21.4817	14.979	14.725	14.683
5	114.4921	21.5289	17.804	17.259	17.083
6	114.5007	21.4523	17.246	16.845	16.691
7	114.3529	21.2430	18.561	17.831	17.576
8	114.4639	21.5439	14.877	14.641	14.605
9	114.3934	21.2792	17.576	17.102	16.971
10	114.3612	21.5472	16.875	16.512	16.388
11	114.2716	21.4530	15.055	14.758	14.736
12	114.5008	21.9307	15.186	14.917	14.856
13	114.5514	21.8219	15.246	15.039	14.987
14	114.7915	21.6364	18.203	17.612	17.464
15	114.8338	21.3354	19.656	18.709	18.327
16	114.8108	21.4273	19.520	18.661	18.341
17	114.8214	21.5455	20.341	19.153	18.629
18	114.7947	21.3329	19.119	18.311	17.985
19	114.7019	21.2075	19.980	18.903	18.503
20	114.6940	21.4959	20.095	18.965	18.546
21	114.5022	21.3501	19.291	18.454	18.133
22	114.5346	21.4441	18.651	17.974	17.731
23	114.3824	21.2302	20.048	19.008	18.645
24	114.3306	21.4731	18.998	18.169	17.877
25	114.2144	21.6947	20.449	19.282	18.825
26	114.3740	21.6822	19.653	18.692	18.311
27	114.6812	21.9667	19.712	18.684	18.267
28	114.6743	21.9474	20.978	19.783	19.416
29	114.7511	21.6117	19.519	18.613	18.306
30	114.8330	21.9176	19.179	18.296	18.030

Table 1. Data of the 30 stars whose spectra were analysed. The table reports position and *g*, *r*, and *i* magnitudes.

3. Work description

First of all, the spectra must be corrected because of the reddening due to interstellar dust. This was done with the task DEREDDEN of IRAF, using the value of color excess $E(B-V) = 0.05$ taken from the article by Jacobson et al. (2011).
With the task SARITH we normalized the spectra, dividing them by the value of intensity at 5500 Å; this value was obtained with the task SPLOT of IRAF by measuring the average value between 5450 and 5550 Å.
Then we compared the normalized spectra with normalized Planck curves of different temperatures, generated with the formula:

$$B(\lambda; T) = \left(\frac{5500}{\lambda}\right)^5 \frac{e^{\frac{1.439\cdot 10^8}{5500\cdot T}} - 1}{e^{\frac{1.439\cdot 10^8}{\lambda T}} - 1} \qquad (1)$$

Planck curves, differing even by 100 K, fitted the same spectrum: Figure 3 shows the plotting of a normalized spectrum and three normalized Planck curves at the temperature of 6800 (blue), 6900 (green) and 7000 (gray) K. Figure 4 is another example of estimate of temperature through the fitting method.

We estimated the absolute error of our work on the data; we normalized again the spectrum of a star that had, compared to the other stars, the greatest relative

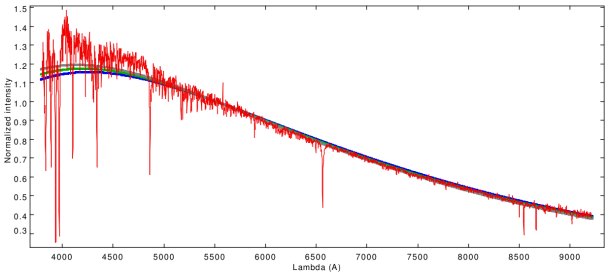

Fig. 3. Plot of a spectrum and three Planck curves at 6800 (blue), 6900 (green) and 7000 (gray) K. On x-axis wavelength in Å, on y-axis the normalized intensity.

error ($\sigma/I_{5500Å}$, where $I_{5500Å}$ is the average intensity between 5450 and 5550 Å) and we established again the temperature by fitting the spectrum against Planck curves.
The chosen star was star 25, which in a measure of intensity of 5.583×10^{-17} erg cm^{-2}s^{-1}Å^{-1} had a mean square deviation of 0.695 erg cm^{-2}s^{-1}Å^{-1}.
Then we normalized again the spectrum dividing it by $\sigma + I_{5500Å}$; the new value of temperature was only 100 K higher than the first one, so it confirmed the reliability

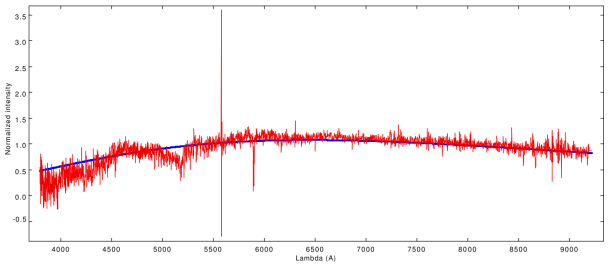

Fig. 4. Example of best fit with a black body curve at 4400 K. On x-axis wavelength in Å, on y-axis normalized intensity.

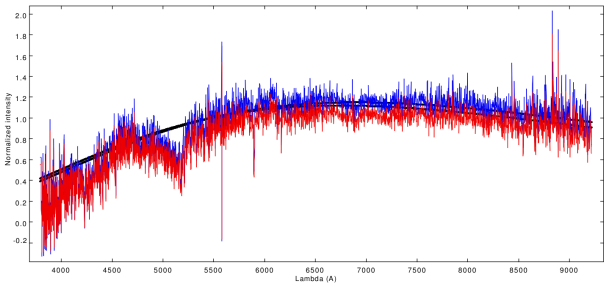

Fig. 5. Overlap of two Planck curves and two spectra normalized with different values of σ. On x-axis wavelength in Å, on y-axis normalized intensity. The difference in temperature is 100 K, a reasonable error.

of our work. The two spectra and two Planck curves are shown in Figure 5. We estimated a 3σ statistic error of about 300 K.

We checked the proportionality between color index

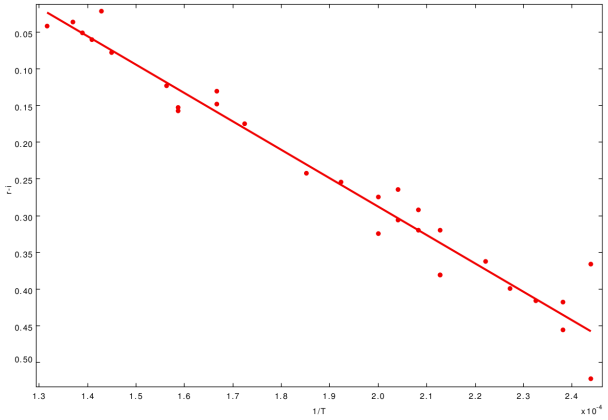

Fig. 6. r − i vs 1/T graph. The data are very well related.

$(r - i)$ and 1/T, the first one given as a data, the second one previously obtained. The graph, with the reciprocal of the temperature (1/T) on x-axis and color index $(r - i)$ on y-axis, is reported in Figure 6 and shows a very good linear correlation between the two quantities (the linear correlation coefficient is r = 0.97). The extrapolated formula is:

$$(\mathrm{r} - \mathrm{i}) = 3868\frac{1}{\mathrm{T}} - 0.485 \tag{2}$$

We wanted to use this relation to estimate the temperature of the other 321 stars of the cluster in consideration; solving the previous relation with respect to T, we obtain:

$$\mathrm{T} = \frac{3868}{(\mathrm{r} - \mathrm{i}) + 0.485} \tag{3}$$

Its results are shown on the histogram in Figure 7; the majority of the stars has a temperature lower than 7100 K.

Next we calculated the radius of the stars from their

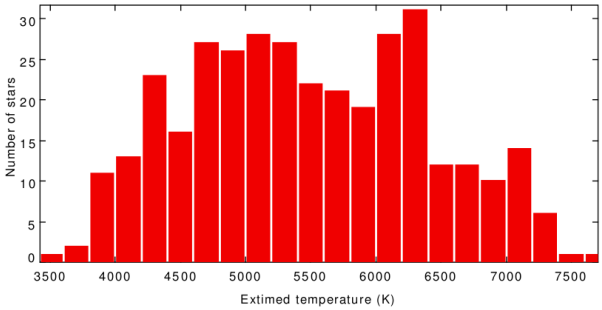

Fig. 7. Histogram of the temperature of 351 stars from the cluster. The majority of the stars has a temperature lower than 7100 K.

apparent magnitude, whose measures were supplied in *ugriz* filters, and from the distance between the cluster and us, d = 2.5 kpc (Jacobson et al. 2011).

Our formulae needed magnitudes in the *UBVRI* Johnson photometric system, but we had data only in the *ugriz* system, so we first calculated the values of B and V for each star with the formulae:

$$B = g + 0.349 \times (g - r) + 0.245 \tag{4}$$

$$V = g - 0.569 \times (g - r) + 0.021 \tag{5}$$

Then we obtained $B - V$, which we used to calculate the surface brightness $\mathrm{P_V}$ (Grey 2005):

$$\begin{aligned}\mathrm{P_V} = {} & 0.2241 - 0.5610(B - V) + 0.6207(B - V)^2 \\ & - 0.6056(B - V)^3 + 0.2041(B - V)^4\end{aligned} \tag{6}$$

We knew the relation between surface brightness and angular radius so we calculated the latter:

$$\theta_\mathrm{R} = \theta_\mathrm{R}^{\odot} \times 10^{-2[\mathrm{P_V} + 0.1(\mathrm{m_V} - \mathrm{m_V^{\odot}})]} \tag{7}$$

Now, given the distance, we calculated the radius:

$$\mathrm{R} = \left(\frac{\theta_\mathrm{R}}{206265}\right)\left(\frac{\mathrm{d}}{6.96 \cdot 10^5}\right) \tag{8}$$

In this way we had an estimate of the radius; from our calculation we know that 96% of the stars in the cluster

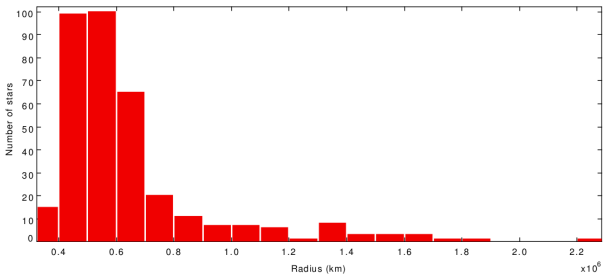

Fig. 8. Histogram of the radius measured in kilometers of 351 stars from the cluster. The majority of the stars has a radius shorter than $2R_\odot$.

have a radius which is less than $2R_\odot$, as we can see in Figure 8.

In the study of Neece (1984) we found the relation:

$$\frac{R}{R_\odot} = 0.87\left(\frac{M}{M_\odot}\right)^{0.8} \quad (9)$$

which can be resolved as:

$$\frac{M}{M_\odot} = \left(\frac{R}{0.87R_\odot}\right)^{1.25} \quad (10)$$

Analysing the results we saw that 97.4% of the stars in the cluster have a mass which is smaller than $3M_\odot$, as it can be seen in Figure 9.

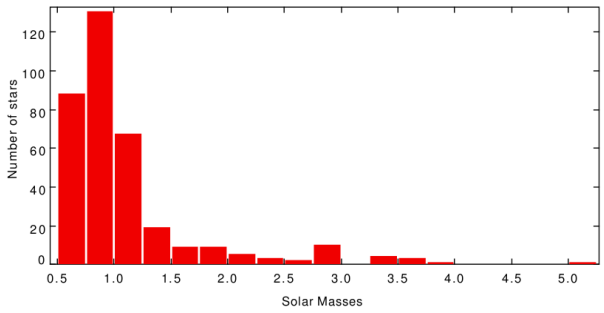

Fig. 9. Histogram of the mass measured in solar masses of 351 stars in the cluster. The majority of the stars has a mass smaller than $3M_\odot$.

4. Results

We studied a sample of 351 stars of the open cluster NGC 2420. We established independently the temperature of 30 of them by fitting their spectra with Planck curves and then we checked the relation between color index and temperature. This relation allowed us to widen our study to the other 321 stars; finally we calculated radius and mass for all the 351 stars.

Table 4 shows the results of our work for the 30 stars. From the results we obtained some statistical information:

ID	T (K)	$R/R_\odot$	$M/M_\odot$
1	6900	1.69	2.30
2	5000	0.86	0.98
3	6300	0.91	1.05
4	7600	1.97	2.77
5	5800	0.83	0.95
6	6300	0.86	0.99
7	5200	0.79	0.88
8	7300	2.01	2.84
9	6000	0.83	0.94
10	6400	0.97	1.14
11	7000	2.03	2.88
12	7100	1.83	2.53
13	7200	1.62	2.17
14	6000	0.74	0.82
15	4700	0.67	0.73
16	4700	0.62	0.66
17	4100	0.69	0.75
18	5000	0.69	0.75
19	4400	0.70	0.77
20	4200	0.72	0.79
21	4800	0.67	0.72
22	5400	0.69	0.75
23	4500	0.65	0.69
24	4800	0.75	0.84
25	4200	0.64	0.68
26	4700	0.69	0.75
27	4300	0.74	0.82
28	4100	0.52	0.52
29	4900	0.67	0.72
30	4900	0.76	0.84

Table 2. The results of our work on the data; the majority of the stars has a radius shorter than $2R_\odot$ and a mass smaller than $3M_\odot$. There are not many stars with a temperature higher than 7100 K.

- 95.7% of the stars have a temperature lower than or equal to 7100 K;
- 96.0% of the stars have a radius shorter than or equal to $2R_\odot$;
- 97.4% of the stars have a mass smaller than or equal to $3M_\odot$.

The data are consistent and confirm the relations between the typical quantities of stars in a cluster's main sequence. Since there is not a significant number of stars hotter than 7100 K, we concluded that the turn-off point in the HR diagram is positioned at this value of temperature.

References

Jacobson, H.R. et al. 2011, ApJ, 142, 59
Neece, G.D. 1984, ApJ, 738, 743
Grey, D.F., The Observation and Analysis of Stellar Photospheres, Cambridge University Press, 2005
http://www.sdss.org/dr7/

Il Cielo come Laboratorio, 9
A.S. 2011-2012

Photometric determination of the age and the distance of the open cluster NGC 2420

Francesco Bussola[1], Marco Faccioli[4], Giovanni Frezzato[3], Giulio Romanelli[2]

[1]Liceo Galilei, sez. Scientifico PNI, Verona
[2]Liceo Galilei, sez. Scientifico Tradizionale, Verona
[3]ISIS Calabrese-Levi, sez. Scientifico PNI, San Pietro in Cariano
[4] Liceo Medi, sez. Scientifico Tradizionale, Villafranca di Verona

Abstract. The *g, r, i* magnitudes of 738 stars of the open cluster NGC 2420 were measured by applying the aperture photometry technique to images taken from the SDSS archive.The *g, r, i* magnitudes were trasformed into *B, V, R* magnitudes used to build the Color-Magnitude Diagrams (CMDs). The aim of this work was the determination of the age and the distance of NGC 2420. By comparing the stellar distribution on CMD, *B-V* vs *V*, with the isochrones obtained from theoretical models, we were able to find these parameters. The isochrones depend on two main parameters, age and metallicity, so when the match between the stellar distribution and the isochrone is reached, we have both the parameters. Since the models are reddening free, it was possible to determine the color excess, E(*B-V*) and then the interstellar absorption A(*V*). The obtained results were compared with those found in literature, finding a substantial agreement, overall for the age and the metallicity. The age we obtained is 2 Gyr, the metallicity, Z, is between 0.004 and 0.008, the distance is about 2500 pc, and the color excess, E(*B-V*), is between 0.07 and 0.16. An estimate of the radii of the stars was performed by means of the surface brightness method. The stellar radius at the CMD turn-off is between 2 and 3 $R_{\odot}$, which is consistent with the age of the cluster.

1. Introduction

An open cluster is a group of stars born from a single cloud of interstellar gas and dust within the Galactic plane. It is composed by a small number of stars, about 700 in the case of NGC 2420, all relatively young. In fact they belong to population I. In an open cluster the stars are distribuited in a central denser region surrounded by a halo, without a well defined nucleus. Because cluster dimensions are much smaller – very few light-years in diameter – than its distance from Solar System, we can assume all stars are at the same distance from the observer. Age and distance are parameters that can be defined thanks to a Color-Magnitude Diagram (CMD). In order to build a CMD it is necessary to calculate the magnitude of the stars of the cluster at least in two spectral bands. Thus, we can get the color index, that is the difference between two magnitudes, which has to be plotted on a graph with one of the two measured magnitudes, for example: *B-V* vs. *V*. In general, in a CMD stars are distribuited in two main regions: the Main Sequence (MS) (population I) and Red Giants Branch (RGB) (population II). The point of passage from MS to RGB, called turn-off (Figure 1), moves gradually downward, where advanced spectral class stars are located. These stars have relatively low temperature and small mass, and take considerably more time to exhaust the hydrogen in their core. By identifing the turn-off point on the CMD, we can estimate the age and the distance of the cluster.

In order to determine the magnitude of a star in a specific spectral band we must measure the amount of light, in number of photons, recorded by the CCD and subsequently transform it into the calibrated magnitude, according to Pogson's equation (Eq. 1):

$$m = -2.5 \times \log_{10}(I) + k \quad (1)$$

where I is the light intensity, derived from the photons count, m the magnitude of the star and k a calibration constant. In this work, we built two CMDs of the cluster NGC 2420: *B-V* vs. *V* and *V-R* vs. *R* . By comparing our data with isochrones, theoretical models describing the position of coeval stars in the Hertzsprung-Russell diagram (HR), having different ages and metallicity, we were able to determine the age of the cluster, the color excess due to the absorption by interstellar dust, and the distance. Finally, we calculated the radii of the stars.

2. Observational Data

Observational data were extracted from the Sloan Digital Sky Survey archive (SDSS, www.sdss.org), one

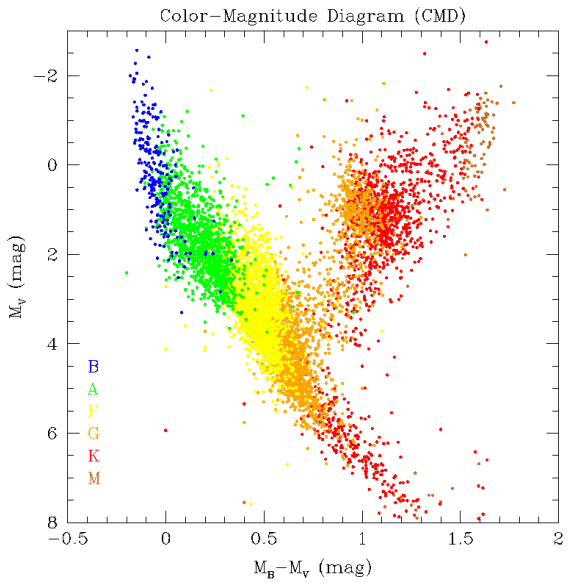

Fig. 1. Color-Magnitude Diagram based on the Hipparcos data, the spectral type of the stars is coded by different colors (from http://www.astrouw.edu.pl).

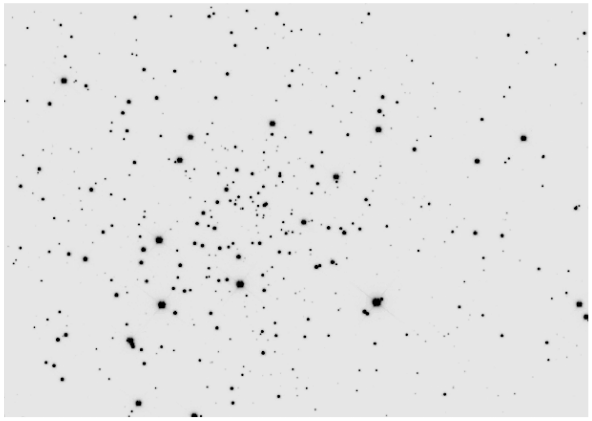

Fig. 2. SDSS image of NGC 2420 taken with the *r* filter.

of the most important ones in astronomy. The archive collects data from a 2.5-meters-wide telescope, located in Apache Point Observatory, New Mexico (USA). The field of view of the telescope is 1.5 square degrees, which corresponds to eight times the size of the full moon. In this research we used images taken in the *g, r, i* bands and the exposure time was 53.9 seconds for each image. An image of NGC 2420, taken with the *r* filter, is shown in Figure 2. The coordinates of NGC 2420 are $\alpha_{2000.0}$=07^h 35^m 05^s and $\delta_{2000.0}$=+21° 41′. The airmass value (X), the coefficient of atmospheric absorption (k) and the zero-point photometric constant (m_0), to convert the instrumental magnitudes, related to the intensity in photon counts unit, to the calibrated ones, related to the intensity in erg cm^{-2} s^{-1}, are taken from the SDSS archive and shown in Table 1.

Filter	X	k	m_0
g	1.07	0.14	24.447
r	1.06	0.09	24.071
i	1.06	0.03	23.741

Table 1. *g, r, i* calibration constants for NGC 2420.

3. Work description

In order to measure the *g*, *r* and *i* magnitudes of the same stars, at first it was necessary to align the three images. We considered the x-y positions of a sample of five stars as reference. The stars were common to every image and, after the calculation of their Cartesian coordinates, assuming the *r* image as reference, we calculated the average Δx and Δy values of the displacement vector of the other two images (Table 2). Then, we shifted the *g* and *i* images so that each stara had the same coordinates in each image.

Filter	Δx	Δy
g	-1.45	-11.29
r	0.00	0.00
i	1.04	-2.85

Table 2. X-Y shift values (in pixels) for the alignment of the three images.

In order to measure the magnitudes of the stars, we adopted the aperture photometry technique, whose principle is to calculate the intensity of a source within a circle of a given radius, called aperture radius, and subtract the contribution of the night sky, measuring its median intensity in a concentric circle having an inner radius a bit larger than the aperture radius, and multiplying this value by the number of the pixels within the circle containing the source. In addition, the exposure time must be taken into account, dividing the night sky subtracted intensity of the source by 53.9 s. For each image, we determined the Full Width at Half Maximum (FWHM) of the stars, the median brightness of sky and the relative dispersion (σ) of the sky-counts. In order to measure the FWHM, we chose a sample of 15 sources for each image. The source had to show a Gaussian shape of intensity distribution over the detector, that means a regular trend with a well-defined maximum (Figure 3); in case the source was saturated, that is the image is over-exposed, it would not be possible to define the FWHM because, having received a too high number of photons, the intensity distribution recorded by the pixels is not approximated to a Gaussian (Figure 4). We considered a median value for each of these parameters (Table 3).

The found values served as input for IRAF task DAOFIND. This task had to identify the sources with a FWHM compatible with the previously measured one and with a minimum emission of photons equal to that

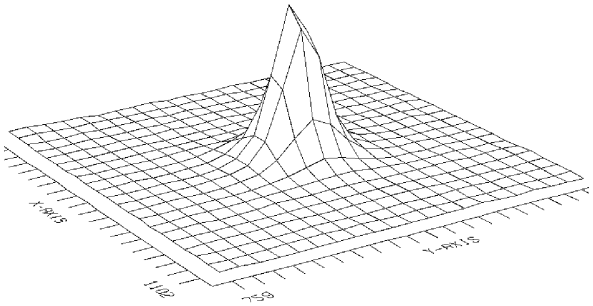

Fig. 3. Intensity distribution of a non-saturated source. The profile is approximated by a Gaussian function.

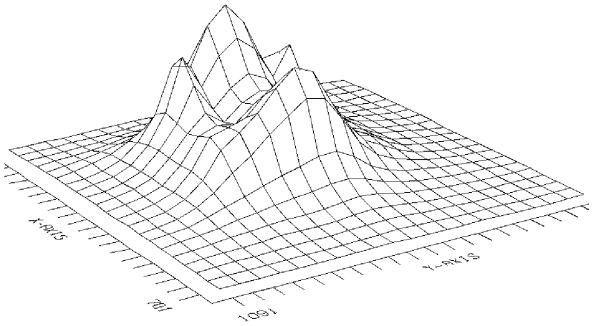

Fig. 4. Intensity distribution of a saturated source. The profile is absolutely irregular.

Filter	FWHM (pixels)	sky counts	σ
g	3.33	1091.2	2.76
r	2.67	1150.6	5.76
i	2.38	1300.0	5.58

Table 3. FWHM values, and sky intensity with its dispersion (σ) obtained from the average of 15 stars for each image.

of the sky, increased by the value of Threshold multiplied by σ (Eq. 2):

$$\mathrm{I_{min}} = \mathrm{I_{sky}} + (\mathrm{Threshold} \times \sigma) \quad (2)$$

(Ciroi, Cracco, Frassati 2011).
Then, we used the task TVMARK in order to verify the correctness of the identification of the sources. This task overlaps the found sources, identified by marks, to the image. We made some attempts changing the DAOFIND parameters up to reach a reliable identification of a great

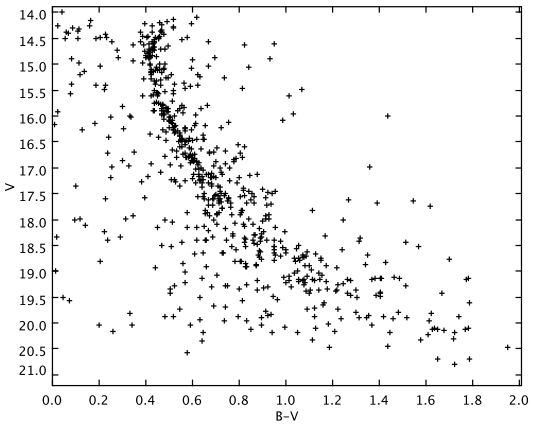

Fig. 5. Color-Magnitude Diagram, *B-V* vs *V*.

number of stars. With the task PHOT of IRAF we calculated the aperture photometry of the identified stars, obtaining as output a table for each image containing the coordinates of the sources and the respective instrumental magnitudes. The number of photometrized sources was 844, 974 and 1248 respectively for the g, r, i images. We matched the coordinates of the sources, using the software TOPCAT, with the constraint that the centroids of the stars must differ not more than 5 pixels, obtaining as a result 738 sources common to the three images. As a comparison, Leonard et al. (1988) were able to identify 685 stars.

From the instrumental magnitudes we calculated the calibrated g, r, i magnitudes using the parameters shown in Table 1 and the following formulas (Ciroi, Cracco, Frassati 2011):

$$g^{\mathrm{cal}} = g_0 - \mathrm{k}_g \times \mathrm{X}_g \quad (3)$$

$$r^{\mathrm{cal}} = r_0 - \mathrm{k}_r \times \mathrm{X}_r \quad (4)$$

$$i^{\mathrm{cal}} = i_0 - \mathrm{k}_i \times \mathrm{X}_i \quad (5)$$

Then we converted them into *B, V, R* magnitudes, which is the standard Johnson-Cousins photometric system.

$$B = g^{\mathrm{cal}} + 0.349 \times (g^{\mathrm{cal}} - r^{\mathrm{cal}}) + 0.245 \quad (6)$$

$$V = g^{\mathrm{cal}} - 0.569 \times (g^{\mathrm{cal}} - r^{\mathrm{cal}}) + 0.021 \quad (7)$$

$$R = r^{\mathrm{cal}} + 0.153 \times (r^{\mathrm{cal}} - i^{\mathrm{cal}}) - 0.117 \quad (8)$$

Eventually, we obtained the *B-V* vs. *V* and *V-R* vs. *R* CMDs by using TOPCAT (Figures 5 and 6). By using TOPCAT, we plotted on the two CMDs some theoretical models (Figures 7, 8 and 9), called isochrones, that describe the distribution of the stars with the same age. Consequently, these models allow us to understand the phases of the stellar evolution, in fact the positions of the stars on the CMD will vary over time. The

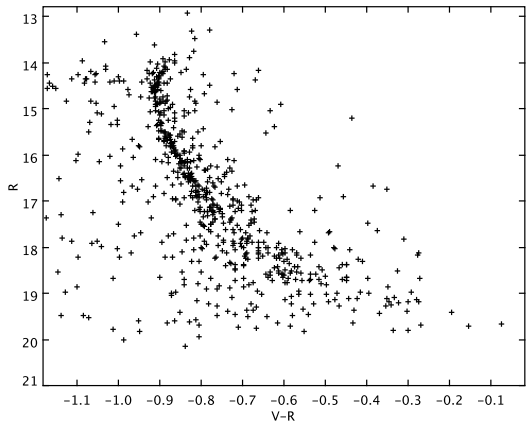

Fig. 6. Color-Magnitude Diagram, *V*-*R* vs *R*.

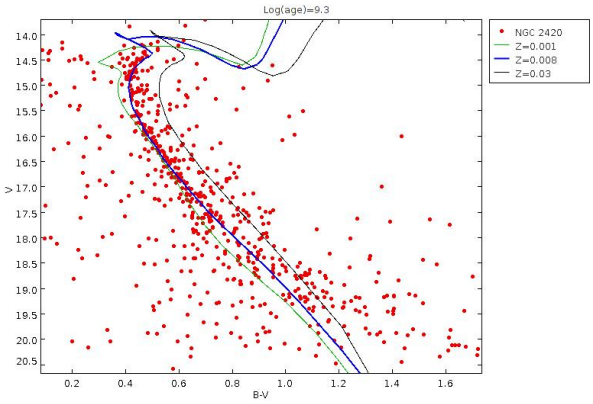

Fig. 7. Isochrones with different metallicities and the same age (log(*t*) = 9.3) on the *B*-*V* vs *V* diagram.

isochrones we used (Girardi et al. 2004) are given in absolute magnitudes and reddening-free colors, so the curves must be shifted along the x and y-axis to fit the observational data. The displacement along the y-axis gives us the Distance Modulus (DM= $V-M_V$), whereas the displacement along the x-axis gives the color excess E(*B*-*V*), which is related to the interstellar absorption A(*V*)=3.1× E(*B*-*V*).

Once estimated the DM value, we obtained the distance with the following formula:

$$d = 10^{\frac{DM+5-A(V)}{5}} \quad (pc) \qquad (9)$$

Each isochron is characterized by a certain metallicity and age. Some attempts were made using the *B*-*V* vs *V* CMD. NGC 2420 can be described using various isochrones with different age and metallicity. However, it was possible to exclude some isochrones because they gave negative or null interstellar absorption, or an inconsistent DM. Anyway, being clearly visible the turn-off point, we estimated an age of 2 Gyr, with a DM about 12.3 and E(*B*-*V*) between 0.07 and 0.16 (Table 4). The precise value of the metallicity is difficult to be calculated only with photometric data. However, a value of Z between 0.004 and 0.008 can be considered plausible.

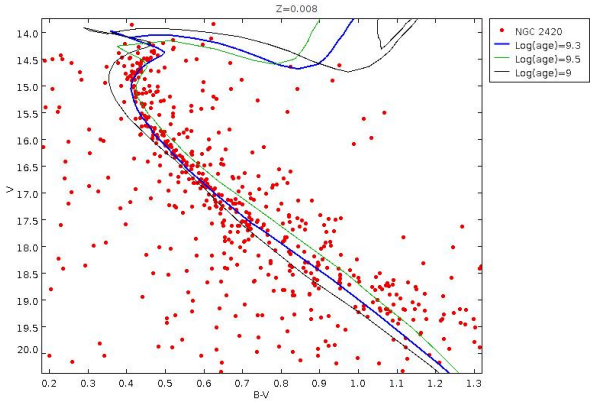

Fig. 8. Isochrones with different ages and the same metallicity (Z=0.008) on the *B*-*V* vs *V* diagram.

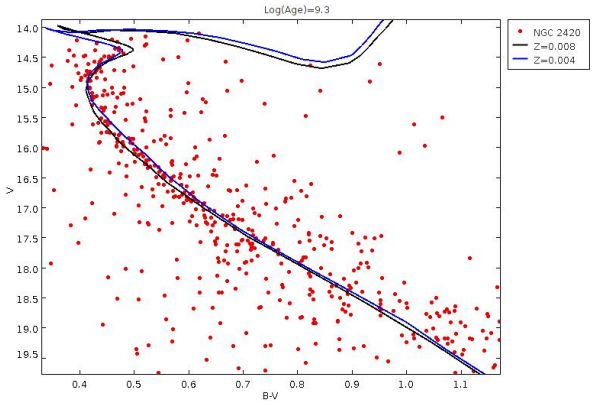

Fig. 9. Fitting of the two best isochrones on the CMD, log(*t*) = 9.3, Z=0.004 (black curve) and Z=0.008 (blue curve).

Z	Log(t)	E(*B*-*V*)	DM	A(*V*)
0.030	9.3	0.00	12.1	0
0.001	9.3	0.25	12.7	0.775
0.004	**9.3**	**0.155**	**12.35**	**0.4805**
0.008	**9.3**	**0.07**	**12.28**	**0.217**
0.008	9.5	0.00	11.6	0
0.008	9.0	0.20	13.2	0.62

Table 4. Parameters obtained by fitting the observed CMD with the isochrones. In bold the best fits are indicated.

In order to provide an estimate of the radii of the stars, we derived the angular radii as a function of the surface brightness (P_V), defined as magnitude per

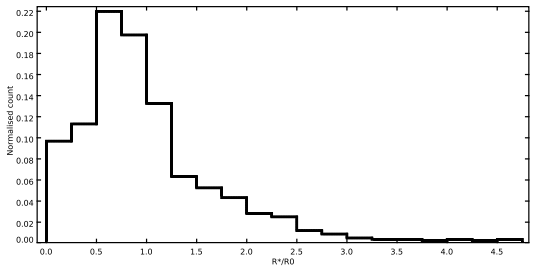

Fig. 10. Distribution of the radii of the stars ($R_\star/R_\odot$), obtained with the surface brightness method.

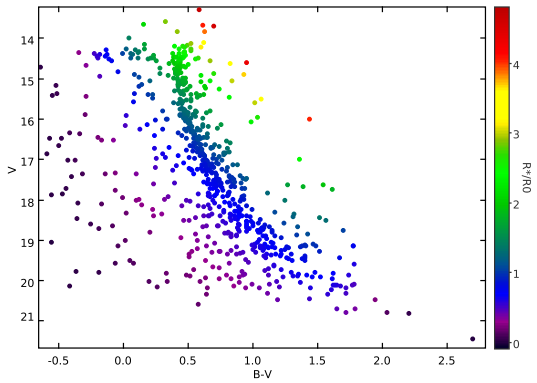

Fig. 11. CMD with the radii of the stars in colored scale. The radius of the stars at the turn-off is between 2 and 3 $R_\odot$.

squared arcsec, by adopting the formula (Eq. 10) given by Grey (2005):

$$\frac{\Theta_R}{\Theta_R^\odot} = 10^{-2\times[P_V+0.1\times(m_V-m_V^\odot)]} \quad (10)$$

Once determined the angular radius of the star, we could derive the linear radius by using the formula (Eq. 11):

$$\frac{R_\star}{R_\odot} = \frac{\Theta_R}{206265} \times \frac{d}{6.96\times10^5} \quad (11)$$

where d=2475.5 pc ($\cong$ 7.64×10^{16} km) is the average of the distances obtained by the best fits (Figure 9). The radii distribution (Figure 10) shows a mode value slightly less than solar radius ($0.75\ R_\odot \lesssim R_{mode} \lesssim R_\odot$). The radius of the stars at the turn-off is between 2 and 3 solar radii (Figure 11).

4. Results

We carried out a photometric analysis of the open cluster NGC 2420 starting from three images obtained with the *g*, *r* and *i* filters, extracted from the SDSS archive. The purpose was the determination of the age and the distance of the cluster by means of the CMDs. These diagrams were compared to theoretical isochrones to provide an estimate of the age, distance and metallicity of the cluster. Our CMDs show clearly that NGC 2420 is composed mainly of MS stars and has an evident turn-off. The age of NGC 2420 turned out to be about 2 Gyr, and the distance about 2.5 kpc. The determination of its metallicity results very difficult through photometric analysis alone. Nevertheless, the best fit models (Figure 9) gave a reasonable value of Z between 0.004 and 0.008.

References	E(*B-V*)	DM	Age (Gyr)	Z
this work	**0.16**	**12.35**	**2**	**0.004**
this work	**0.07**	**12.28**	**2**	**0.008**
1	0.05	11.95	2.4	0.006
2	0.08	12.05	2	0.005
3	0.05	12.15	1.9	0.005

Table 5. Comparison of the obtained results between this work (in bold) and the most recent data. References: (1) Demarque et al. (1994) - (2) Prada Moroni et al (2001) - (3) Anthony-Twarog et al. (2006).

Comparing our results with the most recent data collected from the literature, it appears that age and metallicity are consistent with the values found by Demarque et al. (1994), Prada Moroni et al (2001) and Anthony-Twarog et al. (2006) (Table 5). We point out that Anthony-Twarog et al. (2006) strongly suggest that the metallicity of NGC 2420 is half of the solar one (Z=0.01). With this value of metallicity all the cited authors obtained a distance slightly lower than ours. Concerning the color excess, we find a reasonable agreement with the literature using Z=0.008. Finally, we evaluated the stellar radii by means the surface brightness method: the stellar radii at the turn-off point are between 2 and 3 $R_\odot$. These values are consistent with the age of the cluster.

References

Anthony-Twarog, B. J., Delora, T., Cracraft, M.,& Twarog, B.A. 2006, AJ,131,461-472
Ciroi, S., Cracco, V., Frassati, A., 2011, Fotometria, 'the Sky as a Laboratory', handouts, 101
Demarque, P., Sarajedini, A., & Guo ,X.-J., 1994, AJ,426,165-169
Girardi, L., Greber, E.K., Odenkirchen, M., & Chiosi, C. 2004, apj, 700, 1816
Grey, D. F., 2005, The Observation and Analysis of Stellar Photospheres, Cambridge University Press
Leonard, P. J. T., 1988, AJ,95,1
Prada Moroni, P. G., Castellani, V., Degl'Innocenti, S., Marconi, M., 2001, Mem. S.Alt.,72,4

Il Cielo come Laboratorio, 15
A.S. 2011-2012

Photometric Analysis of the Globular Cluster NGC5272

Stefano Camporese[1], Giacomo Giudice[1], Chiara Konishi De Toffoli[2], Federica Niola[3], Tobia Zorzetto[3]

[1] Liceo Scientifico Ippolito Nievo, Padova
[2] Liceo Scientifico Enrico Fermi, Padova
[3] Liceo Scientifico Tito Lucrezio Caro, Cittadella

Abstract. We studied the globular cluster NGC5272. The purpose of our work was to determine its age, metallicity, and distance. We used aperture and PSF photometry on the filters *g*, *r* and *i*. Thus, we analyzed the obtained data through the *B*, *V* and *R* Johnson-Cousins photometric bands. Then, we plotted the color-magnitude diagram (CMD) of the cluster and compared it to different isochrone models. We found the best fit which gave us values of age (12.5 Gyr), metallicity (0.0004) and, through the determination of the distance modulus and the color excess, we obtained the distance (6.9 kpc).

1. Introduction

Stellar clusters are groups of stars that are gravitationally bound together and are born around the same time from a single molecular cloud. Therefore, the stars in a cluster have approximately the same age and chemical composition. Stellar clusters can be open or globular. The open clusters, due to their smaller population of stars (between 100 and 1000 stars), are less massive and so their shape is more irregular because the stars are less tightly bound together gravitationally. They can be found in the gas-rich galactic disc, and thus are primarily made of young stars. These clusters have a high metallicity value and their brightest stars are the blue giants of the main sequence. The Pleiades are a simple example observable by the naked eye. Globular clusters are instead composed of a greater number of stars (between 10^4 and 10^6), so that their heavier mass leads to a stronger gravitational binding. They have a spherical shape and a high stellar density, especially in the center. These objects are found in the galactic halo, where interstellar gas is absent, and are formed by population II stars, born in the first phases of the formation of their galaxy. Therefore, the globular clusters have a low metallicity and their brightest stars are red giants.

The analysis of the HR diagram, in particular the position of the turn-off point (where the red giant branch splits off from the main sequence) is useful to determine the age of a cluster: in the diagram corresponding to younger clusters it is located earlier in the main sequence. The advantage of studying a single cluster is that all the stars have the same distance and metallicity, while they differ only in mass, which determines their evolutionary path.

We undertook the photometric study of the globular cluster NGC5272, also known as M3, which was first discovered by Charles Messier in 1764 and is shown in Figure 1. It has an apparent magnitude of 6.2, so it can be seen by naked eye only under certain conditions. Located in the constellation of Canes Venatici, it has coordinates of right ascension RA=$13^h\ 42^m\ 11.62^s$ (J2000) and declination DEC= $28^o\ 2'\ 38.2''$ (J2000) with an apparent diameter of 18 arcminutes. It contains more than 5×10^5 stars and is a class VI globular cluster, meaning it has a somewhat average value of stellar density.

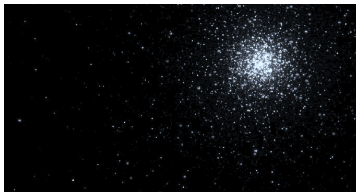

Fig. 1. The globular cluster NGC 5272.

In order to study the globular cluster NGC5272 we used both aperture and PSF photometry to obtain the coordinates and magnitudes of the stars in the different filters. We then matched these data to construct a color-magnitude diagram (CMD) and compared it with different isochrone models to deduce general characteristic of the cluster.

2. Observational Data

We used images taken from the Sloan Digital Sky Survey (SDSS web site 2008) with the 120-megapixel Charge Coupled Device (CCD) of the 2.5 m telescope of Apache Point (New Mexico, USA). The exposure time was 54 s. The photometric study was performed using the filters *g*, *r* and *i* whose wavelengths are shown in Table 1.

Filter	Wavelength
g	4686 Å
r	6165 Å
i	7481 Å

Table 1. Wavelengths of the filters *g*, *r* and *i*.

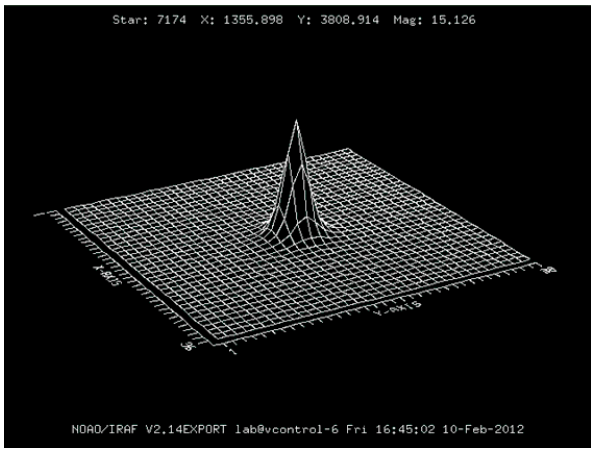

Fig. 2. Example of a regular, three-dimensional profile of a star.

3. Work description

We carried out the photometric analysis of the globular cluster combining the aperture photometry and the Point Spread Function (PSF) fitting. Using these techniques on *g*, *r* and *i* images we obtained the data to construct a color-magnitude diagram. We used the Image Reduction and Analysis Facility (IRAF) program, in particular the DAOPHOT and IMAGES packages and their DAOFIND, PHOT, PSF, ALLSTAR and IMEXAMINE tasks.

The images were not aligned because of chromatic aberration, that alters the focal point of the telescope depending on the filter used. To compensate for this problem, we took the *r* band image as a reference, we calculated the average shift in pixels of a sample of stars, and we used it to change the frame of reference on the *g* and *i* images, to align them with the fixed one.

The aperture photometry consists of calculating the flux of each star by adding up the pixel counts within an aperture centered on each object and subtracting off the average sky count, determined by a circular ring around the object, multiplied by the number of pixels within the aperture. In a globular cluster this technique is not suitable because of the high stellar density. As a matter of fact, it is not straightforward to determine either the aperture or the circular ring in which to calculate the flux of a single object and the background flux of the sky, especially in the center of the cluster. Despite this, the aperture photometry is necessary to apply the PSF technique. To proceed with the photometric analysis, some parameters about the images to analyze need to be established. By working on each filter and using the task IMEXAMINE, we obtained these parameters: from the analysis of a sample of 15 stars we found the Full Width at Half Maximum (FWHM) of the stellar intensity profile. Then we examined the flux of the sky areas without any stars, obtaining the average flux and the average standard deviation σ of the background. We also noted the exposition time of the images and the airmass.

Having obtained these parameters, we identified the light sources in the images. To do this we used the tasks DAOFIND and PHOT in the package DAOPHOT. The task DAOFIND analyzes the image and searches for intensity peaks that have a FWHM equal to the input value and a maximum of counts greater than:

$$I_{star} \geq I_{sky} + (\text{threshold} \times \sigma) \tag{1}$$

where I_{sky} is the average value of the sky counts per pixel, σ is the obtained standard deviation, and threshold is a value that we adjusted manually to filter out spurious sources. We could see the light sources thus identified superimposed on the image of the cluster to check if the mapping was consistent with the image, and hence we could eventually modify the threshold value to obtain a better result. The task PHOT calculates the aperture instrumental magnitude of the sources found with DAOFIND. This task uses this equation:

$$mag^i = 25 - 2.5 \log\left(\frac{I_* - n_{pix} \langle I_{sky} \rangle}{t_{exp}}\right) \tag{2}$$

where mag^i is the instrumental magnitude, I_* is the sum of photon counts detected in a circular area in which there are n_{pix} pixels. Because of the influence of the background on this value, we had to consider the $\langle I_{sky} \rangle$ that is the average value of the counts per pixel, determined in the ring centered on the star, and we need to multiply it by n_{pix}, to take into account the sky contribution. Finally, t_{exp} is the exposure time.

Because of the high density of stars in globular clusters, it is difficult to determine the correct aperture to calculate the flux of a single star. Therefore we applied the PSF photometry, which consists in estimating the magnitude of the sources by means of a mathematical model, called the PSF model. The PSF model describes the average distribution of the stellar light detected on the CCD. This distribution is the result of the diffraction and the atmospheric turbulence (seeing), that randomly

deflects the direction of the stellar rays and causes the broadening of the observed object.

We used the task PSF, of the DAOPHOT package, that allows one to create a PSF model from our sample of 20 stars. The stars we chose belonged to the ones found by the aperture photometry. They also had to be isolated, different in brightness, uniformly distributed in the cluster, and they had to have a regular three-dimensional profile, such as the one shown in Figure 2. We calculated the PSF magnitude by fitting each of the star profiles with a PSF model. To fit the PSF model, we used the task ALLSTAR that determines the coordinates (x, y) of the star centers and the magnitudes of the stars found by the aperture photometry. We obtained the exact position of the stars and their flux, with contamination from the background and nearby sources having been subtracted. Not every star of the cluster was recognized at the first attempt, so the software was recursively run several times.

In this way we found the magnitudes of the recognized stars. As explained above, these magnitudes indicate the photon flux measured by the telescope, not the calibrated flux. The calibrated flux is then calculated from the magnitudes using the equation:

$$m_{cal} = m_0 + m - a - kx \tag{3}$$

where

- m_{cal}: calibrated magnitude
- m_0: calibration constant depending on the filter used
- m: instrumental magnitude
- k: coefficient of atmospheric extinction
- x: airmass
- a = 25: constant chosen previously to make all magnitudes positive

Parameters	g	r	i
m_0	24.416	23.987	23.664
k	0.212	0.125	0.080
x	1.196	1.183	1.186

Table 2. Values of the calibration constants of our SDSS images.

After the magnitude calibration, we matched the pixel coordinates of the stars in each filter. The original aperture photometry yielded around 45000 stars in the r band, 18000 in the g band and 9000 in the i band. By matching the coordinates of the stars in g and r, we identified around 17000 stars. To analyze data related to a color-magnitude diagram V-R vs. R, we had to match the three filters, but the three-way intersection produced only 1000 stars, too few to obtain a meaningful graph. So we created a color-magnitude diagram B-V vs. V. We converted the magnitudes in g and r into B and V filters, belonging to the Johnson's photometric system, using the transformation equations elaborated by K. Jordi et al. (2006):

$$B = g + 0.345 \times (g - r) + 0.245 \tag{4}$$

$$V = g - 0.569 \times (g - r) + 0.021 \tag{5}$$

We plotted the graph by inserting B-V in the x-axis and V in y-axis, obtaining the color-magnitude diagram shown in Figure 3.

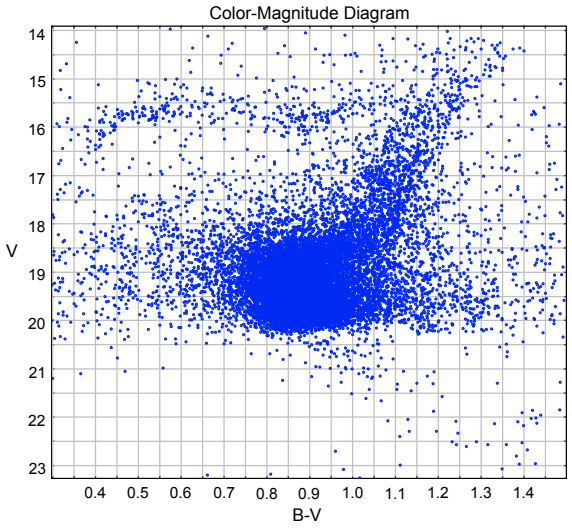

Fig. 3. Color-magnitude diagram.

We compared this CMD to the isochrones created by L. Girardi (2006). The isochrones are theoretical curves that represent the distribution of the stars belonging to the same star population on the H-R diagram and their evolutive traces with certain values of age and metallicity. Since the isochrones are expressed in absolute magnitude, the shift along the y-axis represents the distance modulus $V - M_V$ of the cluster, while that along the x-axis represents the excess of color or reddening $E(B - V)$, related to the visual absorption $A(V)$, which gives an estimate of the effect of weakening of the radiation due to the presence of gas and dust. This varies according to the direction of the object and its height on the Galactic plane. In fact, the color excess $E(B - V)$ is linked to the visual absorption $A(V)$ by the equation:

$$A(V) = 3.1 \times E(B - V) \tag{6}$$

From the distance module $V - M_V$ we get the distance, considering the absorption in V band. We used the equation:

$$V - M_V = 5\log(d) - 5 + A(V) \tag{7}$$

from which we derived the distance of the cluster:

$$d = 10 \exp\left[\frac{V - M_V + 5 - A(V)}{5}\right] \tag{8}$$

which gives approximately: d ≈ 6.9 kpc. We obtained the best fit using the isochrone with a metallicity of Z=0.0004 and an age of 12.5 Gyr. The fit is shown in Figure 4.

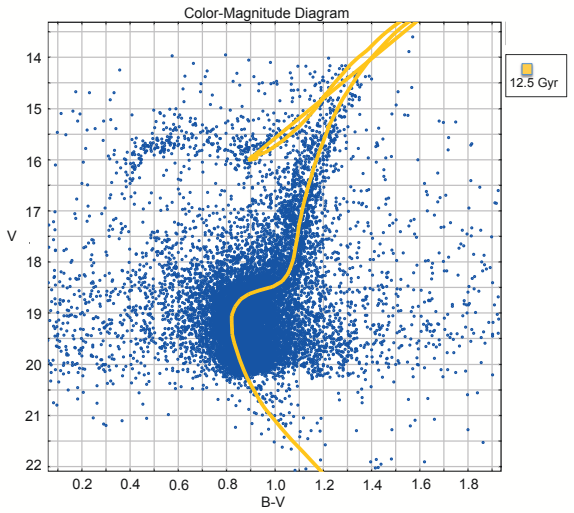

Fig. 4. CMD of NGC5272 and isochrone.

4. Results

Our photometry using the aperture and PSF techniques yielded the following results:

- Age: 1.25×10^{10} years
- Metallicity: 0.0004
- Stars analysed: approximately 17000
- Distance: 6.9 kpc

The values of the age and the metallicity are quite similar to the ones found in literature. We referred to the study of Woolf, N. J. (1967), that reported a value for the age of 8×10^9 years. Instead, the distance we found is quite different from the value of 10 kpc reported by the studies of C. Liu et al. (2008).

References

SDSS web site, http://www.sdss.org

Jordi, K., Grebel, E. K., Ammon, K., et al. 2006, Empirical color transformations between SDSS photometry and other photometric systems, A&A, 460, 339

Girardi, L. 2006, Isochrone Models web site, http://pleiadi.pd.astro.it/isoc_photsys.02/isoc_photsys.02.html

Woolf, N. J., 1967, Age of Messier 3, AJ, 67, 286

Liu, C., Hu, J., Newberg, H., Zhao, Y., 2008, Candidate Milky Way satellites in the Galactic halo, A&A, 477, 139

Il Cielo come Laboratorio, 19
A.S. 2011-2012

Spectroscopic analysis of the planetary nebula NGC 7009

Sabrina Cuogo, Giada Faraon, Francesco Pegoraro, Giada Volpato, Alessandro Zecchin

Liceo E. Majorana - E. Corner, sez. Scientifico, Mirano

Abstract. In this work, carried out at the Asiago Observatory last February, we aimed to analyse the spectrum of the planetary nebula NGC 7009, in order to determine several physical and chemical properties of matter, depending on its distance from the central star, through the analysis of spectral lines. First we singled out seventeen monodimensional spectra from the initial bidimensional spectrum. Then we identified the chemical elements, represented by the spectral lines. After that, we corrected the fluxes because of the extinction. Finally, we derived the temperature, density and abundance of the different chemical elements. The results of our work show that the temperature of this astronomical object is between 9000 K and 11000 K, and that its electron density ranges between 3700 and 3800 cm^{-3} near the star, and between 1300 and 1900 cm^{-3} in the external side.

1. Introduction

A planetary nebula is a a very large cloud of gas surrounding a white dwarf star. Planetary nebulae evolve from stars as massive as the Sun, up to 4 times its mass. It burns hydrogen in its core for the greater part of its lifetime, staying in the Main Sequence. When the hydrogen in the core is completely exhausted, the star starts to burn hydrogen in a shell outside the core, determining the expansion of the outer layers, and it moves to the Red Giant Branch. Inside the core, the gravitational pressure raises and so does the temperature, reaching the point that allows the star to burn helium into carbon and oxygen. That causes the further expansion of the outer layers, and the star reaches the Horizontal Branch. Once the helium burning is ended, the fusion of hydrogen and helium goes on inside two shells, while the core remains inactive, and the star moves to the Asymptotic Branch. The collapsing core does not let the fusion of carbon and oxygen begin, but makes the outer layers expand. These are so far from the star that its gravitational attraction does not affect them any more, and lets them go away. What remains is a core, made up of carbon and oxygen, called white dwarf: it has a very high temperature and density, and it is surrounded by the relics of the previous layers of the original star, which are still expanding, and creating the Strömgren sphere: this determines the radius within which the gas is completely ionized. The radiation released from the star ionizes and heats the surrounding gas: the electrons, according to Bohr's theory, get excited through specific wavelengths and the quantized energy necessary for the electron to change orbital, from the upper ones to the lower ones, is then released as electromagnetic radiation, with a defined wavelength. In our case we analysed the spectrum in the visible range, finding out Balmer's spectral lines over the stellar continuum, because of the position of the spectrograph's slit, which was centered on the white dwarf. In this case the nebula taken into consideration is NGC 7009, also known as Saturn Nebula (Figure 1), because of its elongated shape, that makes it look like the famous planet.

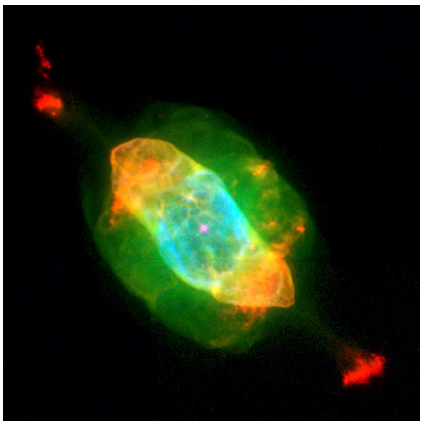

Fig. 1. Image of NGC 7009, obtained with Hubble Space Telescope on December 17^{th}, 1997.

2. Observational Data

The studied spectrum was obtained on August 30^{th}, 2001 with the Isaac Newton telescope (diameter 2.5 m) in La Palma Island (Spain), which has the following

instrumental characteristics: IDS spectrograph, grating 300 lines/mm, 1.5″slit, CCD 1024 × 1024 pixel, $\Delta\lambda$ = 3600–7000 Å exposure time 90 sec, spatial scale 0.7″/px.
NGC 7009 is located in Aquarius constellation; it was discovered on September 7th, 1782 by William Herschel, and has the following equatorial coordinates at epoch J2000.0: RA = 21^{h} 04^{m} 10.877^{s}, DEC = -11° 21′48.25″. It is at an estimated distance of 774 pc from the Sun, it has an apparent size of 41″× 35″and an apparent magnitude of +12.8.

3. Work Description

The work started with the analysis of the bidimensional spectrum (Figure 2): in order to measure the change of the spectrum as a function of the distance from the central star, this was divided, by using the program DS9 and the function BLKAVG of IRAF, in 17 equal sections 5 pixels wide, as shown in Figure 3, that correspond to a width of 3.5″along the slit of the spectrograph. The instrument was set so as to include the central star and, because of the elongated shape of the nebula, also its most external regions, for its whole length. In this way

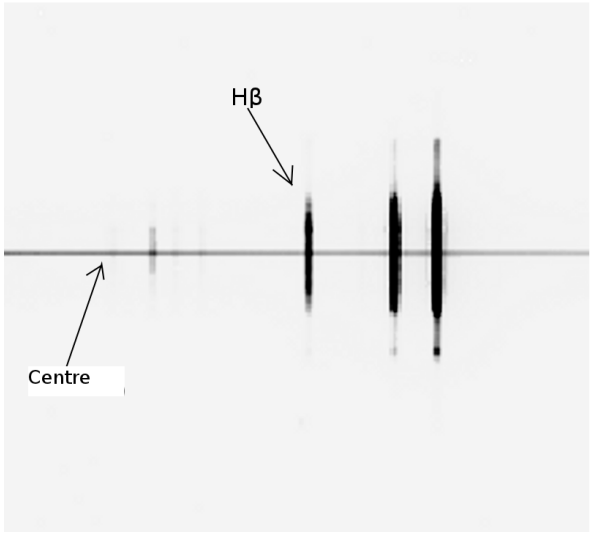

Fig. 2. Particular of the bidimensional spectrum of the nebula, with the central star spectrum and the Hβ line highlighted.

it was obtained a monodimensional spectrum for each section (Figure 4). Then using the program SPLOT of the ONEDSPEC package of IRAF, the spectral lines in emission were analysed, identifying for each one the wavelength of the respective chemical element and measuring the flux, which was obtained by calculating the area under the Gaussian function that better fitted each emission peak (Figure 5). In addition, the standard deviation of the continuum was measured, in order to give an estimate of the error associated to each flux (sse Table 1).

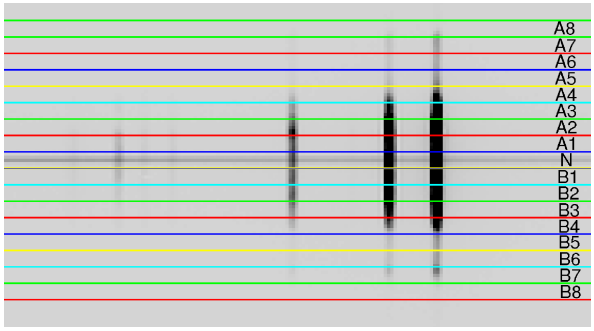

Fig. 3. Division of the bidimensional spectrum into 17 monodimensional sections.

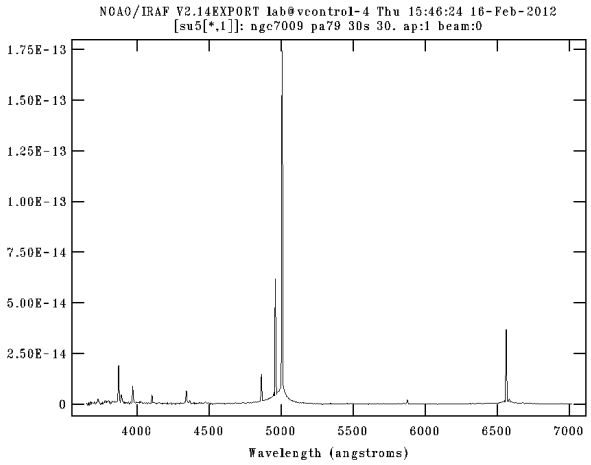

Fig. 4. Example of a monodimensional spectrum of one od the extracted regions.

The data were reported into a text file with GEDIT editor and organized in a table to be readable by the program TOPCAT. Using TOPCAT, the relative errors of the measured fluxes were calculated by creating a column in the table with the ratio between the standard deviation of the continuum and the amplitudes of the Gaussians (ΔF / F).
Moreover, the absolute error was found multiplying the flux of the line by the relative error, which then gave the values of deviation of the intrinsic flux. The observed fluxes, measured with the area under the Gaussian as in Figure 5 were then corrected for extinction, because of the presence of dust in the interstellar space attenuates the flux intensity, being interposed between the observer and the source.
Using the Cardelli, Clayton, & Mathis (1989, CCM) formula the values of A_V were found:

$$\left(\frac{F_{H\alpha}}{F_{H\beta}}\right)_{int} = \left(\frac{F_{H\alpha}}{F_{H\beta}}\right)_{oss} \times 10^{(-0.1386\times A_V)} \quad (1)$$

The intrinsic ratio has the known value of 2.86, so because we knew the observed ratio, we were able to calculate A_V, or the absorption in the visible range, still using TOPCAT. With this value, we were also able to

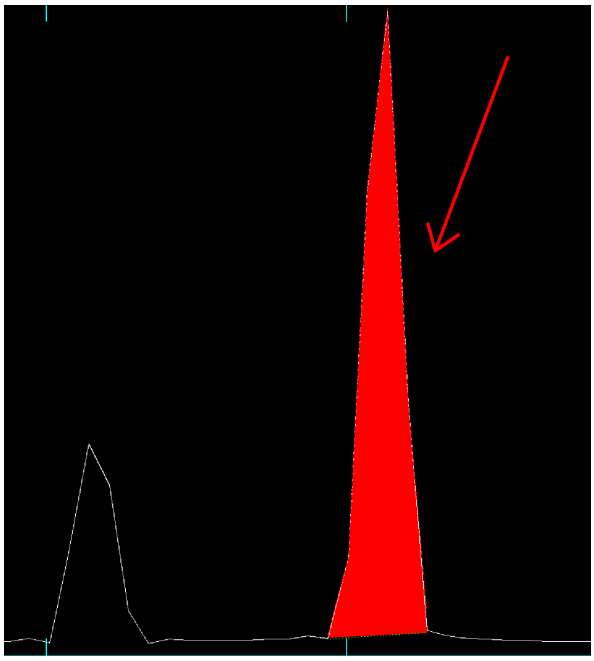

Fig. 5. Flux of the [O III] 5007 line of the central spectrum (N region), obtained by fitting a Gaussian function to the profile of the line.

calculate, for each spectral line, the intrinsic flux F(λ), with the formula:

$$F(\lambda)_{int} = F(\lambda)_{oss} \times 10^{0.4A(\lambda)} \quad (2)$$

The coefficients A(λ), that is the absorption values for different wavelengths, were calculated with the formula:

$$A(\lambda) = A(V) \times \left[a(y) + \frac{b(y)}{3.1} \right] \quad (3)$$

where a(y) and b(y) had known values for each spectral line. At this point we were able to determine the physical parameters of the different regions, using the ratio I_{6716}/I_{6731} of [S II] for density (e^-/cm^3) and ($I_{5007} + I_{4959}$)/I_{4363} of [O III] for the temperature. So using the task TEMDEN of IRAF, these parameters were calculated in an iterative way, in other words: assuming an hypotetical value of the temperature, in this case 10000 K, and inserting it into the program, it calculated the corresponding density, by inserting the obtained value, a different value of the temperature that was closer to the real one was obtained. This process was repeated until the two values became stable. In the A3 region the temperature is 9860 K, the density is 3850 e^-/cm^3, in B3 they are respectively 9050 K and 3710 e^-/cm^3. In A7 the temperature is 10270 K and the density is 1300 e^-/cm^3, while in B7 they are 10270 K and 1910 e^-/cm^3. At this point, in order to obtain density-distance (Figure 6) and temperature-distance (Figure 7) graphs, because the distance in pixels of each region from the centre of the nebula were already known, the distances in arcseconds were found with the following mathematical relationship:

$$r('') = r(px) \times scale('/px) \quad (4)$$

where scale ($''$/px) is the spatial scale along the slit,in this case 0.7$''$/px . Finally, knowing the distance in parsec of the nebula from the Earth, d = 774 pc, the distance of each region from the center of the nebula was calculated, with the following formula:

$$r(pc) = \frac{r('') \times d(pc)}{206265''} \quad (5)$$

where 206265 is the number of arcseconds in a radiant, approximating the tangent of the angle to the angle itself, because of the enormous distance that separates us from that object. One last calculation was the chemical abundancies of oxygen and nitrogen, as compared to hydrogen: after the ratios [O II]3727/Hβ, [O III]4959+5007/Hβ and [O III]4959+5007/([O II]3727+[O I]6300) were calculated, the abundance of oxygen could be found with the formula:

$$\frac{O}{H} = \frac{[O\ I] + [O\ II] + [O\ III]}{H\ I} \quad (6)$$

The value found in A3 region is 4.88×10^{-4} cm^{-3}, while in B3 region is 6.59×10^{-4} cm^{-3}.
After calculating the O/N = [O II]3727/[N II]6548+6584 ratio, the nitrogen abundance was found with:

$$\frac{N}{H} = \frac{O}{H} \times \frac{N}{O} \quad (7)$$

The results were: 2.69×10^{-4} cm^{-3} in A3 region, while 3.35×10^{-4} cm^{-3} in B3 region.

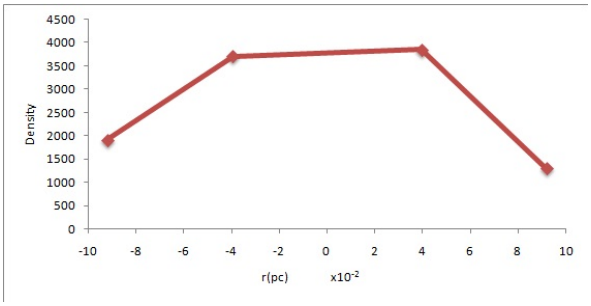

Fig. 6. Density graph, in which the variation of the electron density (e^-/cm^3) is plotted against the radius (pc).

4. Results

The object of our research was NGC 7009, a planetary nebula in the constellation Aquarius, 774 pc far from the Earth. We analyzed the distribution of the various chemical elements inside the nebula, the temperature and density of the various regions in which it was

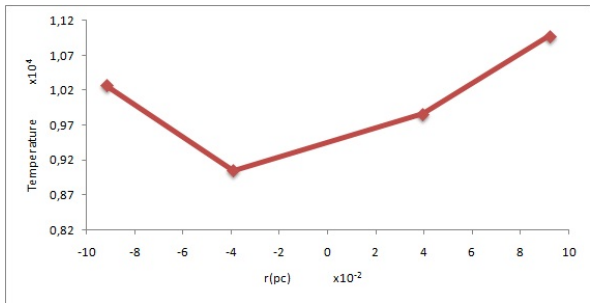

Fig. 7. Temperature graph, in which it is shown how the temperature is higher in the external parts of the nebula.

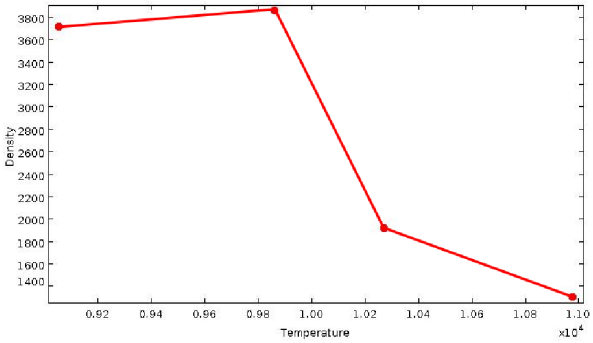

Fig. 8. Temperature-density graph.

divided. Several sections of the nebula were independently considered, the spectral lines of their monodimensional spectra were studied, so that the chemical elements found in the region could be classified. The observed fluxes were corrected for extinction, and temperature, density and distance from the centre of the nebula were calculated for each region. Finally, the chemical abundancies of oxygen and nitrogen were calculated as compared to hydrogen.

In the whole nebula the presence of spectral lines in emission of once ionized oxygen ([O II]), twice ionized neon ([Ne III]) and neutral hydrogen (H I) was found; in the central part the presence of H10, H9, once ionized helium (He II) and three times ionized argon ([Ar IV]) was detected, while in the first shell neutral helium (He I) and once ionized sulfur ([S II]) were present. Traces of once ionized iron (Fe II), neutral oxygen ([O I]) and once ionized nitrogen ([N II]) were also found. Temperature is lower in the centre, with values between 9000 and 10000 K, and higher in the external shells, with values between 10000 and 11000 K. The electron density is higher in the centre, with values between 3700 and 3800 cm^{-3} and lower in the outer parts, 1300-1900 e^-/cm^3. The abundancies of oxygen and nitrogen were calculated in the first shell: O/H is between 4.9 and 6.5×10^{-4} cm^{-3} and N/H is between 2.7 and 3.4×10^{-4} e^-/cm^3. These values are similar to the ones already found in other researches, reported in the references. In fact, in Bohigas, Lòpez, & Aguilar (1994) a temperature of the nebula of 9000 ± 400 K, but an electron density of 2300 ± 400 e^-/cm^3 was mentioned. So it is important to notice (see Figure 8) that in the inner regions, corresponding to the first shell, there is a lower temperature, altough matter is nearer to the central star, but a higher density, differently from the external regions, in which the high temperature and the low density indicate a very high kinetic energy of the particles that compose the external parts of the nebula.

References

Bohigas, J., Lòpez, J.A., Aguilar, L. 1994, ARA&A, 595, 603
Cardelli J. A., Clayton G. C., Mathis J. S., 1989, ApJ, 345, 245
Krabbe, A.C., Copetti, M.V.F. 2006, ARA&A, 31, 473
Lame, N.J., Pogge R.W. 1996, ApJ, 2320, 2331
Phillips, J.P., Cuesta, L.C., Ramos-Larios, G. MNRAS, 881, 902
Wikipedia.it, *Nebulosa Saturno*
Wikipedia.org, *Saturn Nebula*

Table 1. Tables with the obtained values of flux and error for each line. Fluxes are $\times 10^{-14}$ erg cm^{-2} s^{-1}, temperatures in K, densities in e$^-$/cm^3, abundancies $\times 10^{-4}$.

Region	[OII]3727	err [OII]3727	OIII 3755	err OIII 3755	H10 3798	err H10 3798	H9 3836	err H9 3836
N	24.80	5.81	-	-	-	-	26.50	6.30
A1	40.50	9.40	-	-	0.22	5.01	25.90	6.04
A2	71.80	18.90	-	-	0.20	5.35	32.60	8.35
A3	127.00	37.70	-	-	9.74	2.94	11.20	3.42
A4	16.60	5.79	2.85	5.79	3.88	1.44	2.90	1.10
A5	3.77	1.46	-	-	-	-	-	-
A6	3.21	0.99	-	-	-	-	-	-
A7	18.10	6.54	-	-	1.17	0.47	-	-
A8	14.00	5.33	-	-	-	-	-	-
B1	37.10	2.53	-	-	-	-	21.80	0.07
B2	43.80	1.73	-	-	0.17	0.02	20.60	0.53
B3	86.60	1.73	-	-	9.21	0.06	15.10	0.29
B4	21.10	0.01	-	-	3.50	0.03	4.54	0.11
B5	-	-	-	-	-	-	-	-
B6	5.91	0.24	-	-	-	-	-	-
B7	32.30	0.24	-	-	-	-	-	-
B8	0.75	0.10	-	-	-	-	-	-

Region	[NeIII]3869	err [NeIII]3869	HeI 3889	err HeI 3889	[NeIII]3968	err [NeIII]3968	HeI 4026	err HeI 4026
N	416.00	94.80	61.40	15.30	155.00	37.80	-	-
A1	409.00	94.30	73.50	17.80	184.00	43.10	-	-
A2	453.00	114.00	81.70	21.80	208.00	53.10	-	-
A3	199.00	58.50	37.60	11.60	89.00	26.80	4.04	1.17
A4	51.80	19.00	11.10	4.10	23.30	8.67	-	-
A5	12.90	4.29	3.87	1.32	6.25	2.08	-	-
A6	13.50	2.99	2.84	0.77	5.77	1.42	-	-
A7	11.40	4.40	1.54	0.61	4.60	1.64	-	-
A8	5.97	2.05	1.66	0.62	2.03	0.83	-	-
B1	347.00	0.45	71.30	0.37	153.00	0.23	-	-
B2	297.00	0.43	62.60	0.43	138.00	0.08	-	-
B3	237.00	0.36	48.40	0.59	103.00	0.03	-	-
B4	67.90	0.22	15.00	0.07	32.00	0.08	2.63	0.22
B5	13.20	0.74	-	-	6.61	0.01	-	-
B6	10.30	0.02	1.19	0.00	4.22	2.56	-	-
B7	14.90	0.02	2.52	0.47	7.03	0.36	-	-
B8	1.22	0.37	-	-	-	-	-	-

Region	[SII]4069	err [SII]4069	[SII]4076	err [SII]4076	Hδ 4102	err Hδ 4102	Hγ 4340	err Hγ 4340
N	-	-	-	-	87.70	21.50	162.00	40.40
A1	-	-	-	-	106.00	25.50	184.00	45.50
A2	-	-	-	-	118.00	29.90	204.00	53.00
A3	9.63	3.05	-	-	44.60	13.50	822.00	255.00
A4	-	-	-	-	12.10	4.22	21.10	7.67
A5	-	-	-	-	3.04	1.14	5.11	1.60
A6	-	-	-	-	2.77	0.76	5.16	1.13
A7	0.61	0.17	0.48	0.19	2.48	0.95	4.58	1.55
A8	-	-	-	-	0.55	0.19	1.61	0.60
B1	-	-	-	-	88.10	0.06	148.00	0.31
B2	-	-	-	-	78.80	0.07	139.00	0.29
B3	8.44	0.62	-	-	58.30	0.24	99.50	0.09
B4	3.00	0.17	-	-	17.50	0.01	32.00	0.04
B5	-	-	-	-	3.06	0.03	5.55	0.15
B6	-	-	-	-	3.05	0.17	4.90	0.04
B7	2.07	0.07	-	-	2.49	0.02	5.33	0.18
B8	-	-	-	-	-	-	0.54	0.10

Region	[OIII]4363	err [OIII]4363	HeI 4472	err HeI 4472	FeII 4638	err FeII 4638	HeII 4686	err HeII 4686
N	45.30	11.90	16.00	1.95	17.50	4.61	106.00	27.30
A1	30.30	7.64	20.10	5.07	15.50	4.03	95.80	24.60
A2	31.20	8.47	25.30	6.87	-	-	39.20	11.00
A3	12.70	4.10	9.86	3.06	-	-	14.00	43.50
A4	3.16	1.22	2.47	0.98	-	-	3.04	11.70
A5	0.93	0.35	1.05	0.42	-	-	-	-
A6	1.41	0.34	-	-	-	-	-	-
A7	0.85	0.26	-	-	-	-	-	-
A8	-	-	-	-	-	-	-	-
B1	25.60	0.32	15.00	0.30	-	-	71.50	0.02
B2	19.80	0.20	13.60	0.10	-	-	31.40	0.07
B3	14.50	0.01	11.70	0.18	-	-	16.20	0.17
B4	5.00	0.14	4.27	0.14	-	-	6.62	0.36
B5	-	-	-	-	-	-	-	-
B6	-	-	-	-	-	-	-	-
B7	0.81	0.02	-	-	-	-	-	-
B8	-	-	-	-	-	-	-	-

Region	[ArIV]4711	err [ArIV]4711	[ArIV]4740	err [ArIV]4740	Hβ 4861	err Hβ 4861	[OIII]4959	err [OIII]4959
N	22.00	5.69	19.70	5.24	350.00	91.30	1410.00	378.00
A1	611.00	137.00	23.00	5.68	387.00	100.00	1520.00	406.00
A2	15.00	4.16	13.30	3.70	433.00	120.00	1800.00	518.00
A3	4.59	1.50	3.26	1.04	172.00	54.20	721.00	234.00
A4	-	-	-	-	44.60	16.60	188.00	71.50
A5	-	-	-	-	10.30	3.88	45.60	17.30
A6	-	-	-	-	7.13	2.06	37.50	10.80
A7	-	-	-	-	7.35	2.69	34.40	13.00
A8	-	-	-	-	3.23	1.19	11.90	4.46
B1	11.80	0.28	14.70	0.10	306.00	0.19	1240.00	13.20
B2	9.24	0.19	8.06	0.34	280.00	0.19	1170.00	13.10
B3	5.80	0.27	4.32	0.06	195.00	0.29	861.00	7.74
B4	-	-	-	-	66.10	0.18	281.00	2.70
B5	-	-	-	-	11.60	0.02	50.20	0.73
B6	-	-	-	-	9.44	0.09	39.50	0.32
B7	-	-	-	-	10.10	0.02	40.00	0.22
B8	-	-	-	-	1.17	0.49	18.30	1340.00

Region	[OIII]5007	err [OIII]5007	FeII 5190	err FeII 5190	[NII]5755	err [NII]5755	HeI 5876	err HeI 5876
N	4010.00	1050.00	-	-	-	-	50.50	14.20
A1	4350.00	1140.00	-	-	-	-	59.10	16.30
A2	5140.00	1440.00	-	-	-	-	71.50	21.10
A3	2070.00	655.00	-	-	-	-	27.40	9.03
A4	537.00	199.00	-	-	-	-	7.08	2.63
A5	131.00	45.50	-	-	-	-	1.63	0.59
A6	110.00	30.80	-	-	-	-	1.36	0.40
A7	100.00	37.00	-	-	0.27	0.09	1.12	0.39
A8	34.70	12.80	-	-	-	-	0.75	0.28
B1	3500.00	6.35	-	-	-	-	43.10	0.28
B2	3260.00	1.88	-	-	-	-	43.60	0.20
B3	2440.00	1.61	-	-	-	-	30.00	0.07
B4	796.00	0.58	-	-	-	-	10.20	0.07
B5	144.00	0.24	-	-	-	-	2.18	0.06
B6	115.00	0.17	-	-	-	-	1.78	0.03
B7	117.00	0.29	-	-	-	-	1.88	0.09
B8	10.30	0.15	0.16	0.01	-	-	-	-

Region	[OI]6300	err [OI]6300	[SIII]6310	err [SIII]6310	[OI]6364	err [OI]6364	[NII]6548	err [NII]6548
N	-	-	-	-	-	-	-	-
A1	-	-	-	-	-	-	-	-
A2	-	-	-	-	-	-	23.30	7.21
A3	11.30	29500.00	4.14	2.96	3.99	1.30	51.10	17.90
A4	-	-	-	-	-	-	4.02	1.54
A5	-	-	-	-	-	-	-	-
A6	-	-	-	-	-	-	-	-
A7	0.42	0.13	0.30	0.13	-	-	2.39	0.90
A8	1.12	0.63	-	-	-	-	4.88	3.99
B1	-	-	-	-	-	-	-	-
B2	-	-	-	-	-	-	-	-
B3	-	-	-	-	-	-	41.50	0.03
B4	-	-	1.83	0.05	-	-	7.35	0.08
B5	-	-	-	-	-	-	-	-
B6	-	-	-	-	-	-	1.24	0.02
B7	2.02	0.02	-	-	1.11	0.01	11.40	0.03
B8	-	-	-	-	-	-	0.24	0.04

Region	Hα 6563	err Hα 6563	[NII]6584	err [NII]6584	HeI 6678	err HeI 6678	[SII]6717	err [SII]6717
N	1000.00	290.00	-	-	-	-	-	-
A1	1110.00	309.00	20.10	5.98	-	-	-	-
A2	1240.00	365.00	63.20	20.40	-	-	-	-
A3	491.00	164.00	183.00	60.70	-	-	14.40	4.96
A4	124.00	46.00	11.50	4.17	-	-	-	-
A5	27.90	10.40	1.05	0.42	-	-	-	-
A6	20.40	6.18	1.48	0.47	-	-	-	-
A7	18.60	7.06	8.96	3.42	0.59	0.22	1.07	0.41
A8	8.73	3.99	15.20	4.00	-	-	1.62	0.61
B1	875.00	2.56	-	-	14.10	0.12	-	-
B2	801.00	8.81	47.10	0.16	-	-	-	-
B3	558.00	0.79	117.00	0.48	7.12	0.25	8.38	0.09
B4	189.00	0.36	21.90	0.06	-	-	-	-
B5	33.20	0.03	-	-	-	-	-	-
B6	27.00	0.04	4.04	0.13	-	-	-	-
B7	28.80	0.65	34.80	0.07	-	-	3.42	0.06
B8	2.00	0.04	0.89	0.16	-	-	-	-

Region	[SII]6731	err [SII]6731	Te	Ne	O/H	N/H
N	-	-	-	-	-	-
A1	-	-	-	-	-	-
A2	-	-	-	-	-	-
A3	23.50	7.70	9861.70	3849.42	4.88	2.69
A4	-	-	-	-	-	-
A5	-	-	-	-	-	-
A6	-	-	-	-	-	-
A7	1.30	0.48	10976.80	1299.37	-	-
A8	1.82	0.60	-	-	-	-
B1	-	-	-	-	-	-
B2	-	-	-	-	-	-
B3	13.60	0.29	9051.70	3707.66	6.59	3.35
B4	-	-	-	-	-	-
B5	-	-	-	-	-	-
B6	-	-	-	-	-	-
B7	4.67	0.03	10269.40	1912.67	-	-
B8	-	-	-	-	-	-

Il Cielo come Laboratorio, 27
A.S. 2011-2012

Spectroscopic anaysis of the planetary nebula NGC7662

Lorenzo Conselvan, Davide De Grandis, Jacopo Magro, Giacomo Vecchiato

Liceo Scientifico Statale Ugo Morin Mestre-Venezia

Abstract. Our work concerned the analysis of the spectrum of the planetary nebula NGC 7662, located in Andromeda, to determinate from it some physical and chemical parameters such as temperature, electronic density and chemical abundance of the most present elements, in particular oxygen (OI , OII , [OIII]) and nitrogen (N). The basic datum was the bidimensional spectrum of the nebula, that we treated through the softwares IRAF (Image reduction and Analysis Facility) and TOPCAT. The tasks we mainly used were SPLOT in the package ONEDSPEC , to analyze the monodimensional spectra and TEMDEN used to calculate temperature and electronic density in the examined the regions of the nebula.
By the exam of the data we collected we found out that the temperature decreases of 2000 K from the central star to the 0.8 pc far gas shell and then increases in the most external regions. We also determined the chemical composition of the nebula, that is formed in the central region mainly by H, He, O, Ne, Ar and S, while in the others Ar and S disappeared, and the quantity of Fe increased.

1. Introduction

A planetary nebula is a gaseous object, with a white dwarf in its center. It is a phase of the stellar life: when a star of mass between 0.8 and 4 solar masses, that is a quite small star from the main sequence of the H-R diagram, has almost finished its H to be fused in He in its core, starts contracting and so it gets the temperature necessary to fuse H, C and O. The star gets a stratified structure where nuclear reactions between different elements have place in a different stratum. The C and O core contracts to start new reactions, but the mass of the star is non big enough to create the necessary pressure, so the system collapses, ejecting the external stratum. When they are ejected in the space they are stopped by the matter present in it. The star becomes a white dwarf that emitting UV radiations makes the gas become emissive. The sphere in which the gas, H in particular, is ionized and so visible, is called Strömgren sphere; beyond it the gas does not finish, but it is not visible to optical telescopes while it is detectable by radio-telescopes. NGC 7662, also called Blue Snowball Nebula, has two shells corresponding to two different strata in the star (Fig. 1).

The spectrum of the nebula was analyzed with the IRAF package ONEDSPEC which allowed us to obtain the flux, the wavelength and the errors of the spectral lines.

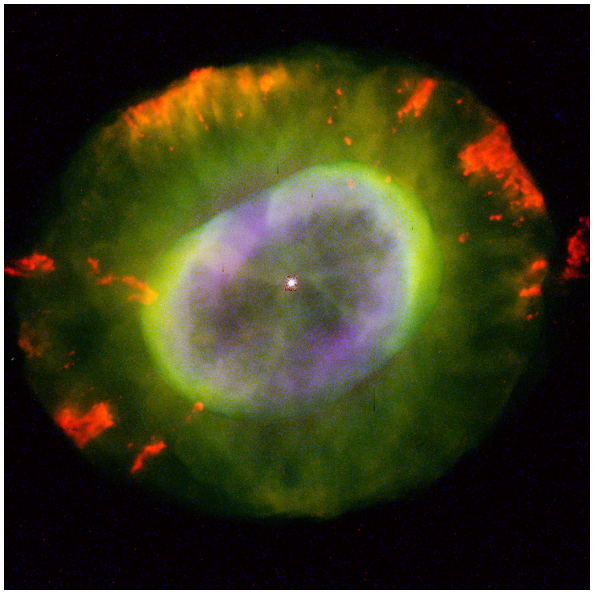

Fig. 1. Hubble Space Telescope (HST) image of NGC 7662.

2. Observational Data

The datum our work developed from was the bidimensional spectrum of NGC7662. A bidimensional spectrum is the spectrum of the region which is framed in the split of the spectrograph, and has in the x-axis the wavelength and in the y-axis the position across the split. The spectrum has been taken by the 1.22 m telescope in Asiago observatory, which has a Cassegrain setting, reflector with a parabolic and a hyperbolic mirror, and a 300 elements/mm spectroscopic grating. The

exposure time was of 30 s, and the scale is 1″/pixel. The spectrum we used had already been treated because the spectrum that the telescope takes is not ordered by flux and wavelength but by the electronic counts of the digital image. The object celestial coordinates are $\alpha_{2000} = 23^h25^m54^s$ and $\delta_{2000} = 42°32'6''$, and it is found near λ Andromedæ.

It has a radius of 0.8 ly and an apparent magnitude of 8.6, so it is quite bright, but there are no accurate measurements of its distance, that is about 1100 pc, so we cannot calculate with great precision its absolute magnitude. To make the various calculation we used a table of the possible emission lines of the main part of the elements at their wavelengths, that we used to recognize the elements of the nebula and a table of the extintion values at the various wavelengths.

3. Work description

The first operation we made on the spectrum was its division in 5″ wide regions (Fig. 2). To do it we used the IRAF task BLKVG that exports in a .fits image a given width and position part of the given spectrum. Putting each time the coordinates of each part we wanted to isolate we created a twentieth of monodimensional spectra, representing a dot region of the nebula, 16 of which were used for the spectroscopic analysis, because the most external regions were not bight enough to distinguish spectral lines from the deep sky radiation (Figs. 3–8). Each monodimensional spectrum was analyzed with the IRAF task SPLOT. It converts the spectrum from a black and white image in which the emission lines are brighter stripes to a wavelength/intensity graph in which emission lines are represented by a profile that can be analyzed like a gaussian. IRAF let us calculate various parameters of these gaussian curves such as the wavelength at the maximum, the flux (represented by the integral of the gaussian function), the FWHM (the width of the curve at half of its height), the equivalent width (the width of a rectangular stripe that is equivalent to the profile referred to the continuum), the width of the gaussian, the average intensity of the continuum and the standard deviation selecting in the IRAFTERM window with keyboard inputs the basal points and the top of the profiles, interpolating to them one or more gaussian functions. The data were tabulated using the software TOPCAT, dividing them according to the different elements. Through TOPCAT we calculated the error about the measured flux dividing the continuum standard deviation (rms) by the gaussian height (core). Then we had to calculate the extinction A_V by the equation 1. The intensity of the lines Hα ed Hβ is used as a reference.

$$\left(\frac{f_{H\alpha}}{f_{H\beta}}\right)_{intrinsic} = \left(\frac{f_{H\alpha}}{f_{H\beta}}\right)_{observed} \times 10^{(-0.1386 \times Av)} \quad (1)$$

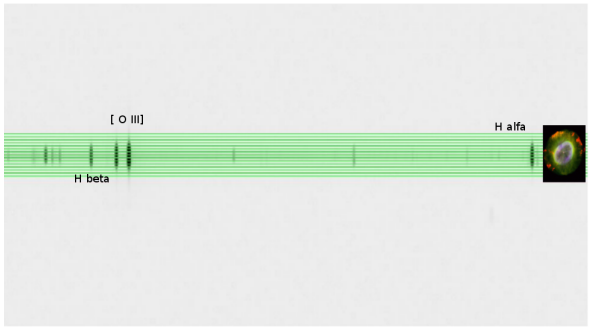

Fig. 2. Bidimensional spectrum with the division into regions.

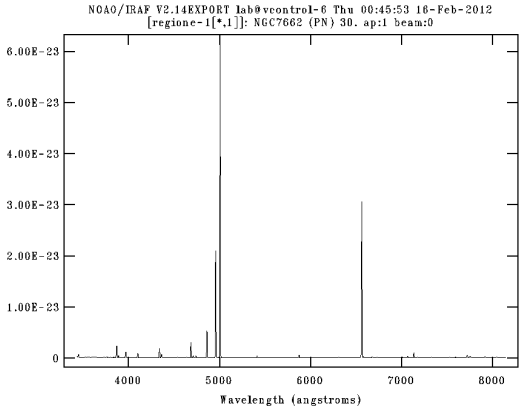

Fig. 3. Spectrum of the region at 5″ from the star.

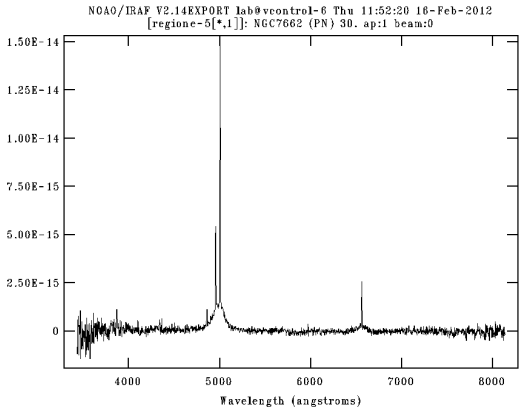

Fig. 4. Spectrum of the region at 25″ from the star.

The intrinsic ratio, measured in laboratory, is a constant and is equal to 2.86. But the extintion rises at the decrease of wavelength, so it is necessary to calculate a different coefficient A(λ) for each wavelength, which, put in the equation 2

$$A(\lambda) = A(V) \times k \quad (2)$$

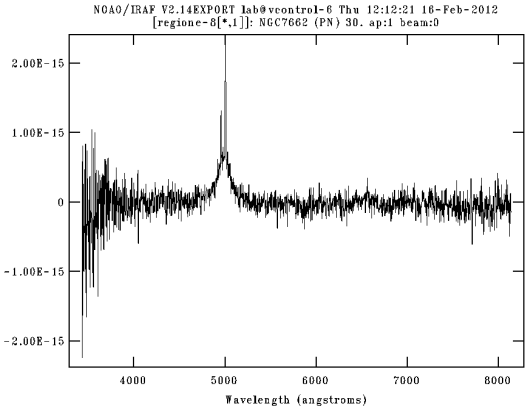

Fig. 5. Spectrum of the region at 40″ from the star.

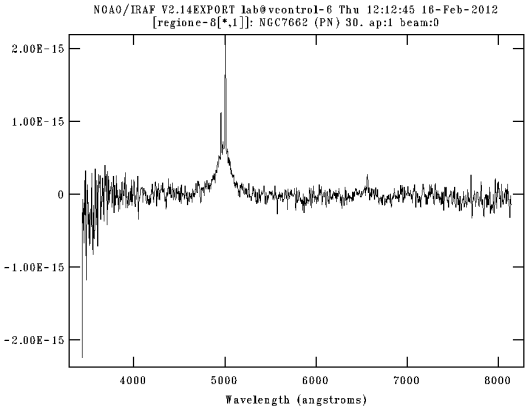

Fig. 6. The same spectrum as in Fig. 5 with an average smoothing of 3 pixels.

in which k depends from λ and was furnished in a table, allowed us to get the value of the extintion-corrected flux for each line in each region and the linked error ΔF,that is the relative error multiplied for the corrected flux. The density and temperature values for each region were calculated through the exam of the 6716 and 6731 Å [SII] lines and the 5007, 4959 and 4363 Å [OIII] ones. The data collected from these were elaborated through the IRAF task TEMDEN, which works in an iterative way: it means that at first we found a density value using a standard temperature for IRAF calculations, then we put the obtained density into the temperature calculation and its result in the density one, and so on, until the density and temperature data stabilized on the definitive ones. The values of the distance of the region from the central star were converted from pixels to pc with a trigonometric calculation based on the approximate nebula distance value found in literature. These data were organized in the Figs. 9 and 10.

The N and O chemical abundances calculations were based from the temperature, density and corrected flux data of some H, O and He lines through the equations 3,4,5 and 6.

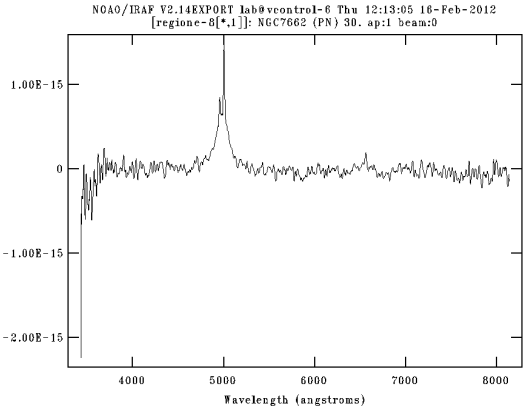

Fig. 7. The same spectrum as in Fig. 5 with an average smoothing of 7 pixels.

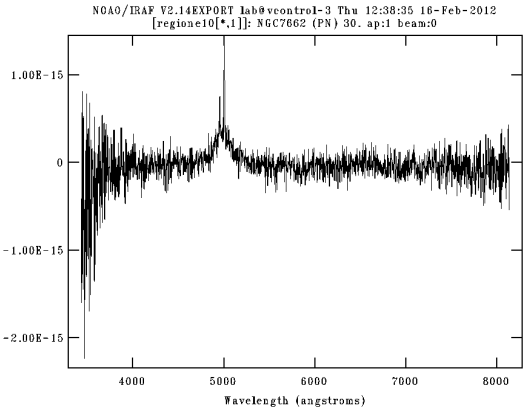

Fig. 8. The spectrum of the most external region at 50″.

$$12 + \log\left(\frac{\mathrm{OII}}{\mathrm{HI}}\right) = \log\left(\frac{I_{3727}}{I_{H\beta}}\right) + 5.89 + \frac{1.676}{t^2} - 0.40\log(t_2) + \log(1 + 1.35x) \quad (3)$$

$$12 + \log\left(\frac{\mathrm{OIII}}{\mathrm{HI}}\right) = \log\left(\frac{I_{4959} + I_{5007}}{I_{H\beta}}\right) + 6.174 + \frac{1.251}{t} - 0.55\log(t_2) + \log(t) \quad (4)$$

$$\left(\frac{\mathrm{OIII}}{\mathrm{OII} + \mathrm{OI}}\right) = 0.111 \cdot \mathrm{t}^{-0.13}\left(\frac{\mathrm{I}_{4686}}{\mathrm{I}_{5876}}\right) \quad (5)$$

$$\log\left(\frac{\mathrm{O}}{\mathrm{N}}\right) = \log\left(\frac{I_{3727}}{I_{6548} + I_{6583}}\right) - 0.307 + \frac{0.726}{t_2} + 0.02\log t_2 + \log\frac{1 + 1.35x}{1 + 0.116x} \quad (6)$$

where $t = T_e([OIII])/10^4$ K, $t_2 = T_e([OII]) = 0.243 + t(1.031 - 0.184 \cdot t)$, and $x = N_e/(\sqrt{t_2} \cdot 10^4)$. The data we obtained were organized in Tab.1.

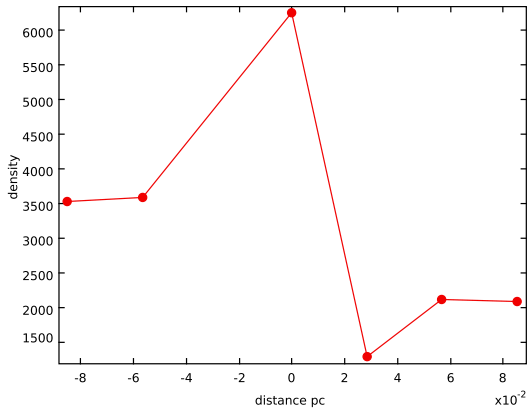

Fig. 9. Distance from the central star (in pc) vs. electron density (in e^- /cm^3).

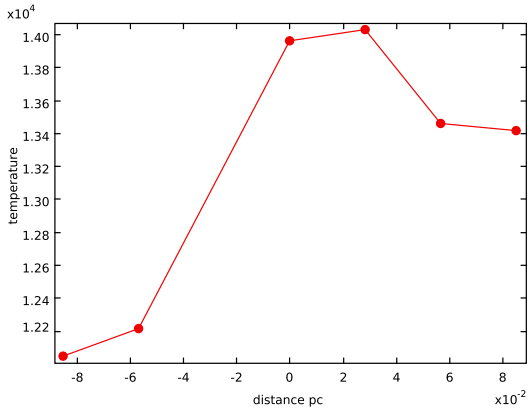

Fig. 10. Distance from the central star (in pc) vs. temperature (in K).

4. Results

Through the analysis of the spectrum of NGC 7662,at first examining some isolated regions of the spectrum and then its emission lines, we obtained the temperature, density and chemical abundances data of this planetary nebula with the softwares IRAF and TOPCAT, and in this way we came to the physical properties of the nebula at different distances from its centre. From the analysis of the emission lines we found an important presence of ionized Fe almost exclusively in the most external visible shell, while in the nearest regions to the star the gas composition consists mainly of H, He, Ne, Ar and S. This is due to the fact that the ionization energy of Fe (7.9 eV) is less than the ionization energy of other gases, for example H (13.6 eV) and He (24.8 eV), thus it is ionized in the colder region of the nebula. The data of temperature and density are consistent with those are reported in literature. In the area in which there is the star we could notice a temperature of about 14000 K, indicator of the white-bluish colour of the star, that is lower than the temperature of the region immediately surrounding the star, because the gas has been ejected at a certain temperature prolonged in time. From the observation of the distance-density graph we can notice the maximum in correspondence to the star, after a significant decrease and then another slight increase at the distance of about 0.06 pc from the centre, where the first shell starts. Around the star there are two shells, but from the graph only the first one can be detected because the density remains almost constant beside it. Probably, the shell surrounding the white dwarf was after the ejection of the external strata of a red giant when the amount of He that had to be fuse to maintain the hydrostatic equilibrium had finished.

References

Antonucci, R.R.J & Miller, J.S. 1985, ApJ, 297, 612
Antonucci, R. 1993, ARA&A, 31, 473
Cid Fernandes, R., et al. 2004, ApJ, 605, 105
Cid Fernandes, R., Mateus, A., Sodré, L., Stasińska, G., & Gomes, J. M. 2005, MNRAS, 358, 363
Pottasch, S. R., Beintema D. A., Bernarnd Salas, J. & Feibelman, W. A. 2001, å, 380, 684

Table 1. Reddening corrected fluxes (in units of 10^{-15} erg cm^{-2} s^{-1}), reddening, electron density and temperature, chemical abundances.

d(pc)	region	O III 3444	[O II] 3728	O III 3754	[Fe VII] 3760	H10 3799	H9 3837	[Ne III] 3869	He I 3890 3890	Hϵ 3969	He I 4027	[S II] 4069	[S II] 4076	Hδ 4101	Hγ 4339	[O III] 4362	[Fe II] 4452	He I 4471
0.17	6		9.96										7.72	5.82	5.6	6.08	7.21	
0.14	5		26.77	15.11						9.44				4.02	12.08	12.95		
0.11	4	41.4	18.8							90.03	10.98		6.43	28.97	74.92	45.75		10.92
0.09	3		352.69			120.17		338.58	386.89	1101.11	56.29			590.23	966.65	429.03		93.17
0.06	2		683.73		314.88		456.45	667.07	1048.55					1616.67	2686.25	1049.96		162.0
0.03	1		573.36				501.08		954.0	2579.78		86.1		1832.72	3131.74	1065.31		124.73
0.0	0		678.82	201.33		471.86	638.78	669.74		3196.9		129.13		2431.61	4099.08	1295.06		145.21
0.03	-1	1724.68	510.82			364.63	519.02	507.08	1022.68	3868.6	129.33			1903.44	3275.48	1151.78		156.23
0.06	-2	271.91	403.76			115.21	172.68	402.64	465.61	1226.48	58.65			682.9	1180.57	430.74		114.28
0.09	-3	10.1	50.08			11.01	15.46	50.65	45.92	111.82				58.45	102.94	40.5		
0.11	-4	9.39	5.26					5.23		11.12				10.49	17.68	10.75		
0.14	-5																	
0.17	-6																	
0.2	-7																	
0.23	-8		0.2															
0.26	-9																	

d(pc)	region	He II 4541	He II 4687	[Ar IV] 4710	[Ar IV] 4740	Hβ 4861	[O III] 4960	[O III] 5006	Fe II 5186	[N I] 5196	[Fe VII] 5276	He II 5411	[Fe II] 5520	[N II] 5760	He I 5875	[Fe VII] 6086	[Ca V] 6097	[S III] 6311
0.17	6		7.63			10.56	64.97	184.08	0.95						5.4			
0.14	5					19.14	136.3	406.25										
0.11	4		28.94	5.85	9.56	146.52	808.53	2435.77	4.45						14.94			7.08
0.09	3		455.88	108.21	85.41	1779.27	9722.18	29325.6				40.2			210.03	3.98		17.03
0.06	2	105.42	2984.44	402.38	339.31	5545.71	23778.34	70964.79				237.31			404.74			69.82
0.03	1		4980.55	527.27	473.91	6793.23	22064.46	65233.58				411.54			365.5			92.01
0.0	0	223.76	6655.9	704.12	683.88	8773.61	26733.47	78661.62				533.6			439.47			102.71
0.03	-1	150.19	4405.96	551.96	549.64	7097.06	26129.98	76642.48				355.32	25.56		499.29			
0.06	-2	19.16	470.87	133.34	109.01	2579.45	12483.09	37188.57	4.89	1.45		38.13	14.39	1.67	414.68		9.45	
0.09	-3	11.14	11.86	11.89	9.22	234.14	1227.17	3621.59							32.09		0.35	
0.11	-4		5.38			29.93	173.58	514.4			1.7				5.13			
0.14	-5					5.75	30.78	99.81									2.45	
0.17	-6					1.66	9.98	30.99										
0.2	-7					1.68	13.52	35.51										
0.23	-8					28007.55	4136972.23	9318992.06										
0.26	-9																	

d(pc)	region	[Ne II] 6451	[O I] 6302	[Ar V] 6435	Hα 6562	[N II] 6584	[Ne II] 6582	He I 6680	[S II] 6717	[S II] 6730	[Fe II] 6944	[Ar V] 7006	[Ar III] 7140	? 7280	[O II] 7325	? 7718	[Ar III] 7751 7751	? 8050	
0.17	6				30.21		2.88	1.58										9.45	
0.14	5				54.76		0.45	1.66						2.81					
0.11	4				419.27		2.15	2.42				1.2		23.67					
0.09	3				5091.69	45.4	6.61	67.17		12.04	16.34			153.3				56.77	
0.06	2				15866.31	138.92	19.57	130.72		27.71	37.75		44.15	456.42				102.93	
0.03	1				19431.7	146.89	111.99	108.56		27.35	32.25			505.71					
0.0	0			84.83	25097.35		6.95	133.4		20.74	36.72		180.76	586.06		34.84		145.88	
0.03	-1				20299.73		6.34	189.82						524.33	25.41	32.23	269.78		85.44
0.06	-2		7.7		7377.54		156.33	190.0	92.71	24.44	38.68			257.6			128.39	70.7	1.74
0.09	-3		0.47		669.54		17.49	17.98	8.43	2.74	4.32							9.94	
0.11	-4				85.6		2.25	1.55		5.18		1.66		1.75	1.12	1.01			
0.14	-5	1.74			16.44								0.83						
0.17	-6				4.75														
0.2	-7				4.8														
0.23	-8				80581.74		8903.27	25857.75											
0.26	-9																		

d(pc)	region	A(V)	$[SII]_{ratio}$	$[OIII]_{ratio}$	density	temperature	t	t2	x	$\frac{OI}{HI}$	$\frac{OII}{HI}$	$\frac{OIII}{OII+OI}$	$\frac{OIII}{HI}$	$\frac{O}{H}$	$\frac{O}{N}$	$\frac{N}{H}$
0.17	6	1.18		40.97												
0.14	5	0.98		41.89												
0.11	4	1.21		70.91												
0.09	3	1.27	0.74	91.02	2075.61	13409.68	1.34	1.29	0.18	3.41E-6	3.27E-4	0.23	7.65E-5	4.07E-4	10.52	3.86E-5
0.06	2	0.77	0.73	90.23	2108.25	13455.94	1.35	1.3	0.19	2.11E-6	2.53E-4	0.79	2.01E-4	4.56E-4	10.01	4.55E-5
0.03	1	0.34	0.85	81.95	1285.06	14024.5	1.4	1.33	0.11	1.23E-6	1.80E-4	1.45	2.61E-4	4.42E-4	5.16	8.57E-5
0.0	0	0.42	0.56	81.38	6237.21	13955.7	1.4	1.32	0.54	1.72E-6	1.69E-4	1.61	2.75E-4	4.45E-4	13.82	3.22E-5
0.03	-1	0.23		89.23												
0.06	-2	0.09	0.63	115.32	3575.25	12206.8	1.22	1.23	0.32	3.73E-6	3.32E-4	0.12	4.12E-5	3.77E-4	3.12	1.21E-4
0.09	-3	-0.35	0.63	119.71	3516.82	12041.5	1.2	1.22	0.32	5.22E-6	3.65E-4	0.04	1.48E-5	3.85E-4	3.8	1.01E-4
0.11	-4	0.21		64.01												
0.14	-5	-0.12														
0.17	-6	-0.34														
0.2	-7	0.45														
0.23	-8	12.98														
0.26	-9															

Il Cielo come Laboratorio, 33
A.S. 2011-2012

Spectroscopy of the planetary nebula NGC 7354

Artur Kryzhanovskyy[(1)], Mattia Gioele Prendin[(2)], Stefano Silvestrini[(1)]

[(1)] Liceo scientifico *G. Bruno*, Mestre
[(2)] Liceo scientifico *G.Galilei*, Dolo

Abstract.
We present an observational study of the planetary nebula NGC7354. The aim of this study was to determine the temperature and density of the nebula as a function of distance from the center; after the analysis was also possible to determine the intrinsic flux of each spectral line and recognized the abundance of certain elements such as Oxygen and Nitrogen as a function of Hydrogen. To achieve the objectives we analyzed the two-dimensional spectrum from which later were extracted one-dimensional spectra for each region identified. We researched and examined the emission lines of some elements to derive an intrinsic value of the flow, which was used to derive the values of temperature and density, and finally abundance of Oxygen and Nitrogen. The average temperature was around 9500 K and were not important differences as a function of distance from the center, instead the density tended to decrease with the removal the center.

1. Introduction

Planetary nebulae are the final stage of the life of stars of medium mass (0.8 a 5 M⊙). During its regular life, in the main sequence, the star burns hydrogen in the core, when the Hydrogen finished in the nucleus, the star burns hydrogen in a shell around the nucleus, while the core is stationary. The star is becoming a giant, when is sufficiently large, the nucleus of Helium shrinks and turns, converting the Helium in Carbon and Oxygen. There is a further expansion of the outer layers called shells. This phase is the horizontal branch in the HR diagram. When He finishes in the core, the star starts burning Hydrogen and Helium into two shells, while the core of C and O is inactive for its entire duration in the art asymptotic. Finally, when the nucleus of C and O tries to ignite, contracting its self, it does not find the conditions necessary power, and the external states are expanded again. The core does not have enough mass to continue to hold the more external layers together and fails to hamper expansion: it is creating the new planetary nebula.

The planetary nebula's nucleus is composed by C and O of the original star, which is very hot and it is called White Dwarf, it is surrounded by the envelope gas of the original star, that is still growing. The White Dwarf emits UV radiation that ionizes the gas, which is detectable in the visible spectrum. The ionizing radiation should be very energetic, like UV, because there are lines of Hydrogen which need photons of wavelength less than 912 Å to be ionized. The peculiarity of the spectrum of nebulae is to have a continuous profile added to one in emission. We studied the planetary nebula NGC 7354 , shown in Figure 1, which is located in the constellation of the Cepheids and is about 4200 ly far from the Earth (1,271 kpc). To achieve the objectives we analyzed the two-dimensional spectrum, which was divided into eleven regions, 5″ each. For all of these regions we created, by summing the spectra over the interval, one-dimensional spectra. In these spectra we examined the emission lines and extracted, through the software at-IRAF, some important parameters such as the observed flux. Then we estimated the extinction coefficient, we adjusted the flow and we determined the values of temperature, density and chem-

Fig. 1. Image of the planetary nebula NGC7354.

ical abundances of Oxygen and Nitrogen in relation to the amount of Hydrogen.

2. Observational Data

The image of NGC 7354 was obtained on the 31st of October 2001 with the Galileo Telescope 122cm at the Astrophysical Observatory in Asiago with a shutter speed of 1200 seconds. The specrograph was the Boller & Chievens. The diffraction grating composed by 300/mm with a fissure of 4.3″ . The CCD used is made up by 512x2048 pixels. The range of wavelength of spectrum was from 3400 Å to 8000 ÅThe coordinates of the object are:

Object	NGC 7354
Right Ascension	22:40:19.9
Declination	+61:17:8.1
Constellation	Cefeidi
Angular diameter	23 ″

3. Work description

We conducted a spectroscopic analysis of the planetary nebula NGC 7354, whose two-dimensional spectrum is in Figure 2 with the software IRAF.

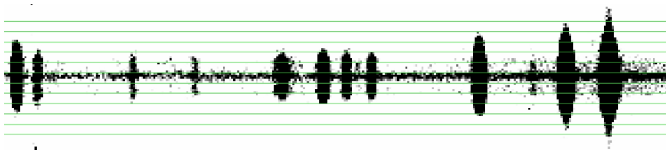

Fig. 2. Two-dimensional spectrum of the planetary nebula NGC7354.

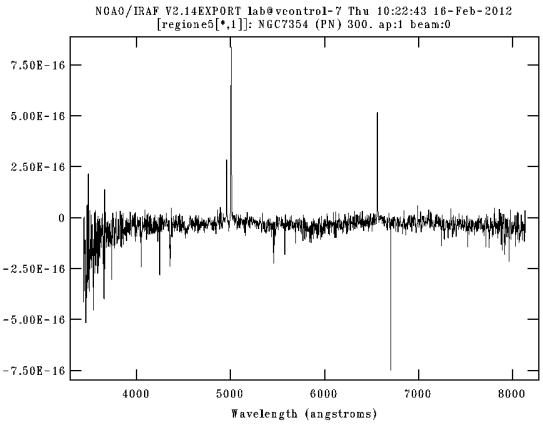

Fig. 3. One-dimensional spectrum of the external region, far about 15″ from the center.

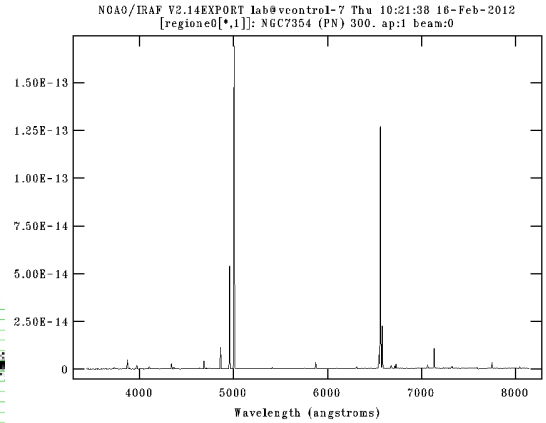

Fig. 4. One-dimensional spectrum of central region

We found the center of the two-dimensional spectrum. After that we divided it in 11 parts along the spatial direction. Each share has a dimension of 5 pixel which corresponded to 5″ because the spatial scale is 1″ /pixel. This operation was done using the task BLKAVG. We extracted their one-dimensional spectra which were then shown by SPLOTWe analyzed their emission lines: for each line we identified the wavelength of the top and then we interpolated the area below with a suitable Gaussian. Two examples are shown in Figure 3 and Figure 4, they represent respectively an external and the central region.

The software gave back on output the value of the area that represented the observed flux of photons of each lines we were interested in. After that we calculated the error linked with the flux's line. In order to calculate it we measured the standard deviation of the continuum, that is the background radiation without either lines of emission or absorption. Thanks to this analysis, for each region of the planetary nebula we obtained: chemical element and flux of the respective lines. In this way it was possible to determine the chemical composition of the different region. After the compilation of the file spot.log we created a table with these variables with the software gedit: for each analyzed region, the elements with their corresponding values of the flux, width of the Gaussian and standard deviation. We moved the new obtained table into Topcat, in Table 1.

We calculated the approximation error $\Delta F/F$ by dividing the standard deviation with the width of Gaussian, the absolute error ΔF by multiplying the observed flux of the line with the approximation error, and the signal/noise ratio $S/N = F/\Delta F$ by calculating the inverse of relative error. These operations were repeated for each element we found in the nebula. The absorption value in the visible A_V was calculated with the Cardelli, Clayton and Mathis (1989) formula, described by the equation in which the Balmer's decrease is used to determine the coefficient:

$$\left(\frac{F_{H\alpha}}{F_{H\beta}}\right)_{int} = \left(\frac{F_{H\alpha}}{F_{H\beta}}\right)_{oss} \times 10^{(-0.1386 \times A_V)} \quad (1)$$

Hα6563	A6563	rms6563	F(Hα)int
3.259E-15	5.631E-16	2.6E-17	
3.311E-14	4.94E-15	2.842E-17	4.442E-13
2.537E-13	3.553E-14	3.437E-17	6.263E-12
8.14E-13	1.119E-13	2.102E-16	1.654E-11
1.336E-12	1.808E-13	5.36E-16	3.335E-11
1.027E-12	1.392E-13	3.149E-17	2.757E-11
1.338E-12	1.83E-13	6.622E-16	3.365E-11
8.458E-13	1.163E-13	3.051E-17	3.138E-11
2.35E-13	3.191E-14	1.282E-16	8.872E-12
1.556E-14	2.031E-15	2.218E-17	3.209E-13
2.092E-15	2.641E-16	1.889E-17	

Table 1. Flux's values measured in erg cm^{-2} sec^{-1}, gaussian's width erg cm^{-2} sec^{-1} Å $^{-1}$, standard deviation in erg cm^{-2} sec^{-1} Å $^{-1}$ and intrinsic flux in erg cm^{-2} sec^{-1}

where the intrinsic ratio is known to be 2.86. The coefficient A_V represents a magnitude which is subtracted from the observed value to correct the extinction's effect of dust. Thanks to this value we calculated the intrinsic flux determined by the correction's value for each spectral line measured through equation 2:

$$F(\lambda)_{int} = F(\lambda)_{oss} \times 10^{0.4 \times A(\lambda)} \quad (2)$$

where $A(\lambda)$ is a coefficient which depends on wavelength, according to two polynomial equations, and on the extinction's coefficient according to equation 3.

$$A(\lambda) = A(V) \times \left[a(y) + \frac{b(y)}{3.1} \right] \quad (3)$$

where:

$$y = \frac{1000}{\lambda} - 1.82$$

$$a(y) = 1 + 0.17699 \times y - 0.50447 \times y^2 - 0.02427 \times y^3 + \\ + 0.72085 \times y^4 + 0.01979 \times y^5 - 0.77530 \times y^6 + 0.32999 \times y^7$$

$$b(y) = 1.41338 \times y - 2.28305 \times y^2 + 1.07233 \times y^3 - \\ - 5.38434 \times y^4 - 0.62251 \times y^5 + 5.30260 \times y^6 - 2.09002 \times y^7$$

After adjusting the fluxes of each line from the extinction's effect, it was possible to determine the density, measured in number of electrons for volume's unity, and the temperature, measured in Kelvin, in all the different regions of the planetary nebula; particularly we used lines of [S II] λ 6716, 6731 Å for the density and lines of [O III] λ 4363,4959,5007 Å for the temperature. After calculating the following ratios with equation 4 for the Sulfur and equation 5 for the Oxygen:

$$[S\,II]\frac{I(6716)}{I(6731)} \quad (4)$$

$$[O\,III]\frac{I(5007) + I(4959)}{I(4363)} \quad (5)$$

we used the task TEMDEN on the software IRAF to perform an iterative process which, assuming first an arbitrary temperature's value, calculated a density's value which was then used to determine a new temperature's value until the convergence of one value for the temperature and one for the density. Then we worked out the distance from the center of the planetary nebula for all of the regions converting pixel's distance into arcseconds using the following equation $r('') = r(px) \times scale('' /px)$ where the scale was $1'' /px$; distances were then transformed into parsec through the equation 6:

$$r(pc) = \frac{r('') \times d(pc)}{206265} \quad (6)$$

where Earth's distance, which is about 1271 pc, was extracted from literature. The constant, which divides, represents the number of arcseconds in a radian, assuming we could approximate the tangent with the angle. With these data we built up the graphs in Figure 5 and in Figure 6 that linked temperature and density of each region with the distance from the center of the nebula.

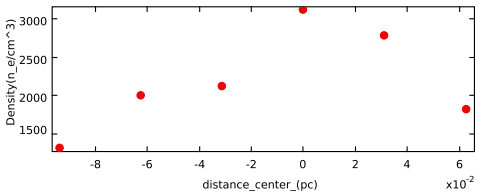

Fig. 5. Graph describing density as a function of the distance from the center.

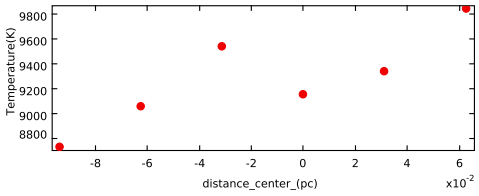

Fig. 6. Graph describing temperature as a function of the distance from the center.

From the graphs we could deduce that there is not a uniform distribution of both temperature and density; moreover for the temperature it is impossible to recognize a trend moving away from the center, whereas the density decreases as a function of the distance. Then it was possible to determine chemical abundances of Oxygen and Nitrogen through their ra-

tios with Hydrogen using the following equations 7 and 8:

$$\frac{O}{H} = \frac{OI + OII + OIII}{HI} \tag{7}$$

$$\frac{N}{H} = \frac{O}{H} \times \frac{N}{O} \tag{8}$$

The results are summarized in the general table in the appendix.

4. Results

The analysis concerned the planetary nebula NGC7354. The aim of our work was to determine a profile which attempted to describe the trend of temperature and density as a function of the distance from the center for each region; moreover it was possible to estimate chemical abundances of some elements, such as Oxygen e Nitrogen, through the comparison with Hydrogen. The process to obtain the results is described at point 3: we divided the two-dimensional spectrum into 11 regions of 5″ each, from which we extracted the one-dimensional spectra. From these spectra we obtained the observed fluxes, Gaussian's values which interpolated spectral lines, which were then corrected from the extinction's effect. Once we got the intrinsic fluxes we went on with the analysis of temperature, density and chemical abundances. The results demonstrate a temperature's value which varies in a 1000 K range from one of the furthest region to the other, from a minimum of 8800 K to a maximum of 9800 K. This inequality is not so significant because if we considered the experimental errors, estimated about 1 out of 10, temperatures are not likely to be so different, which let us thinking of an average temperature of 9500 K. Regarding density we worked out a maximum value of approximately 3100 e^-/cm^3 in the central region: getting far from the center we found a decrease down to about 1300 e^-/cm^3. The chemical abundances of Oxygen and Nitrogen were determined linked to the Hydrogen's abundance; in certain regions there are not these values of abundances because there were not the lines needed in the ratios. The abundances of Oxygen and Nitrogen are similar in all regions and they worth 8.4×10^{-4} for the Oxygen and 4.9×10^{-4} for the Nitrogen. The results seem to agree with those derived from literature (Contreras, Vazquez, Miranda, Olguìn, Zavala & Ayala 2010) .

References

Contreras, Vazquez, Miranda, Olguìn 2010

regione	F[ArIII]	err_ass[ArIII]	F[OII]	err_ass[OII]	F[OII]	err_ass[OII]	F[ArIII]	err_ass[ArIII]	F[SII]	err_ass[SII]
regione5										
regione4							0,264	0,002		
regione3							3,021	0,002		
regione2	1,579	0,003					7,459	0,009	0,911	0,002
regione1	3,364	0,004					15,956	0,012	4,531	0,002
regione0	3,198	0,004					15,085	0,009	4,400	0,002
regione-1	3,699	0,004	1,774	0,012	1,764	0,010	17,824	0,011	5,329	0,002
regione-2	3,288	0,004					16,362	0,004	4,285	0,002
regione-3	0,734	0,002					4,823	0,003	1,378	0,001
regione-4							0,157	0,002		
regione-5										

Table 2. Flux's values measured in 10^{-17}erg cm^{-2} sec^{-1}, standard deviation linked in 10^{-17}erg cm^{-2} sec^{-1}.

F[SII]	err_ass[SII]	F(HeI)	err_assHeI	F[NII]	err_ass[NII]	F(Halfa)	err_assHalfa	F[NII]	err_ass[NII]
							0,002		
				0,387	0,002	4,442	0,002		
				7,566	0,003	62,629	0,002	3,577	0,003
0,680	0,002	1,669	0,003	19,468	0,021	165,422	0,015	7,942	0,018
2,999	0,002	3,327	0,004	73,370	0,041	333,510	0,040	27,131	0,041
2,826	0,002	2,817	0,002	53,725	0,003	275,739	0,002	19,574	0,002
3,797	0,002	3,023	0,002	79,509	0,048	336,518	0,048	26,473	0,046
3,088	0,002	2,998	0,002	67,709	0,002	313,808	0,002	23,461	0,002
1,116	0,001	1,257	0,001	16,844	0,010	88,724	0,009	6,561	0,010
				0,379	0,002	3,209	0,002	0,290	0,002
							0,001		

Table 3. Flux's values measured in 10^{-17}erg cm^{-2} sec^{-1}, standard deviation linked in 10^{-17}erg cm^{-2} sec^{-1}.

F(HeI)	err_assHeI	F(HeII)	err_assHeII	F[OIII]	err_ass[OIII]	F[OIII]	err_ass[OIII]	F(Hbeta)	err_assHbeta
					0,002		0,002		
0,257	0,002			21,011	0,002	7,410	0,002	1,553	0,002
3,047	0,002			305,277	0,002	102,767	0,002	21,900	0,003
5,552	0,003			766,044	0,003	258,997	0,002	57,844	0,002
10,143	0,003			1312,871	0,002	451,429	0,004	116,621	0,002
9,579	0,002			1196,452	0,004	402,112	0,005	96,420	0,003
10,346	0,003	4,669	0,003	1393,637	0,004	469,564	0,004	117,673	0,002
12,692	0,002			1570,979	0,004	526,632	0,004	109,733	0,004
4,756	0,002			429,400	0,002	146,614	0,002	31,025	0,001
				12,511	0,001	4,326	0,002	1,122	0,002
					0,001		0,002		

Table 4. Flux's values measured in 10^{-17}erg cm^{-2} sec^{-1}, standard deviation linked in 10^{-17}erg cm^{-2} sec^{-1}.

F[ArIV]	err_ass[ArIV]	F[ArIV]	err_ass[ArIV]	F(HeII)	err_assHeII	F[OIII]	err_ass[OIII]	F(Hgamma)	err_assHgamma
								12,540	0,003
				28,139	0,014	10,124	0,004	29,041	0,002
				71,621	0,013	15,392	0,004	60,363	0,003
				46,279	0,008	13,254	0,003	54,145	0,003
6,407	0,002	7,977	0,003	64,081	0,004	17,471	0,002	62,832	0,002
4,867	0,001	6,698	0,002	42,080	0,003	18,125	0,002	63,009	0,002
						4,343	0,002	17,960	0,002

Table 5. Flux's values measured in 10^{-17}erg cm^{-2} sec^{-1}, standard deviation linked in 10^{-17}erg cm^{-2} sec^{-1}.

F(Hdelta)	err_assHdelta	F[NeIII]	err_ass[NIII]	F(H8)	err_assH8	F[NeIII]	err_ass[NeIII]	F[OII]+	err_ass[OII]+
6,722	0,002					36,295	0,005		
22,066	0,003	37,124	0,004	13,137	0,004	86,154	0,009		
45,044	0,003	69,656	0,006	26,859	0,004	164,247	0,008	52,209	0,007
38,345	0,003	65,047	0,005	24,693	0,003	156,133	0,006	36,821	0,006
45,723	0,003	74,763	0,007	31,111	0,008	172,006	0,008	57,099	0,010
45,663	0,003	88,824	0,004	37,837	0,004	205,199	0,004	54,498	0,008
		24,17		7,578	0,003	51,866	0,003		

Table 6. Flux's values measured in 10^{-17}erg cm^{-2} sec^{-1}, standard deviation linked in 10^{-17}erg cm^{-2} sec^{-1}.

Temperatura(K)	Densita(e^-/cm^3)	Oxygen_abundance_(O/H)	Nitrogen_abundance_(N/H)
9837	1807		
9331	2778	8,41	5,00
9145	3116	8,27	4,84
9527	2117	7,90	4,90
9049	1997	8,72	4,68
8719	1302		

Table 7. Values of Temperature measured in Kelvin, density in e^-/cm^3 and chemical abundances ($\times 10^{-4}$) as pure numbers

Il Cielo come Laboratorio, 39
A.S. 2011-2012

The morphology of the galaxy NGC 2768

Mattia Bertesina[1], Tommaso Bocca[2], Luigi Mattiello[1], Giovanni Munaretto[1]

[1]Liceo G.B. Quadri, sez. Tecnologico, Vicenza
[2]Liceo D.G. Fogazzaro, sez. Tecnologico, Vicenza

Abstract. In this work we studied the morhology of the galaxy NGC 2768. The main goal was to determine its morphological class. To this end, we analyzed three galaxy images taken with different filters: *g*, *r* and *i*, extracted from the Sloan Digital Sky Survey (SDSS) archive. We determined morphological type and also the luminosity of NGC 2768 by studying the isophotes of its projected structure. Our work show that this object is an E6 elliptical galaxy. Moreover, we found faint evidences of the effect of interaction with the surrounding environment.

1. Introduction

The morphological classification of galaxies, introduced by Edwin Hubble in 1936, divides galaxies in four different groups: elliptical galaxies (E), lenticular galaxies (S0, SB0) spiral galaxies (normal S and barred SB) and irregular galaxies (Irr). The morphological classification of a galaxy is important because it is linked to its structure and evolution. Historically, the first works were based on the visual inspection of the obtained images. After the introduction of CCD in astronomy, more quantitative and objective methods of investigation were introduced. One of the most important and useful is the analysis of the isophotes. Isophotes are lines that link together pixels having the same intensity; these lines are conveniently approximated with ellipses, so that it is possible to parametrize the isophotes. Pratically, the analysis of the geometry of such ellipses give us the semi-major and semi-minor axis values, a and b respectively, the position angle (PA), that is the orientation of the semi-major axis with respect to a fixed direction, normally the north, the coordinates of the center of the ellipses, and the ellipticity, that is the quantity: e = 1 − b/a. NGC 2768 have not a precise morphological classification. It is often classified as E5/E6 (e.g. Strom et al. 1978), but also as S0 (Crocker et al. 2008). It is also reported as a LINER (Smith et al. 2000). In Crocker et al. (2008), it is also evidenced that there could be a molecular ring, due to the interaction of the galaxy with the surrounding matter. In this work, having images taken in three photometric bands (*g, r, i*), we studied the morphology and surface brightness profile of NGC 2768.

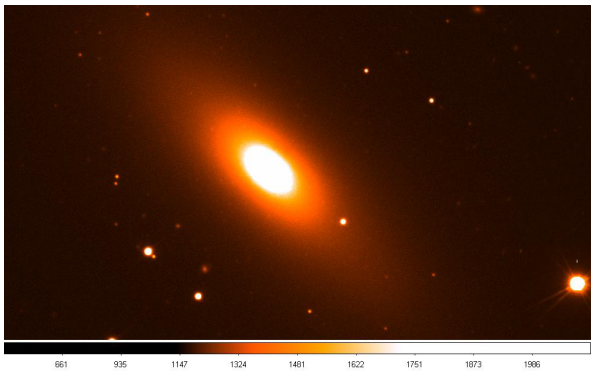

Fig. 1. NGC 2768 – *r* band.

2. Observational Data

The images analyzed were extracted from the Sloan Digital Sky Survey (SDSS) archive, taken in the *g*, *r* and *i* photometric bands of the *ugriz* photometric system. The exposure time of each frame is 53.9 seconds, while the pixel scale is: 0.4 ″/pixel. The Table 1 reports some general information and data of NGC 2768, obtained from the Nasa Extra-galactic database (NED).

Table 1. Data of NGC 2768.

RA (J2000)	9h 11m 37.5s
Dec (J2000)	+60º 2’ 14”
RV(Km/s)	1373 ± 5
z (v/c)	0.00458 ± 0.000017
d (Mpc)	20.067 ± 3.098

3. Work description

Data were analyzed with IRAF software. First, we made the isophotes fitting with variable center, to elaborate the graphs of the geometry of fitted ellipses, a model of the galaxy and to spot any residuals. To do this, with the DS9 software, we drew a generic ellipse that enclosed the whole galaxy in its area and we set up its parameters for the fit. Initially we set to "no" the HCENTER parameter, so that the fitted ellipses had not a fixed center. We also carefully masked any light sources that could affect the fit (e.g. field stars). Hence, the IRAF task ELLIPSE allowed us to execute the isophotes fit. During the fit we also considered the stop code value. The stop code value is a indicator of the quality of the fitted isophote. It can assume three values, related to the fitting quality . In particular, it tells us whether the fit of the ellipse is optimal, if the maximum number of iterations were reached, or if the fit failed. In our case, we discarded any failed fit.

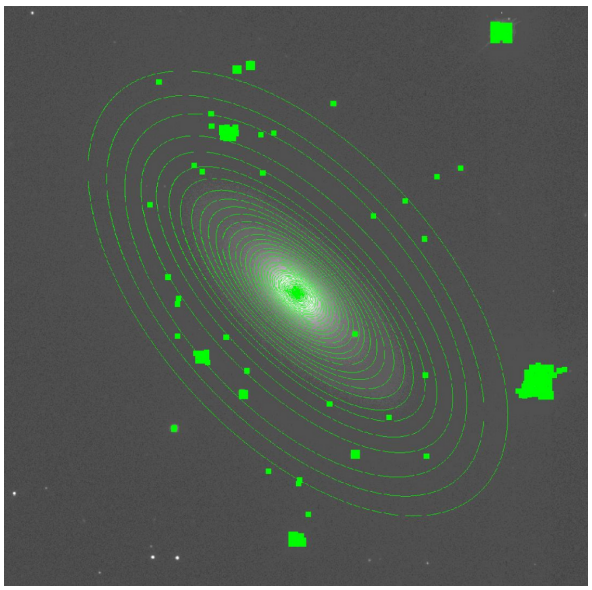

Fig. 2. NGC2768 galaxy – masks and fitted isophotes.

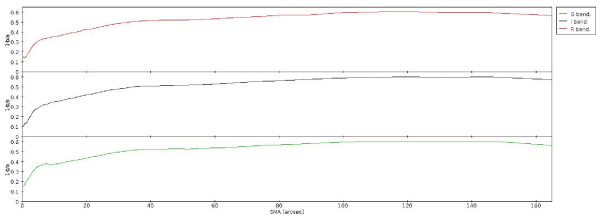

Fig. 3. Ellipticity versus semi-major axis in the three bands *g*, *r* and *i*.

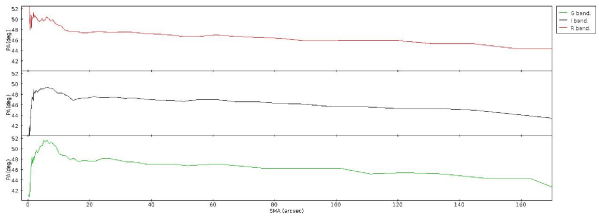

Fig. 4. Position angle versus semi-major axis in the three bands *g*, *r* and *i*.

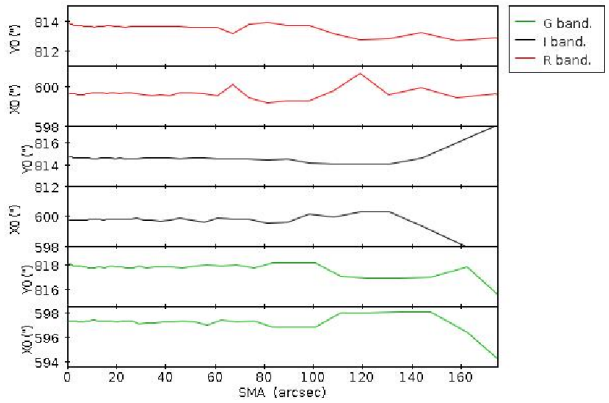

Fig. 5. coordinates of the centers versus semi-major axis in the three bands *g*, *r* and *i*.

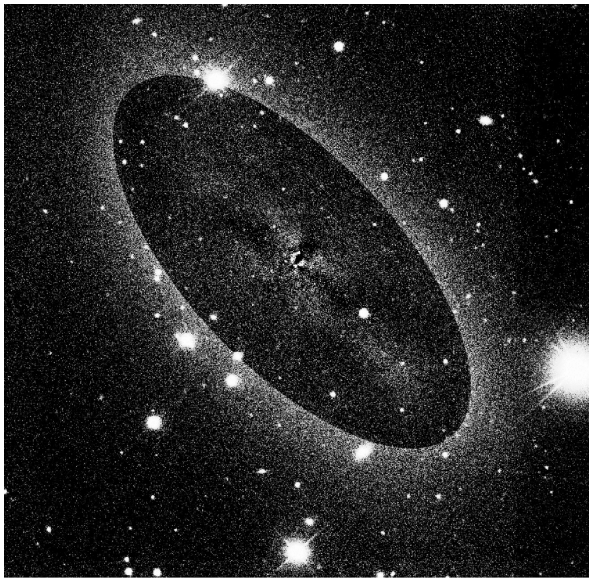

Fig. 6. NGC2768 galaxy – *i* photometric band: (O–C).

The fitted ellipses parameters give us the estimated galaxy center, and hence we repeated the isophotes fit with this input value to improve the fit itself. Thanks to the isophote fitting, with the IRAF's task BMODEL we built a model of the galaxy. To that end, the background sky mean level was determined and subtracted. Once we obtained the model, we got the residuals by subtracting it to the galaxy original image 6. The residuals show a non–zero signal within the central regions of the galaxy. This may represent a substructure inside an ordinary elliptic one. Indeed, Crocker *et al.* (2008) found in the inner regions a rotating molecular polar disc.

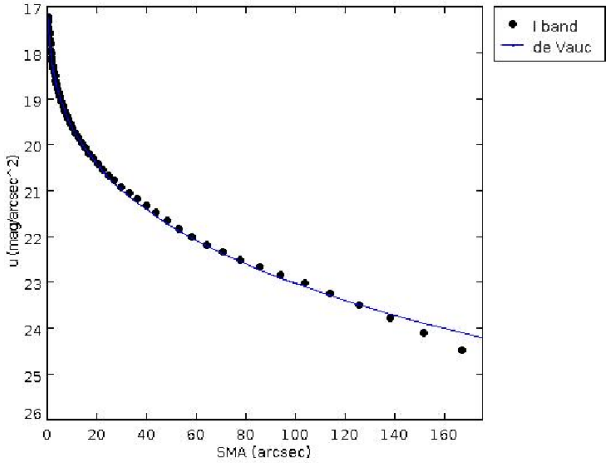

Fig. 7. Surface brightness – *i* band.

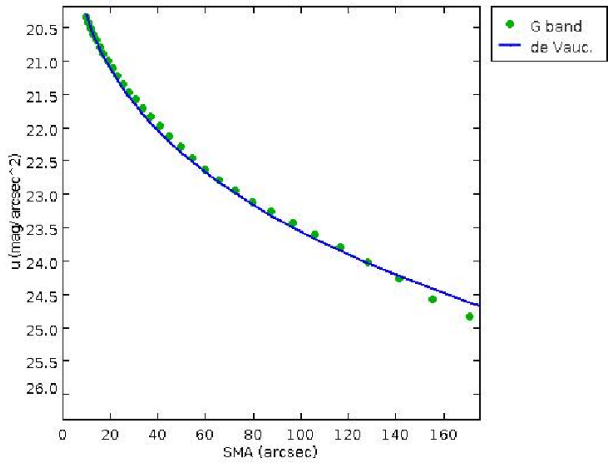

]

Fig. 8. Surface brightness – *g* band.

We converted the semi-major axis from pixel to arcsec (Eq. 1) and the area of each isophote into squared arcsec (Eq. 2). We computed the instrumental intensity by subtracting the background mean value, and then the surface brightness of the galaxy using Eq. 3.

$$r = sma \times 0.4 \tag{1}$$

$$A = n_{pix} \times 0.4^2 \tag{2}$$

$$I_{sup} = \frac{I_\star - < I_{sky} > \times n_{pix}}{t_{exp} \times A} \tag{3}$$

In Eq. 3 $I_\star$ is the intensity of the ring between two consecutive ellipses, $< I_{sky} >$ is the mean sky intensity determined by the task IMEXAMINE, n_{pix} is the number of pixels contained in each ring, t_{exp} is the exposure time and A is the area of each ring in squared arcsec. In this way we obtain the surface brightness profile. We fit these data by adopting the de Vaucouleurs' relation:

$$I(r) = I_e \times e^{-7.67\left[\left(\frac{r}{r_e}\right)^{0.25}-1\right]} \tag{4}$$

In Eq. 4 r is the semi-major axis, I_e is the surface brigthness at the effective radius r_e, the radius of the circle containing half of the luminosity of the galaxy. I_e and r_e are the two parameters set to make the curve fitting to our data as good as possible. Even if the de Vaucouleurs' law was the most satisfactory to fit the surface brightness profile and any attempt to fit data with more complex laws does not given meaningful result, the Figures 9 and 10 show that there is an eccess of signal compared to the de Vaucouleurs' law. This enforce our hypothesis about the presence of a substructure in the inner region of the galaxy. With the de Vaucouleurs' model we found the total intensity, hence computing the instrumental magnitude (μ_s). Below, the employed relations. Intensity:

$$I = 22.66 \times I_e \times r_e^2 \tag{5}$$

Magnitude:

$$\mu_s = -2.5\log(I) \tag{6}$$

The instrumental magnitude was subsequently corrected by removing the instrumental zero-point and taking into account the atmospheric extinction, with the Eq.7:

$$\mu = \mu_s + m_0 - k \times x \tag{7}$$

where μ is the corrected magnitude, m_0 is the zero point, and $k \times x$ represent the atmospheric extinction, given by multiplying the airmass x by the extinction coefficient k, that is related to the given photometric band. We measured the absolute magnitude (M) using the Eq. 8:

$$M = m + 5 - 5 \times \log(d) \tag{8}$$

where d is the distance in parsec of the galaxy (Table 1). Finally, the luminosity was computed as follow:

$$\frac{L}{L_\odot} = 10^{0.4\times(M_\odot - M)} \tag{9}$$

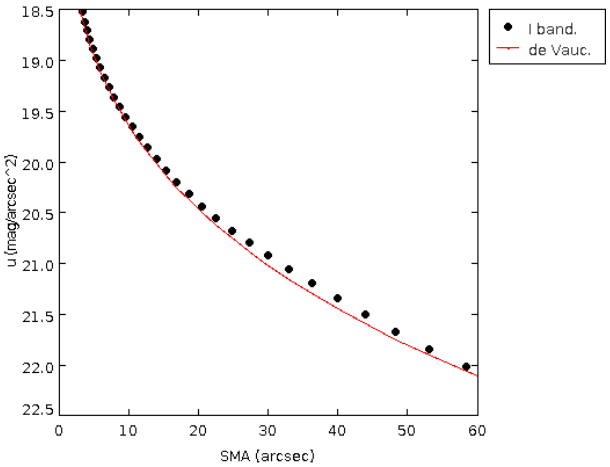

Fig. 9. Surface brightness – *i* band. From 0″ to 60″.

Table 2. Calibration coefficients.

	g	*r*	*i*
μ_0	24.4685	24.0532	23.6789
k	0.187	0.112	0.063
x	1.186	1.181	1.182

where $L_\odot$ is the solar luminosity. The Table 3 show the parameters of the de Vaucouleurs' function and the galaxy luminosity at the effective radius r_e.

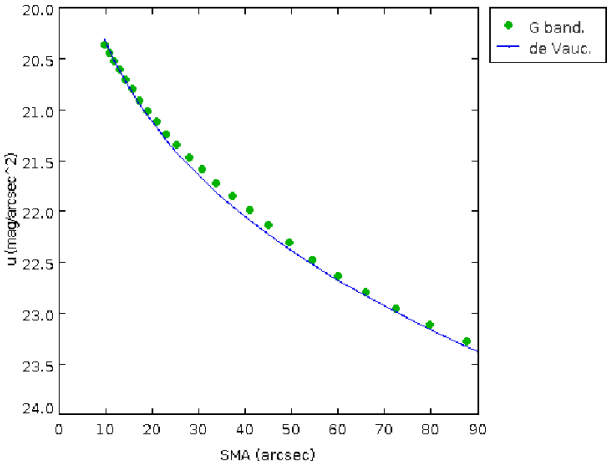

Fig. 10. surface brightness – *g* band. From 0″ to 90″.

4. Results

We studied the morphology of NGC 2768 galaxy using *g*, *r* and *i* images. The images were extracted form the SDSS archive. Isophotes were fitted as ellipses, obtaining ellipticity, PA and center coordinates as a function of the SMA. Also the brightness profile was computed and fitted adopting the de Vaucouleurs' law and determining the galaxy luminosity. The surface brightness profiles in the *g* and *i* bands show a small signal excess with respect to the de Vaucouleurs' curve between 30–50 arcsec. The graphs of the PA and ellipticity show an irregular trend in the inner region while they remain almost constant in the outer part. However the variation of position angle are very small and comparable with the computational errors (about 5 degrees). To summarize, in agreement with literature, we can suggest that NGC2768 is a peculiar elliptical galaxy, with an inner substructure maybe due to its interaction with surrounding companion galaxies.

Table 3. Results of the photometric analysis.

band	μ_e (mag)	r_e(″)	$L/L_\odot$
g	24.5	160	5.74×10^{10}
r	23.5	125	8.79×10^{10}
i	23.5	125	8.89×10^{10}

5. Bibliography

Crocker A. F., Bureau M., Young L. M., Combes F., 2008, MNRAS, 386, 1811
Strom K. M., Strom S. E., Wells D. C., Romanishin W., 1978, ApJ, 220, 62
Smith R. J., Lucey J. R., Hudson M. J., Schlegel D. J., Davies R. L., 2000, MNRAS, 313, 469

Il Cielo come Laboratorio, 43
A.S. 2011-2012

Stellar velocity dispersion and mass of the galaxy NGC 2768

Riccardo Caneve[1], Francesca Del Favero[2], Rebecca Valcozzena[3], Lorenzo Zandonella[2]

[1]Liceo Galilei, sez. scientifico, Belluno
[2]LIceo Fermi, sez. scientifico, Pieve di Cadore
[3]Liceo Follador, sez. scientifico, Agordo

Abstract. The aim of our work is the calculation of the mass of the galaxy NGC 2768 based on the measurement of velocity dispersion and effective radius. Making use of the IRAF program and the package FXCOR, we processed the spectra of the galaxy and the star HD 78821. The stellar spectrum was convolved with Gaussian functions of increasing σ values, and then correlated with itself and with the galaxy spectrum, to obtain the velocity dispersion and the rotation curve. Ww studied the isophotes of the galaxy with the ELLIPSE package, we calculated the brightness profile, and by applying the empirical laws of De Vaucouleurs and Freeman, we estimated the effective radius, that combined with the stellar velocity dispersion gave us the mass of the galaxy.

1. Introduction

The different shapes of galaxies depend on the dynamic conditions in which they formed, from the primordial cloud to the gravitational interactions with the nearest galaxies. The morphological classification, proposed by Hubble and still valid, distinguishes the galaxies in elliptical, lenticular, spirals and irregulars. *Elliptical galaxies* have a circular or elliptical shape, and are classified according to their ellipticity, from spherical (E0) to highly elliptical (E7). In these galaxies it is little evident the presence of gas and dust, since they are composed almost exclusively by old stars, even older than 10^{10} years. They have low rotation and their spectra show absorption lines of heavy elements, such as calcium, magnesium, iron, sodium, etc. Their colors are orange and red, because their light is dominated by class K and M stars. *Spiral galaxies* are classified from Sa to Sd, according to how the arms are wound: from tightly to loosely wound. They are formed by a luminous central bulge and a flattened disk, rich in young stars, dust and especially gas. In the bulge we can find mainly population II stars, while in the arms popula-

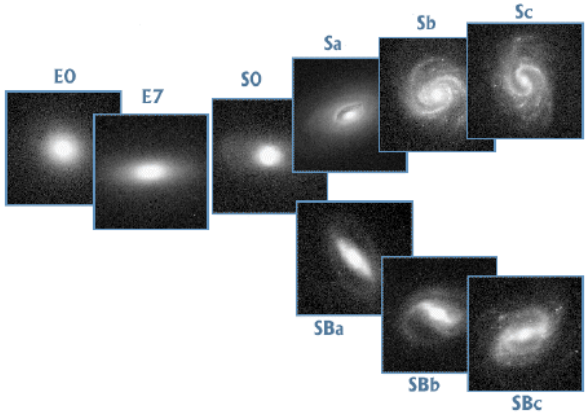

Fig. 1. Hubble diagram of the morphological classification of galaxies. Real galaxies are used in this illustration.

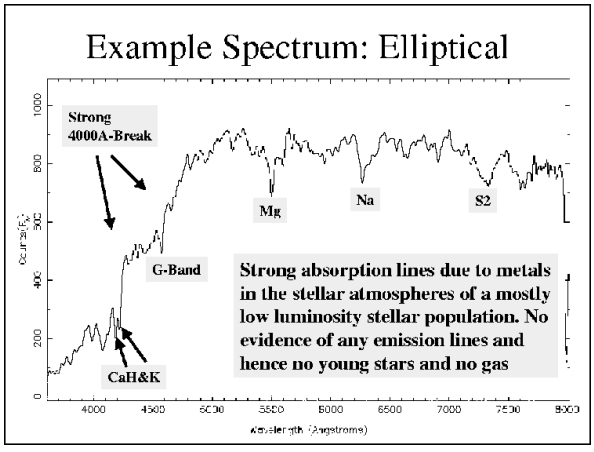

Fig. 2. Example of a typical elliptical galaxy spectrum.

tion I. In spiral galaxies the ordered motions of rotation around an axis perpendicular the disc dominate. The spirals are divided into ordinary (S) and barred (SB): the S have arms which start directly from the core, while the SB have an oval-shaped bulge with a bar whose apices are connected to the arms.
A particular kind of galaxy is represented by *lenticular* galaxies: these are also composed of a bulge and a disk, but without spiral arms. The bulge is very big, in comparison to the disk and even more massive; briefly, they are disk galaxies where star formation has stopped long time in the past due to the exhaustion of interstellar matter, and they are mostly made up of old stars.
At last we have a class of galaxies called *irregular*, with many structures and configurations.
Some recent observations have found blue and young open clusters in some elliptical galaxies, along with other structures that can be explained by galaxy mergers. In this new frame, the elliptical galaxies are the result of a long process where two or more smaller galaxies, of any type, collide and merge into a single more massive object.
From the kinematic point of view, namely the distribution of the motions of the stars which compose them, the elliptical galaxies are systems where the chaotic motions dominate; in spiral galaxies, on the contrary, ordered rotational motions dominate. The dispersion

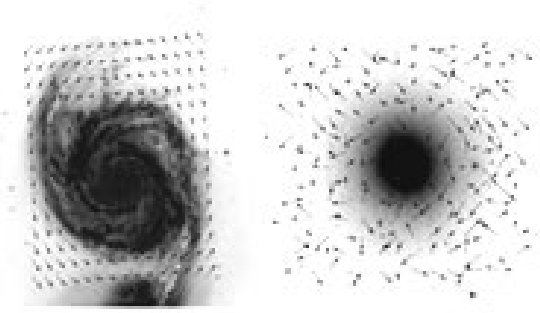

Fig. 3. Distribution of the motions in galaxies. Elliptical galaxies, on the right: the stars are distributed on orbits of different shapes and inclinations, that originate chaotic motions. Spiral or disk galaxies, on the left, are dominated byrotational motions around an axis perpendicular to the disk on which most of the stars is distributed.

velocity σ, is the quantity that measures the chaotic motions of the stars. In general in elliptical galaxies σ shows high values in the center, while in spiral galaxies these values are significantly lower. On the contrary, the rotation velocities are high in spiral galaxies and low in elliptical galaxies. So it is believed that what contrasts to the gravitational collapse in elliptical galaxies is the high velocity dispersion, and that spiral galaxies maintain their dynamic equilibrium by means of high rotation velocity.

Datum	Value
RA (J2000)	$09^h\ 11^m\ 37.40^s$
Dec (J2000)	$+60°\ 02'\ 14.0''$
Class	E6 (NED) ; E/S0 (SIMBAD)
Size	$6.3' \times 2.8'$; PA= 95°
Magnitude	10.1

Table 1. Data of the galaxy NGC 2768.

Datum	Value
RA (2000)	$09^h\ 12^m\ 36^s$
Dec (2000)	$+56°\ 18'\ 06''$
Apparent magnitude	8.3
Spectral type	K

Table 2. Data of the star HD 78821.

2. Observational Data

We analyzed the elliptical galaxy NGC 2768. It is located in Ursa Major constellation. In Table 1 there are the coordinates and other data of the galaxy (SIMBAD database).

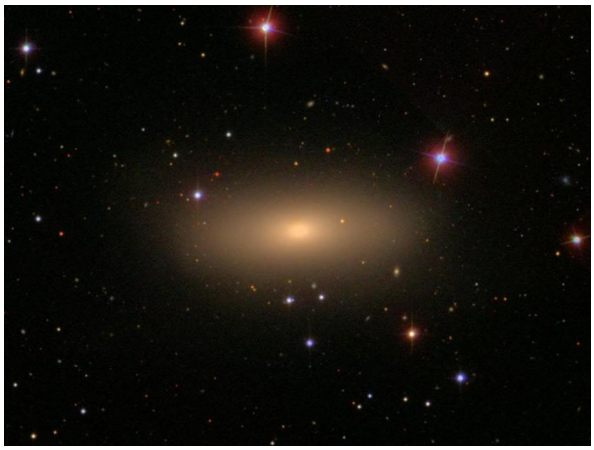

Fig. 4. Image of the galaxy NGC 2768.

We also considered the star HD 78821. Table 2 shows coordinates and some properties (SIMBAD database).

The galaxy spectrum was taken on January 26th, 2012 with the 1.82-m telescope of Padova Astronomical Observatory (OAPd/INAF) situated on cima Ekar (Asiago, Italy) with the Asiago Faint Object Spectrograph and Camera (AFOSC) and the grism nr. 4.

The considered wavelength range was between 5300 and 7800 Å. The slit was aligned along the major axis of the galaxy and it was 1.26″ wide; the exposure time was 3600 seconds. The spectral resolution was 13 Å.

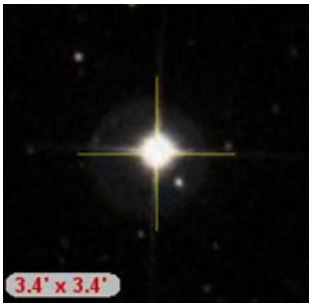

Fig. 5. Image of the star HD 78821.

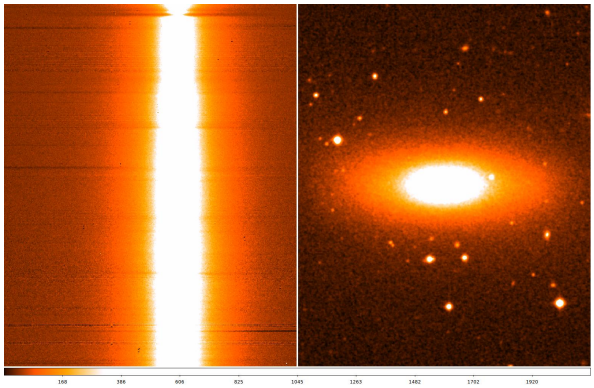

Fig. 6. The spectrum of the galaxy NGC 2768.

3. Work description

Since we know that a strong broadening of the spectral lines corresponds to a high velocity dispersion, we compared the spectra of the galaxy NGC 2768 and the star HD 78821. We correlated the stellar spectrum with itself, but convoluted with Gaussians of increasing σ, from 50 km s^{-1} to 400 km s^{-1}, with steps of 50 km s^{-1}, focusing on the absorbtion line of Na I, λ = 5892 Å.

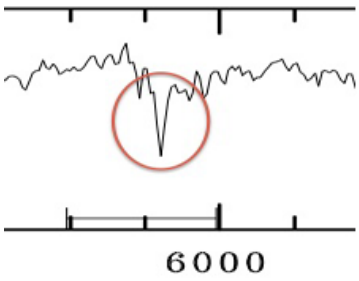

Fig. 7. Detail of the NaI line.

In this way, the broadening of the lines, due to the caotic motions of the stars, can be interpreted in terms of a spectrum of a single star convoluted with a Gaussian function. This fuction represents the statistical distribution of the stellar radial velocities and its σ is the stellar velocity dispersion. The objective is to find a relation between the Full Width at Half Maximum (FWHM) of the correlation peak and the velocity dispersion. With the program IRAF and the task FXCOR, which applies the method of the Fourier cross correlation to derive the radial velocities, we calculated the cross correlation function and we measured the FWHM of the peak (Figure 8). We then constructed a graph by

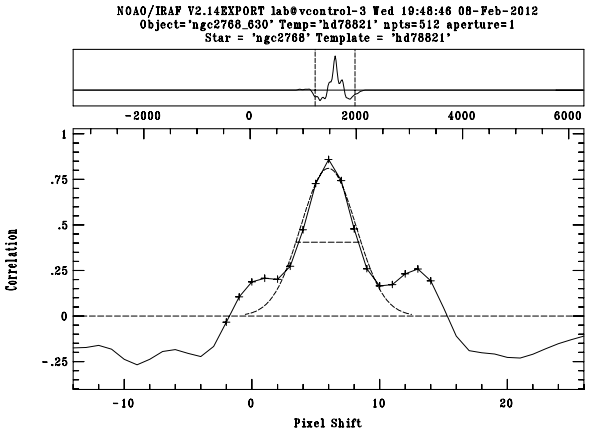

Fig. 8. The correlation spectrum of the star with itself. On the top, the correlation function, on the bottom, a zoom on the correlation peak.

using the TOPCAT program, representing the FWHM as a function of σ (Figure 9).

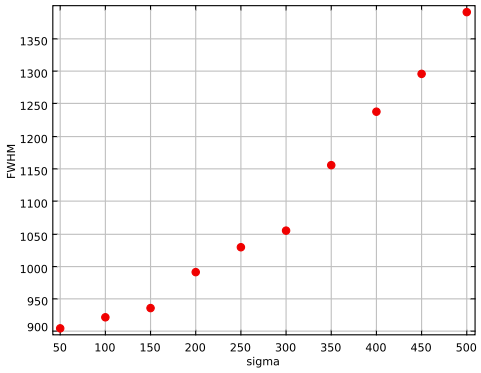

Fig. 9. Graph that relates the FWHM of the correlation peak and σ. The units are km s^{-1} in both axes.

Now, we divided the spectrum of the galaxy in regions of ~3.5″ starting from the center, and we cross correlated each of them with the spectrum of the star. Using the calibration graph found above (Figure 9), from each FWHM of the correlation peak we obtained the corresponding stellar velocity dispersion. Then we plotted the values of σ against the distance from the center.

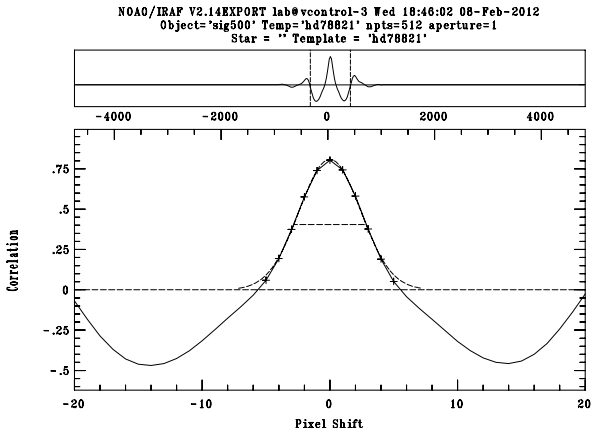

Fig. 10. The result of the correlation between the spectrum of one of the regions in which the galaxy was divided, and the spectrum of the star.

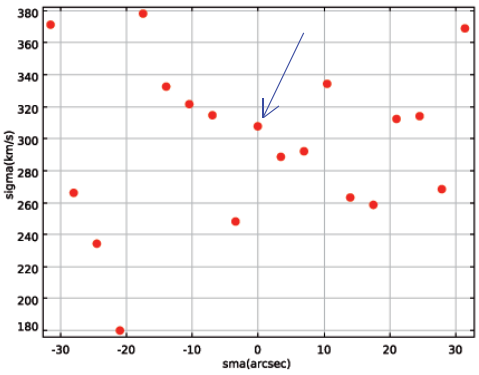

Fig. 11. Graph of the velocity dispersion as a function of the radius.

Since this is an elliptical galaxy, we expected a graph showing a trend of decreasing σ from the center of the galaxy outwards, such as in Figure 12.

In this case, we obtained a random distribution (Figure 11): we interpret this result considering that the values of σ are close to the spectral resolution (about 280 km s^{-1}) and so it is difficult to obtain the correct graph.

After converting the distances from the center from pixel to arcsec (Eq. 1):

$$R('') = R(px) \times scale \quad (1)$$

where the AFOSC pixel scale is 0.5″/px. We obtained also the rotation velocity in each region, and we plotted a graph velocity vs. radius.

The curve has the expected shape: the module of the velocity increases with the distance from the center.

To calculate the mass of the galaxy it is necessary to know the effective radius r_e, i.e. the radius that contains half the luminosity of the whole galaxy. For this

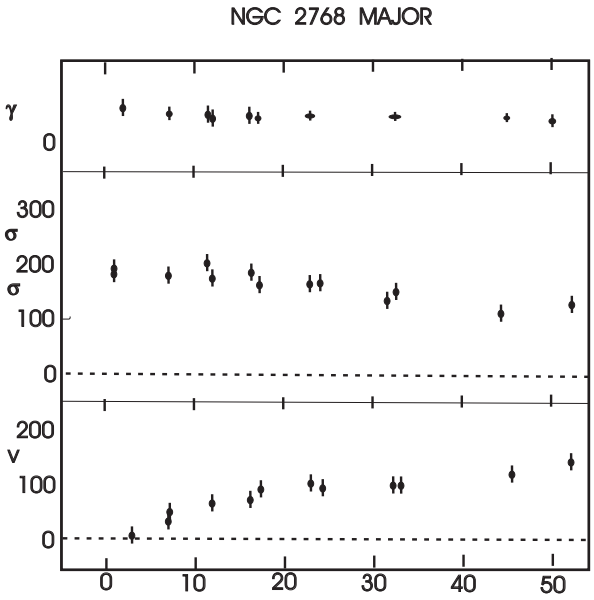

Fig. 12. Rotation curve and velocity dispersion as a function of the radius, from Fried & Illingworth, 1994

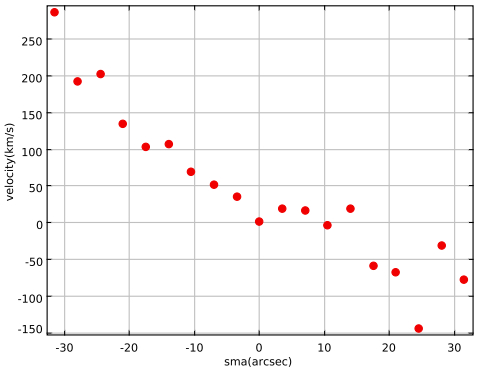

Fig. 13. The rotation curve of the galaxy.

purpose, we used the IRAF task ELLIPSE to model the isophotes of the galaxy, approximated by ellipses. The isophotes are lines connecting points of equal brightness. It is necessary to give ELLIPSE the starting values. To this aim, we enclosed the galaxy with an ellipse that approximates its shape, determining the coordinates of the center as accurately as possible.

With these initial values, the task extrapolates the geometrical parameters (Sma, e, Pa, etc) and the flow within each ellipse, and gets the average sma and the average intensity for each ellipse. The relative intensity for each individual ring is obtained by subtracting the flow of each ellipse n-th one of the ellipse (n-1)-th (fig. 11). These values are modified, however, taking

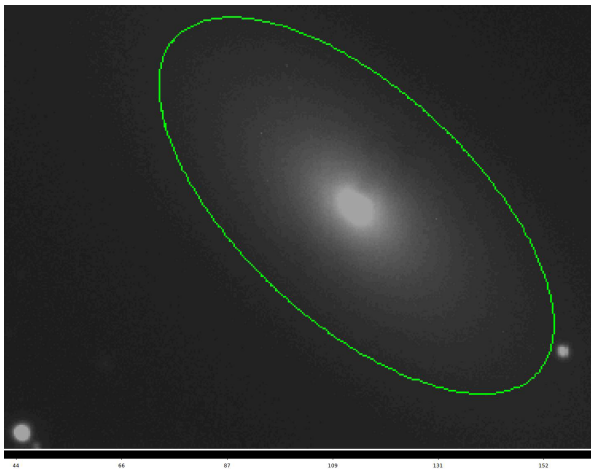

Fig. 14. Manual setting of the starting ellipse.

account of the average intensity of the sky and the exposure time, with the following formula:

$$I_{sup} = \frac{I_* - < I_{sky} > \times < N_{pix} >}{t_{exp} \times A} \quad (2)$$

Where I_* is the intensity calculated within the single ring, I_{sky} is the average intensity of the sky, N_{pix} is the number of pixels contained within each ring, t_{exp} the exposure time of the image and A the area of each pixel in arcseconds. To find the instrumental surface brightness we used the Pogson law:

$$\mu = -2.5 \log_{10}\left(I_{sup}\right) \quad (3)$$

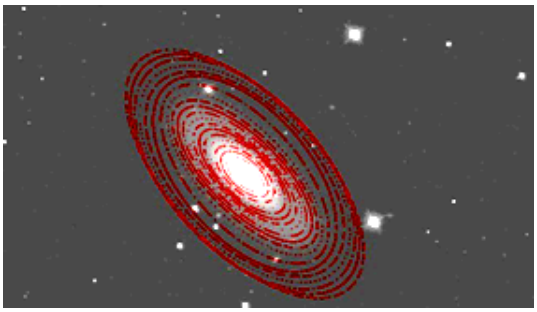

Fig. 15. Approximated galaxy isophotes, made by the using of ELLIPSE.

With the found values and through TOPCAT we are able to create the brightness profile of the galaxy, i.e. the trend of the instrumental magnitude as a function of the distance from the center (fig. 16).

3.1. Analysis of the brightness profile

Since the brightness profile of the galaxy depends on its effective radius and because our profile was deduced experimentally, we try, for comparison, the best fit made

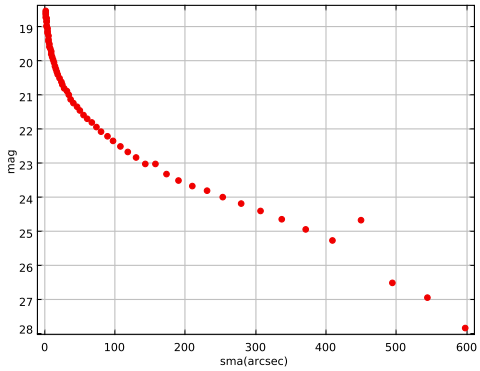

Fig. 16. Brightness profile: graph describing the trend of the instrumental magnitude as a function of the distance from the center.

with known empirical laws.
With De Vaucouleurs' empirical law (4), we put, each time, different values of effective radius (r_e) and the relative brightness (μ_e).

$$\mu_{bulge} = \mu_e + 8.325\left[\left(\frac{r}{r_e}\right)^{\frac{1}{4}} - 1\right] \quad (4)$$

This study, however, does not achieve a satisfactory fit, except for the area near the center of the galaxy (fig. 17).

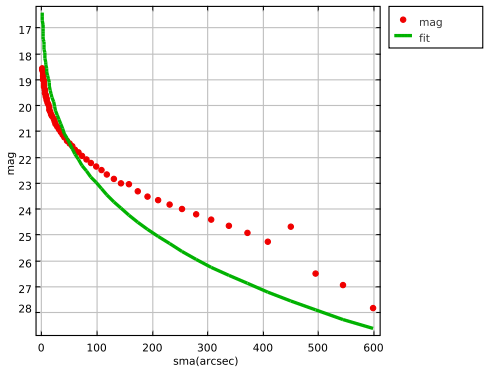

Fig. 17. Fit made using only De Vaucouleurs' law.

So we used two different empirical and exponential laws: one for bulge profile (5) and the other for the disk (6).

$$I_{bulge} = I_e \exp\left[-7.67\left[\left(\frac{r}{r_e}\right)^{\frac{1}{4}} - 1\right]\right] \quad (5)$$

$$I_{disk} = I_0 \exp\left[-\left(\frac{r}{h}\right)\right] \quad (6)$$

Using these two components we got a better experimental curve (fig.18).

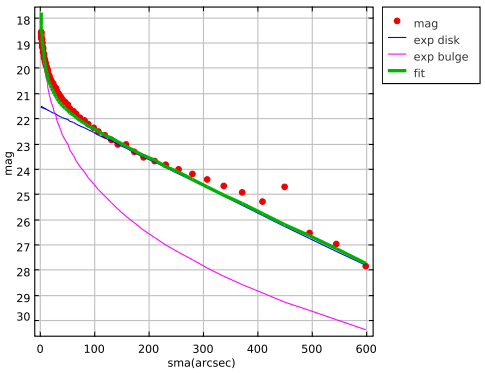

Fig. 18. Brightness profile fitted with two different exponential laws, one for the bulge and one for the disk.

The best fit we made was obtained for r_e = 46 arcsec = 1.23 $\times 10^7$ km.

3.2. Calculation of the mass

Since the effective radium is bigger than the maximum distance from the centre considered in this work (31.5″) and since we couldn't extract the σ from the experimental distribution, we used the σ of the central band (307 km/s, arrow in fig.11). So we determined the mass of the galaxy.

$$M = \frac{r_e \cdot \sigma^2}{0.33G} \tag{7}$$

We got: M=5.26×10^{41} kg, ie M=2.63 ×10^{11} $M_\odot$.

To have a comparison, we derived the mass of the galaxy also using the Virial Theorem, which links the kinetic energy and the potential one of a system at equilibrium, according to the known relationship: 2K+U = 0.

$$M = \frac{R \cdot v^2}{G} \tag{8}$$

where R (31.5″) is the greatest radius deducted from the rotation curve and v (200 km/s), the respective velocity (Figure 13). The mass turns out to be M=5.06×10^{40} kg, ie M=2.53 ×10^{10} $M_\odot$.

4. Results

From this analysis, some result, which discord with our expectations, emerged. The rotation curve (Figure 13) suggests that the galaxy rotates with a velocity higher than those normally seen in similar elliptical galaxies; against a normal average velocity of about 50 km s^{-1}, NGC2768 presents a rotational velocity, at the considered extremes, measuring nearly 200 km/s: this is the a typical behavior of barred or spiral galaxies.
Also the profile of brightness obtained is not really an elliptical galaxy, since it is not possible to find an optimal fit for all the curve using only De Vaucouleurs' empirical law (which usually well reproduces the brightness profile of elliptical galaxies).
In order to find a better fit of the experimental curve we used two other empirical and exponential laws, one for the bulge and one for the disk, as if, in the galaxy, the light did not come from a compact body but from a one composed of bulge and disk.
Anyway we find high values of σ in the nucleus of the galaxy, although, in our work, the trend of σ as a function of the distance from the center is not representative of the velocity dispersion in an elliptical galaxy.
We are thus led to believe that NGC2768 is a S0 galaxy. But it could also be the result of merging with another galaxy.

References

NED (Nasa/Ipac Extragalactic Database), http://ned.ipac.caltech.edu
SIMBAD (Set of Identifications, Measurements and Bibliography for Astronomical Data) Astronomical Database, http://simbad.u-strasbg.fr/simbad/
SDSS (Sloan Digital Sky Survey), http://skyserver.sdss.org/public/en/
http://www.oacn.inaf.it
www.fisica.uniroma2.it/~balbi/eleastro2/Lezione12.pdf
Fried J. W., Illingworth G. D., 1994, AJ, 107, 992
A.Pizzella, *Corso Astrofisica Generale* Mod. B, Dipartimento di Astronomia Universitá di Padova, a.a. 2008/09
S.Ciroi et al., *Massa di galassie ellittiche o sferoidali*
S.Ciroi et al., *Fotometria di galassie con* ELLIPSE
S.Ciroi et al., *Cinematica di una galassia a spirale*
The sky as a laboratory, University of Padua
T.Cavattoni, *Il cielo sopra di noi*

Il Cielo come Laboratorio, 49
A.S. 2011-2012

Morphological analysis of spiral galaxy NGC7331

Maurizio Boscolo[1], Matteo Legnardi[2], Jacopo Lion[3], Lorenzo Pasqualetto[3]

[1]Liceo Classico Giuseppe Veronese Chioggia (VE)
[2]Liceo Scientifico Pietro Paleocapa Rovigo
[3]Liceo Classico Marco Foscarini, Venezia

Abstract. We worked on the morphological classification of the galaxy NGC7331 through the photometric analysis of *B*- and *R*-band; by studying the isophotes modelled with ellipses, in particular the position angle, the ellipticity and the centre position, and by comparing the brightness profile to some empirical laws, it was possible to quantify the relative importance of the bulge and the disk. Therefore, we calculated the quantitative morphological classification. Then, we created the color map of the galaxy, and its radial color profile *B*-*R*.

1. Introduction

The best-known classification system of galaxies surely is the Edwin Hubble's one, which dates back to 1936. This system proposes a partition in 4 families of galaxies that are denominated from their morphology: elliptical, lenticular, spiral-like and irregular, as we can see in Figure 1, which represents the famous diapason diagram.

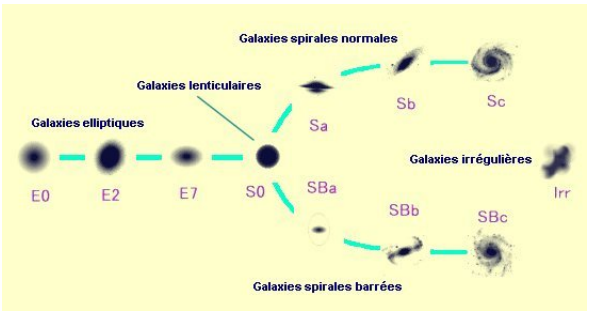

Fig. 1. Scheme that shows Hubble's morphological classification of galaxies.

This system has some limits: probably the most important of them is that it is only based on a qualitative and subjective observation of the images. A more objective and quantitative approach is based on the photometric analysis of these celestial bodies, by means of some helpful applications, mainly IRAF and DS9.

The photometric analysis of galaxies is built on the notion of isophote: it is a line that links all the points of an extended light source, like a galaxy, that have the same brightness.

The IRAF ELLIPSE task allowed us to interpolate the isophotes of the images in *B* and *R* band and to obtain, starting from a manually created elliptical model, the parameters that were necessary for the morphological analysis. These parameters were the semi-major axis (SMA), the position angle, the centre position and the ellipticity. The construction of the isophotes was made by following two different methods: by using both variable and fixed centres; a specific parameter of the ELLIPSE task allowed to set these two behaviours of the program. Then we focused on the connection between ellipticity, position angle and centre position depending on the SMA, regarding the isophotes with variable centers. Later on, by starting from the isophotes with fixed centres, we built the brightness profile that was compared to some empiric laws which describe the brightness trend of the specific parts of the galaxy, in particular the bulge and the disk. Thanks to this comparison, we were able to find the T-Type value that is fundamental for an objective morphological classification.

The last operation we made was based on IRAF BMODEL task. Then we obtained the color map *B*-*R* of the galaxy and the radial profile of the same color.

The galaxy we studied is called NGC7331; it was diskovered by William Hershel in 1784; it is placed in the Pegasus constellation, it is about 14 Mpc far from us and it is the brightest element of the group of galaxies that has the same name. Its coordinates are: RA=$22^h\ 37^m\ 04.1^s$, DEC=$34°\ 24'\ 56''$(J2000).

2. Observational Data

Our analysis started from 2 different images of the galaxy NGC7331 that were aligned and had an exposure time of 100 sec, but that were taken with

two different filters, respectively *B* and *R* of Bessel photometric system. The two images were acquired by the Schmidt-Cassegrain 67/92 telescope of Padova Astronomical Observatory (OAPd-INAF) placed on cima Ekar (Asiago, Italy), with the CCD SBIG STL 11000M 4000x2600 px, pixel scale 0.86″/px: Fig.2.

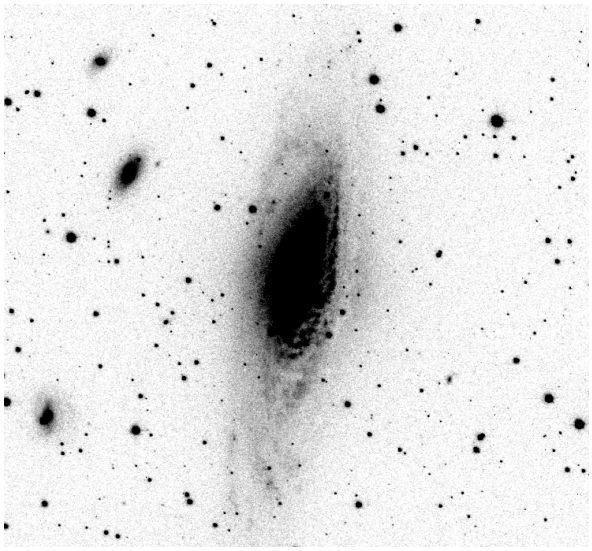

Fig. 2. An image of NGC7331 in *B*-band acquired by the Schmidt-Cassegrain 67/92 telescope of Padova Astronomical Observatory (OAPd-INAF) placed on cima Ekar (Asiago, Italy).

3. Work description

IRAF, the software used to analyze the images of NGC7331, includes a package which allows to build, thanks to the ELLIPSE task and starting from an image of the galaxy, the isophotes and to obtain from them all the useful parameters (SMA, centre position, position angle, ellipticity, light flux inside the isophote, pixel number). Therefore, it was possible to compare these values, in particular the variation of ellipticity, the centre position, the position angle depending on the SMA; these comparisons allow us to determine an approximate evaluation of the morphology of NGC7331.

Through another IRAF task, called BMODEL, it was possible to get a model image by interpolating the elliptical isophotes obtained with ELLIPSE; the result was an image that showed every element of NGC7331 that departed from the ellipticity: spiral arms, bars, internal structures.

In addition, we were able to obtain the brightness profile, that is a diagram that relates the surface brightness and the SMA, by using again the data of the ellipses produced with IRAF. The brightness profile obtained from the photometric analysis can be compared with empirical laws which describe the surface brightness trend of different components of the galaxy like the bulge and the disk. We fitted the empirical models to the observed data, by changing the appropriate parameters. The same parameters can be finally used to determine the T-Type value, a parameter introduced by Simien and DeVaucouleurs in order to make an objective morphological classification of the galaxies.

Another approach to the morphological study is based on the galaxy's color map and on the color profile. The work is based on the concept of color index, which represents the difference in magnitude of an object taken in two different photometric bands. With the images of the galaxy in two different photometric bands (e.g. B and R) it is possible, by applying the formula of the color index, to obtain the map and the galaxy's color profile which allow us to describe the distribution of the stellar population inside the galaxy.

In details, we proceeded as follows. We manually constructed a guess ellipse on the first image, that was opened with DS9, in order to mark the galaxy as shown in Figure 3. This ellipse, whose parameters (centre position, major axis dimension and position angle) were drawn with a specific DS9 tool, was used as an approximate evaluation for the construction of isophotes with ELLIPSE task.

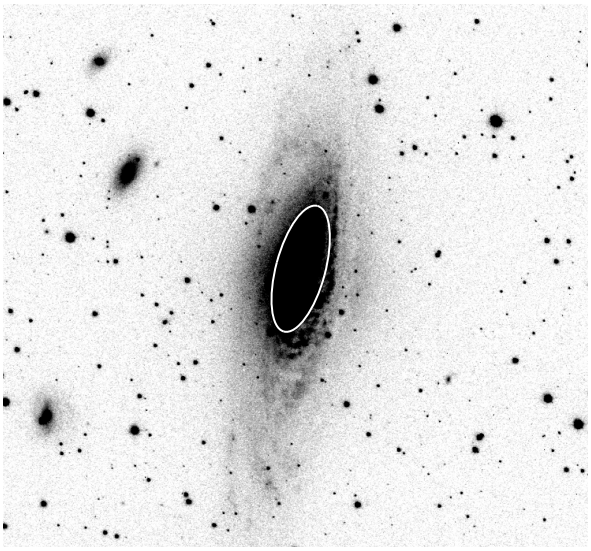

Fig. 3. Image of the galaxy in *R*-band with the ellipse we used to determine the input parameters for IRAF ELLIPSE task.

We also defined the *h*center parameter (set on *no*) to start to work with moving-centre ellipses. Then, we applied a mask on the stars which could disturb the construction of the ellipses. Later it was plotted in DS9 the whole series of isophotes by launching ELLIPSE task; the construction was interactive so that the program showed different values of stop code at every isophote elaborated: for values 0 and 2 the isophote were confirmed, for the value 4 (incorrect fit) the same isophote were

ignored. The cut-off of the extension of isophotes was given by the parameter *m*axsma, previously setted at 700 px (Figure 4).

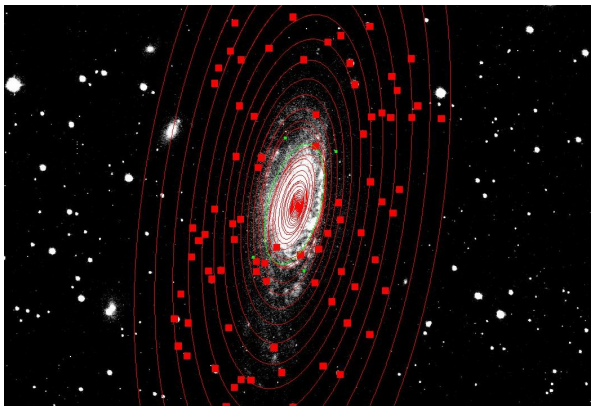

Fig. 4. Isophotes of the galaxy made with ELLIPSE and masks for the stars in *R*-band.

The output of the ELLIPSE task is a table containing the whole data of the drawn ellipses, from which only columns necessary for our work were extracted using *tdump* command: SMA, ellipticity, position angle (PA), centre's coordinates X0 and Y0, the flux and the number of pixels inside the ellipses. These data were saved in a new table, which we modified with a text processor (*gedit*). After these changes, the table was opened with TOPCAT and we could create two graphs: in both of them the X axis shows the SMA values, but in the first graph the y_1 axis refers to ellipticity and y_2 refers to PA, in the second y_1 refers to X0 and y_2 refers to Y0.

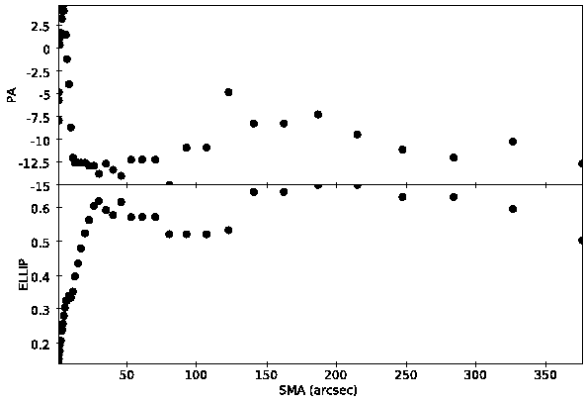

Fig. 5. Ellipticity (bottom) and PA (top) brought on line with SMA.

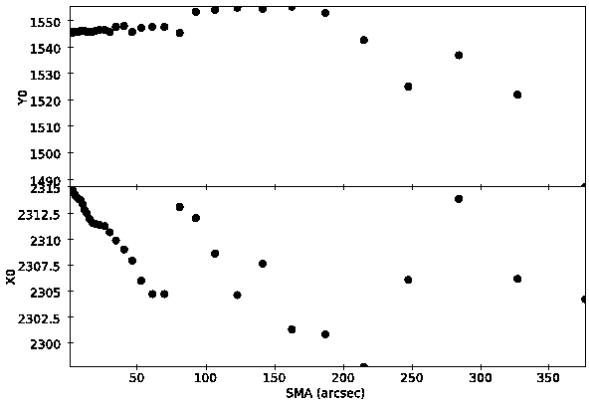

Fig. 6. X0 (bottom) and Y0 (top) in function of SMA.

With these graphs we could have a first idea of the morphological classification: it can be noted that the ellipticity of the galaxy grows rapidly up to 0.6 at SMA=30″, and then it remains almost constant; also the PA suddenly changes, decreasing in the innermost part of the galaxy and then it keeps constant. The centre of the ellipse does not change with the radius. These plots indicate that our galaxy is not an elliptical galaxy. Then, our work proceeded with the construction of an image of the galaxy as if the isophotes were exactly elliptical. To do that we need to know the mean sky value, measurable with the IRAF IMEXAMINE task: to obtain this is sufficient to analyze areas of the image empty of stars to diskover the mean and median value of the intensity of the pixels in those areas and the standard deviation. The mean sky value and the mean standard deviation were calculated. Thanks to BMODEL task we created an image obtained by interpolating the elliptical isophotes calculated by ELLIPSE which once subtracted from the original image with the IMARITH command returned the image of the residual.

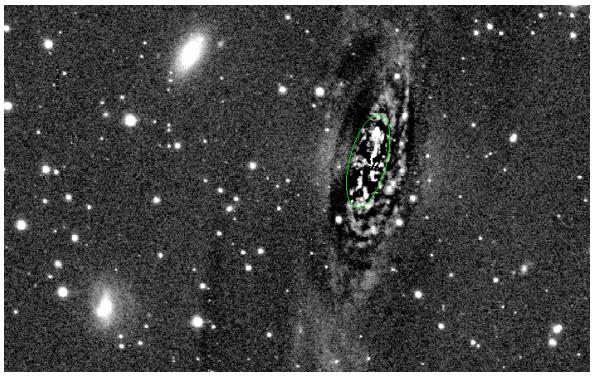

Fig. 7. Image of the residual for the galaxy in *R* filter.

In Fig. 7, we noticed spiral arms in the external part and star formation regions in the inner part. Then, we created the fixed centre ellipses, initially only for *R*

band, modifying the *hcenter* parameter and, setting it on "yes" this time, we obtained a new data set: SMA, flux and the number of pixel were put in another table. Now, we needed to find the flux value for each SMA. Therefore, we opened the table with TOPCAT and we added 3 columns to it: the SMA in arcsec, from the scale value=0.86 $\frac{\text{arcsec}}{\text{pixel}}$ ("a"), the sky-subtracted flux value ("flux") and the isophote area in arcsec squared ("area"), calculated with the formulas: 1, 2, 3.

$$a = sma \times scala \tag{1}$$

$$flux = \frac{t_{flux} - (n_{pix} \times I_{cielo})}{t_{exp}} \tag{2}$$

$$area = n_{pix} \times scala^2 \tag{3}$$

We used the data of this table in order to obtain the flux of each ring resulting from the difference between the area of two consecutive isophotes. In order to do it, we obtained two subsets from the newly created table: the first subset included lines from the first one to the last but one, the second subset included lines from the second one to the last one. Then we made the match between the two tables. Finally, we calculated the mean radius in arcsec and the surface brightness in counts s^{-1} $arcsec^{-2}$ with formulas (4, 5):

$$r = \frac{a_1 + a_2}{2} \tag{4}$$

$$int = \frac{flux_2 - flux_1}{area_2 - area_1} \tag{5}$$

The calculation made on the data of the fixed centre isophotes permitted us to calculate, for each ring, the surface brightness as a function of the radius in agreement with the equation (6):

$$I_{sup} = \frac{I_* - I_{sky} \times N_{pix}}{t_{exp} \times A} \tag{6}$$

where I_* is the brightness of the single ring, I_{sky} is the mean brightness of the sky, found previously, N_{pix} is the number of pixels of the single ring, A is the area in arcsec of a single pixel. Moreover we put in the table a new column with the following expression:

$$\mu = -2.5 \log_{10} I_{sup} \tag{7}$$

this expression allowed us to define the surface brightness in instrumental magnitudes in function of the distance from the centre (Surface Brightness), shown in Figure 8.

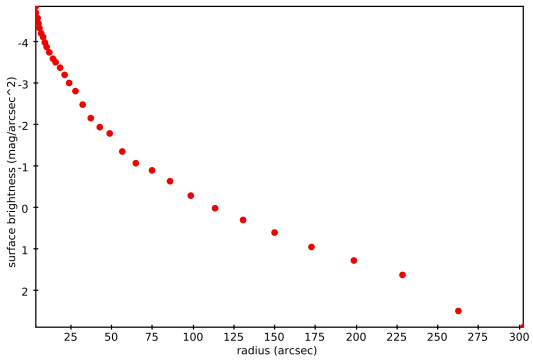

Fig. 8. Surface brightness of the galaxy obtained from the image with the *R*-filter. On the x-axis there is the radius; on the y-axis there is the surface brightness.

The obtained values of the instrumental magnitude, in function of the distance from the centre, can be compared with empirical laws which permitted us to calculate the brightness for the two components of the galaxy: the bulge and the disk. We used the De Vaucouleurs empirical law for the bulge (8) and the exponential disk empirical law for the disk (9):

$$I_{bulge} = I_e exp\left\{-7.67[(\frac{r}{r_e})^{\frac{1}{4}} - 1\right\} \tag{8}$$

$$I_{disk} = I_0 exp\left\{-(\frac{r}{h})\right\} \tag{9}$$

These empirical formulas have some parameters which permit to reproduce the surface brightness. These parameters are the effective radius (r_e), that is the distance from the centre in which there is half of the bulge's light and the intensity at the effective radius (I_e), for the first law; the scale height (h) and the central intensity (I_0), for the second law; for both the laws the radius is indicated by r. The search for the right parameters allowed us to model the observational data in the way in which it is represented in the graph of Figure 9. The values of the parameters are reported in the Table 1: both I_e and I_0 are not calibrated values, so they are expressed in counts/arcsec^2.

Parameter	Value
r_e	34
I_e	3
h	65
I_0	5

Table 1. Parameters for the empirical laws.

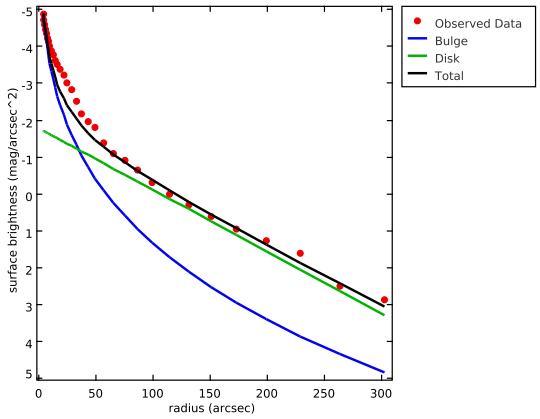

Fig. 9. Fit (black line) of the NGC7331 galaxy's surface brightness obtained using the De Vaucouleurs law (blue line) for the bulge and the disk exponential law (green line) for the disk.

These same parameters allowed us to calculate the total brightness of the two components. In particular, for the bulge:

$$I^{tot}_{bulge} = 22.66 \times I_e \times (r_e)^2 \quad (10)$$

Whereas for the disk:

$$I^{tot}_{disk} = 2\pi \times I_0 \times h^2 \quad (11)$$

In this way we found $I^{tot}_{bulge} = 78585$ and $I^{tot}_{disk} = 132732$. Moreover we calculated K_1,that is the ratio between the brightness of the bulge and the total brightness, which is $K_1 = B/T = 0.37$. A value derives from it, that is $\Delta m_1 = -2.5 \log K_1 = 1.07$, which we put in a particular diagram which is related to a number called T-TYPE. Thanks to a special scale, this number is associated with a determined morphological classification: our group found a T-TYPE value=1.5, which corresponds to a spiral galaxy Sa or Sb.

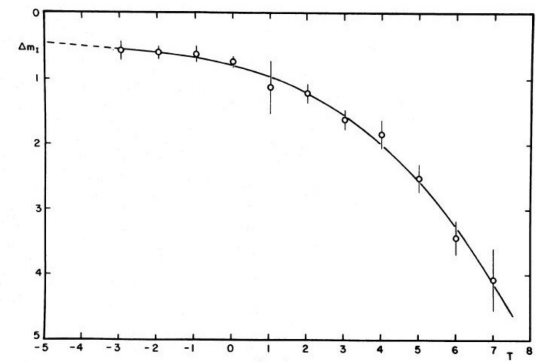

Fig. 10. Diagram for the determination of the relation between Δm_1 and T-Type.

T-Type	Morphological type according to Hubble
-6	E
-5	E
-4	E
-3	S0
-2	S0
-1	S0
0	S0/a
1	Sa
2	Sa-b
3	Sb
4	Sb-c
5	Sc
6	Sc
7	Sc
8	Sc-Irr
9	Irr I
10	Irr I

Table 2. Relation between T-Type value and morphological typology of the galaxies according to Hubble.

We later proceeded to study the color map. The color index is a difference between two magnitudes:

$$B\text{-}R = 2.5 \log I_B/I_R \quad (12)$$

In order to obtain the color map we calculated this difference by using IRAF IMARITH task that allowed us to calculate the ratio of the brightness intensity of an image (filter *R*) to another (filter *B*), pixel by pixel. Before we could make this operation, the two images had to be aligned and to have the same exposure time: however, the original images already fullfilled these two conditions. Moreover, we had to subtract the background sky counts, that were obtained by making the average of the counts in different points of the image far enough from light sources, by means of IRAF IMEXAMINE task; so we got the mean, that was 141 in the *B* band image and 341 in the *R* band one. Because of the greater extension of the *R* band image, in *B* band one we put every pixel of value $< 3 \times \text{stddev}_{cielo}$ equal to zero. The standard deviation (9.6 for the *B*-band image, 11.6 for the *R* band image) was found with the same method we used for the mean, and then it was used to change the values of the pixels with the IMREPLACE task. So we obtained an image with values different from zero concentrated only in areas corresponding to the galaxy and the stars, and that image was ready to be used to divide the images in the different bands (by using the IMARITH task). We calculated the $\log_{10}$ of that image by using the IMFUNCTION command and by applying the logarithm to the function parameter, and then we multiplied it by 2.5 with IMARITH. The resulting image is represented in Figure 11. The color distribution of the components of the galaxy is evident. The bulge appears mostly red, because of the old stars, while in the outskirts the blue color prevails, caused by hot young stars. This distribution is typical of spiral galaxies. Then we obtained, by using the ELLIPSE task again, the *B*-*R* color radial profile.

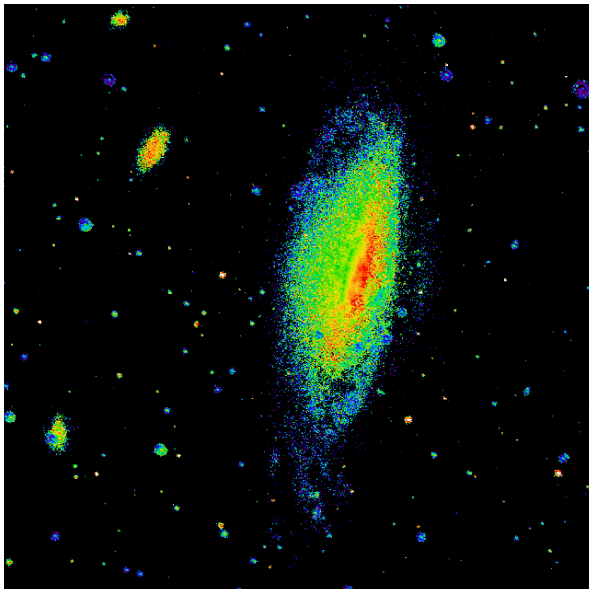

Fig. 11. *B*-*R* color map of NGC7331.

This time the ellipses were drawn on the *B*-image by applying those obtained for the *R*-band image: in other words, we used the ellipses calculated in the *R*-filter to analyze the galaxy in *B*-band, by calculating only the flux within these ellipses; obviously the ELLIPSE task will not give us 0 or 2 stop codes, but 4, nevertheless the ellipses will be considered correct. The obtained data were modified to get the brightness profile of the image in B and then, from the two brightness profiles we obtained the color profile by subtracting the magnitude in *R*-band from the magnitude in *B*-band.

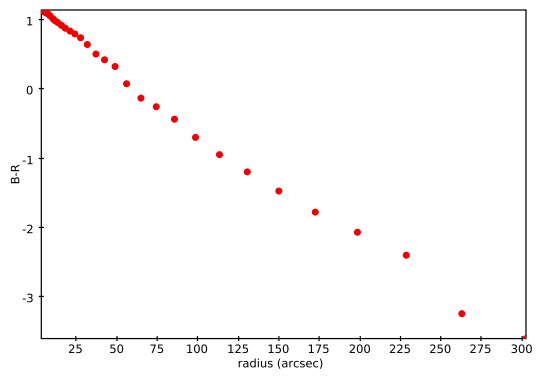

Fig. 12. *B*-*R* color index in relation to SMA for NGC7331; there is a predominance of the red color in the central zone of the galaxy and of the blue color in the outskirts.

4. Results

The morphological analysis of NGC7331 was carried out by means of images in *B*- and *R*-band taken by the Schmidt-Cassegrain 67/92 telescope (OAPd-INAF), and using DS9 and IRAF programs, particularly ELLIPSE and BMODEL tasks. Those tasks allowed us to get the main parameters of the isophotes of the galaxy like SMA, PA, light flux, center position and ellipticity. From these data we could do a first guess of the morphological class of the galaxy according to the values of ellipticity, PA and center position in function of SMA and according to the analysis of the residual image. In a second phase we plotted the brightness profile thanks to the values of the light flux within the isophotes. With that profile we created a model of the galaxy by using the empirical formulas of De Vaucouleurs (bulge) and of the exponential disk (disk), which allowed us to determine the T-Type and the morphological category of NGC7331. With the data of the light fluxes of the isophotes on the *B*- and *R*-images we built the color map of the galaxy and the radial color profile. NGC7331 is a spiral galaxy: it is demonstrated by the variations of PA, ellipticity and center positions of the isophotes as a function of SMA; the presence of a bar is also excluded because that feature is associated to increasing ellipticity and constant PA. The analysis of the residual image also clearly shows traces of spiral arms. The method based on T-Type that was proposed by F. Simien G. De Vaucouleurs (1986) leads to a morphological Hubble classification of intermediate type spiral between Sa and Sb (E.M. Corsini 2011). These categories concern spiral galaxies (S stands for Spiral) and the Sa and Sb subtypes refer to the prominence of the bulge, to the winding and to the resolution of the arms (E.M. Corsini 2011). The color map, also confirmed by the radial color profile, represents a galaxy in which the red color prevails in the bulge, typical color of cold old stars, while in the outskirts the blue color is dominant and typical of hot young stars; that confirms the galaxy is a spiral. A validation of this result can be found in A. Sandage e J. Bedke (1988)'s text, where NGC7331 is located in the same morphological classification as ours.

References

A. Sandage, J. Bedke,"Atlas of Galaxies", NASA, Washington DC, 1988

F. Simien, G. De Vaucouleurs, Sistematics of Bulge-To-Disk ratios, NASA, Washington DC, 1986

E.M. Corsini, Morfologia e classificazione delle galassie, Università di Padova 2011

S. Ciroi, Dispense per lo stage "Il cielo come laboratorio", Università di Padova, 2012

Il Cielo come Laboratorio, 55
A.S. 2011-2012

Stellar kinematics in NGC 7331: velocity dispersion and bulge mass

Daniele Cini, Marco Coppola, Caterina Derossi, Elena Lappon

Liceo Scientifico Statale *G.B. Benedetti*, Venezia

Abstract. We studied the spiral galaxy NGC 7331 considering its kinematic aspects, especially the velocity dispersion of its stellar component. To do this, we used the method of the cross-correlation between the spectrum of a sample star and that of the galaxy; the correlation gave a function whose peak can be fitted with a gaussian curve. The analysis of the velocity dispersion allowed us to estimate the bulge mass.

1. Introduction

The object we studied is a spiral galaxy, NGC7331, which was discovered in 1784 by W. Herschel, who included it in the New General Catalogue, one of the largest comprehensive catalogues, as it includes all types of deep space objects. NGC7331 is the brightest member of the homonymous group of galaxies and its structure is similar to the Galaxy with a spiral shape. Its morphological class is, indeed, Sb/a (Wikipedia 2012) (see Figure 1).

Fig. 1. Image of NGC 7331 taken with the Paramount Telescope.

In 1936, Hubble proposed a classification of galaxies based on their morphology, which is linked to many other properties of the objects. He divided galaxies in four main groups: elliptical, lenticular, spiral and irregular. Spiral galaxies are composed by a central spheroid called bulge, which is the object we will study, a disc characterized by spiral arms and a galactic halo, a spherical region which contains the whole disc. They contain from 10^9 to 10^{11} stars and are 3×10^3 to 10^5 pc in diameter. The arms are sites of strong star formation and mainly contain young stars rich of heavy elements, called population I stars. On the contrary, in the bulge and in the galactic halo, we find population II stars, old and poor of heavy elements (Cavattoni 2009).
The most common spectral types of stars in a galactic bulge are G, K and M: to make an accurate analysis we should examine all the three spectral types but, in our case, for practical reasons we only used the spectrum of a K5 star.
In elliptical galaxies and in bulges of spiral ones, stars move in a chaotic motion around the center of mass; kinematic information are provided by the width of the spectral lines, which allow us to calculate the stellar velocity dispersion (σ) as a function of the distance from the center. Indeed, in different positions of their chaotic orbits around the center, stars have spectral lines centered at similar but different wavelengths, higher if the star is receding, lower if it is approaching (see Figure 2). Due to the enormous number of stars in the bulge, the observed spectral lines are wider than those of a single star. Therefore the width of an observed line depends on the variation from the average velocity of the stars.
Furthermore, a more massive galaxy has a higher gravitational potential which results in a more chaotic motion of the stars and therefore in a higher velocity dispersion; we can then infer that the velocity dispersion is related to the mass, as well.
The distribution of the component of stellar velocity along the line of sight is described by a gaussian function, which can be characterized by two different kinds of width (see Figure 3): the FWHM (Full Width at Half

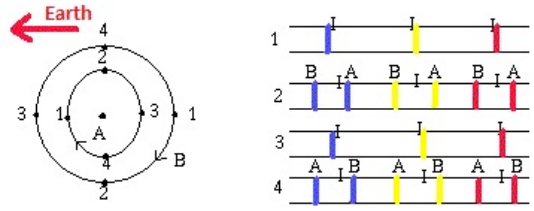

Fig. 2. Change of the wavelength at which the single star lines are peaked, according to their position around the center.

Maximum) and the sigma (σ), which are related by Eq. 1:

$$\mathrm{FWHM} = 2.35 \times \sigma \quad (1)$$

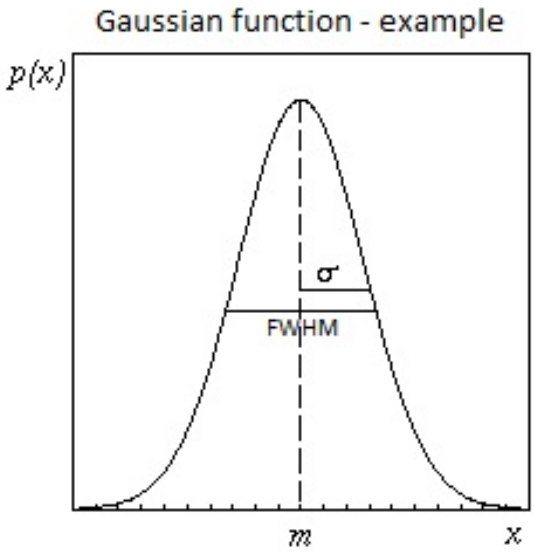

Fig. 3. Typical gaussian function in which are indicated the FWHM and sigma (σ) of the curve.

Therefore, a higher velocity distribution means a larger observed spectral line and, hence, a higher value of the FWHM or σ of the gaussian function interpolating the data.
It is necessary to pay attention because the gaussian functions considered are two: the first one defines the velocity dispersion within the bulge of the galaxy, the second one describes the correlation peak of the correlation function. The two curves have different FWHM, but there is a relation between the FWHM of the correlation peak and the sigma of the gaussian function used to convolve the stellar spectrum which represents the velocity dispersion. Therefore it is possible to compute the velocity dispersion (σ) knowing the FWHM of the correlation peak.
In the disc of a spiral galaxy, we expect to find high radial velocities and a low velocity dispersion, while in the bulge of spirals and in elliptical galaxies, we expect a lower radial velocity and a higher dispersion.

2. Observational Data

The spiral galaxy NGC 7331 can be observed in the Pegasus constellation, near to η Pegasi;its coordinates (J2000) are:
RA = $22^h\ 37^m\ 04^h$
DEC= +34° 24′59″
It is 12.2 Mpc far from the Milky Way and it has a receding velocity of 816 kmh^{-1}; its apparent magnitude is +10.4, and the major axis is 40 kpc long (Wikipedia 2012).
For our work, we used spectra taken on October, 30th 2012 at the 120 cm Galileo telescope of the Asiago Astrophysical Observatory with an exposing time of 2400 s. The spectrograph was a Boller&Chivens with a 4.3″ slit, set along the major axis of the galaxy, with a PA of -10° (**?**). The scale of the spectrum is 1 pixel = 1 arcsecond.

3. Work description

At first, we analysed the spectrum (see Figure 4) and divided it in regions. Since the spectrum of NGC 7331

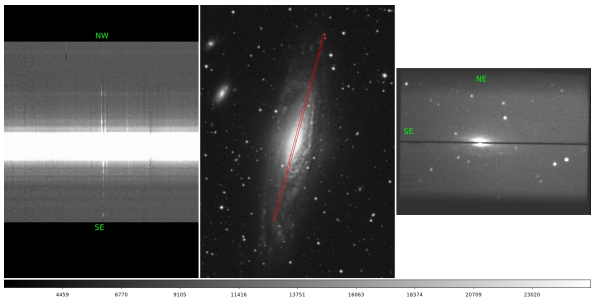

Fig. 4. Left: portion of galactic spectrum containing Hα and [N II] lines. On the y axis there is the position along the slit and on the x axis the wavelength. Center: position of the slit set along the major axis of the galaxy. Right: image of the guide camera of the telescope with the slit overlapped to the galaxy.

we considered has in abscissa the wavelength and in ordinate the spatial position, we selected 3″ wide regions starting from the center. It is important to point out that the possibility of moving away from the center is limited by too faint data. At the end, we obtained 29 regions (see Figure 5, reaching distances of +45″ and -36″ from the center. To do this, we used the BLKAVG task of the IRAF program.

We used the cross-correlation method to compute the velocity dispersion. This method requires to correlate the spectrum of the galaxy with that of the stars composing it convolved with a gaussian function, and

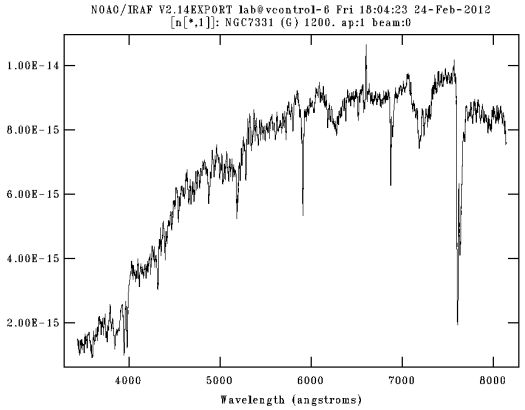

Fig. 5. Spectrum of the central region of NGC 7331.

puts in relation the FWHM of the peak of the correlation function and the sigma of the gaussian used to convolve the stars. For simplicity, we considered the galaxy composed only by cold K5 stars. In this way, the galactic spectrum can be seen as the convolution of the K5 star (see Figure 6) with a gaussian function of initially unknown σ:

$$G = S \otimes f(x) \quad (2)$$

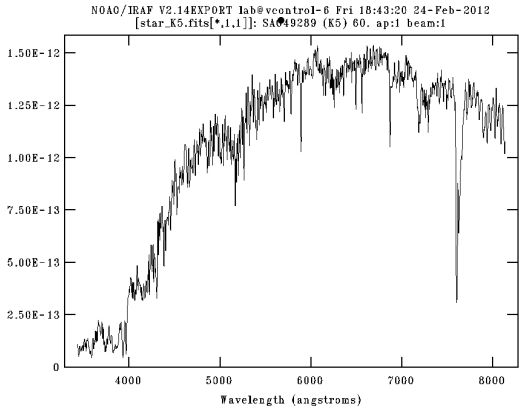

Fig. 6. Spectrum of a K5 star considered as representative of the whole stellar population of the galaxy.

In order to compute the velocity dispersion of the galaxy, we needed to know the relation between the FWHM of the correlation peak and the sigma of the gaussian used for the convolution, which is unknown. This relation can be found by cross-correlating the stellar spectrum convolved with gaussian functions of different known sigma and the stellar spectrum not convolved itself.

For this reason, at first we convolved the K5 spectrum with gaussian functions of increasing sigma, starting from 50 to 400 by step of 50 kms^{-1}, and we cross-correlated each one of the convolved spectra with the K5 spectrum not convolved, using the FXCOR task. In order to get a good correlation, it was necessary to fit both the convolved spectrum and the template spectrum continuum with a polynomial function of order 15 or 16 (see Figure 7) and to reduce the range of the spectrum taken into account, selecting the wavelength between 5600 and 6400 Å(see Figure 8).

Finally, the correlation function showed a peak that we

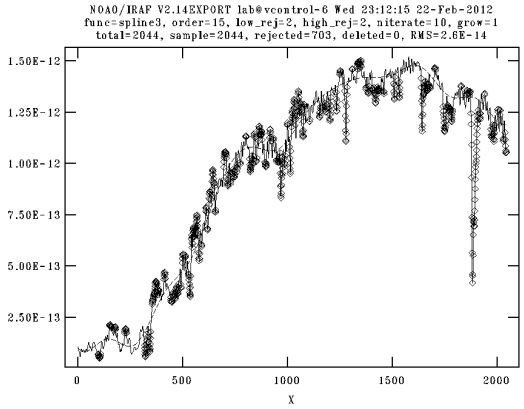

Fig. 7. Polynomial function of order 15 interpolating the spectrum of the K5 star.

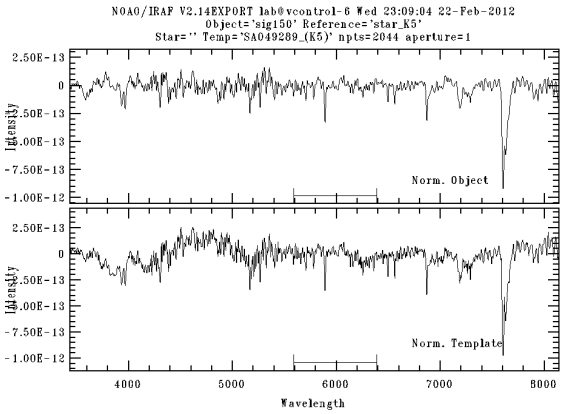

Fig. 8. Comparison between the σ = 150kms^{-1} convolved stellar spectrum and the K5 sample spectrum. It is shown the range of wavelengths selected for the correlation.

fitted with a gaussian function to find its FWHM (see Figure 9).

At this point, we had a list of FWHM of the correlation peak related to the σ used to convolve the stellar spectrum, and we were then able to build the FWHM-σ graph (see Figure 10). We computed the polynomial

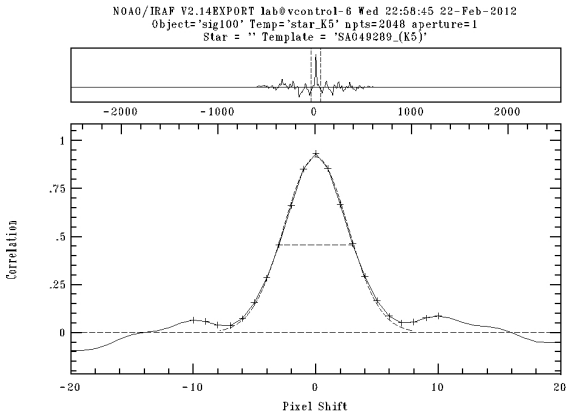

Fig. 9. Top: correlation function between the stellar spectrum convolved with a gaussian function of 100kms^{-1} and the template spectrum. Bottom: correlation peak fitted with a gaussian function.

function interpolating the data (Eq. 10) using the program EXCEL.

$$\sigma = 0.00045\,(\mathrm{FWHM})^2 + 1.4872\,(\mathrm{FWHM}) - 794.47 \quad (3)$$

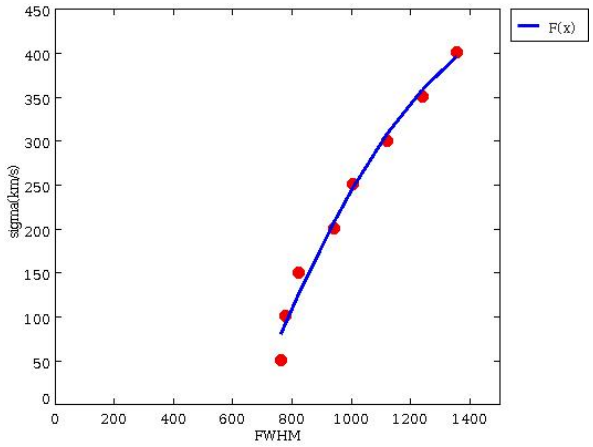

Fig. 10. FWHM-σ graph: the polynomial function is represented by the blue line.

Once obtained this relation, we were able to proceed with the cross-correlation between the galaxy and the star. With the same method previously used, we took the spectra of each region of the galaxy and we cross-correlated them with the K5 star not convolved spectrum. As before, we obtained a correlation function with a peak that had to be fitted with a gaussian function to obtain its FWHM. Then, using Eq. 3, we transformed the values of FWHM into values of velocity dispersion (σ).
Having the values of the dispersion velocity for the various regions, we were able to study the variations with the distance from the center. In order to do this, we built the a graph with on the y axis the velocity dispersion and on the x axis the distance from the center (see Figure 11). From the graph we can infer that the velocity dispersion remains constant as the distance from the radius increases.

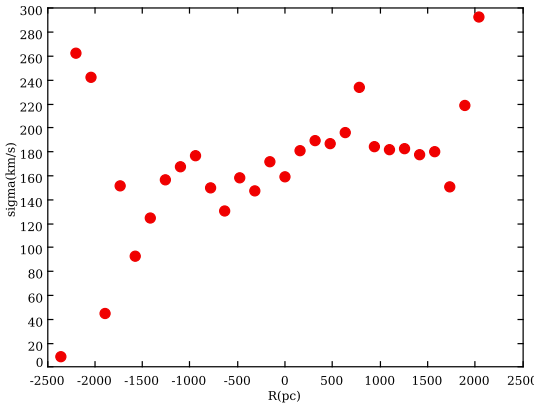

Fig. 11. Graph showing the relation between the distance from the center, on the x axis, and the velocity dispersion, on the y axis.

At this point, we could compute the mass of the bulge through the Virial Theorem (Eq. 4).

$$2K + \Omega = 0 \quad (4)$$

Were we can substitute K and Ω, according to Monaco (2010), with Eq. 5 and 6:

$$K = \frac{M(r_e) \times [\sigma(r_e)]^2}{2} \quad (5)$$

$$\Omega = -\frac{G \times [M(r_e)]^2}{r_e} \quad (6)$$

We, then, obtain Eq. 7 to compute the mass.

$$M = \frac{r_e \sigma^2}{0.33G} \quad (7)$$

Generally, it is necessary to put in Eq.7 the sigma corresponding to the effective radius, that is the radius containing half the luminosity of the galaxy, but in our case, since the relation between sigma and distance was constant, we could use the average value of σ. Moreover, we had to transform the effective radius from 34 ″into kilometers using Eq. 8.

$$r(\mathrm{pc}) = \frac{r('') \times D(\mathrm{kpc})}{206265} \quad (8)$$

Finally, through Hubble's law (Eq. 9), using the receding velocity of the center of the galaxy obtained with the cross-correlation method, and setting H_0 to 75 $kms^{-1}Mpc^{-1}$, it was possible to compute the distance of NGC 7331 from us.

$$d = H_0 \times v \tag{9}$$

4. Results

Through the mathematical method of cross-correlation, the study of the spectrum of NGC7331 allowed us to compute its distance from Earth (10.8 Mpc), the velocity dispersion related to the distance from the center (σ = 168 on average), the mass within the effective radius (9×10^{40} kg). Also, we considered the relation between velocity dispersion and distance from the center: in our case, the curve was virtually flat, showing that sigma has a constant value (Figure 11).
All the results we obtained were compared with values obtained by Bottema (1999) and available at on-line databases SIMBAD (2012) and Wikipedia (2012).
Furthermore the results obtained about the radial velocity curve were compared with those obtained by Angeli, Doda & Villani (2012), who studied the kinematics of the gas in the same galaxy. What we observe is that the velocities related to the radius are nearly equal in both studies (see Figure 12), which means that stars and gas move similarly. It is also noticeable that the gas can be studied at bigger distances that the stars. This is due to the fact that brightness of the spectral lines is higher for the gas than for the stars.

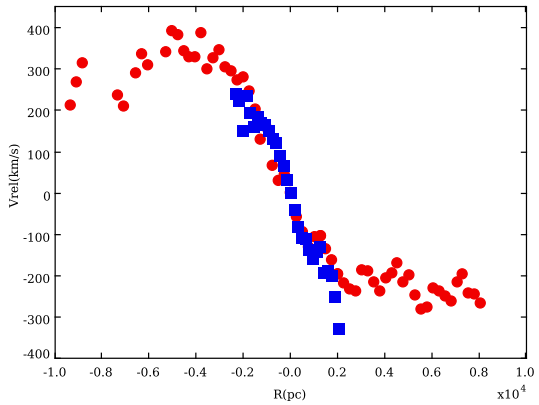

Fig. 12. Velocity curve of NGC 7331. On abscissa the distance from the center, measured in pc, and on ordinate the radial velocity, measured in kms^{-1}. Red points represent the gas velocity, whereas blue points represent the stellar kinematics.

References

Angeli, L., Doda, M., Villani, U., Gas kinematics in NGC 7331, The Sky As a Laboratory, 2012
Bottema, R., The kinematics of the bulge and the disk of NGC 7331, 2012, A&A, 348, 77B
Cavattoni, T., Il cielo sopra di noi, 2009, chapter 9
Monaco, P., Introduction to Astrophysics course booklet, 2011, http://adlibitum.oats.inaf.it/monaco/
SIMBAD Astronomical Database, 2012, http://simbad.u-strasbg.fr/simbad/
Wikipedia, 2012, http://www.wikipedia.it

Il Cielo come Laboratorio, 61
A.S. 2011-2012

Gas Kinematics in NGC 7331

Lorenzo Angeli, Mirdit Doda, Umberto Villani

Liceo Scientifico Statale *G.B. Benedetti*, Venezia

Abstract. In this work galaxy NGC 7331 was studied. The aims were reconstructing the rotation curve of the galactic gas and, then, calculating its mass by means of the Virial theorem. To do so, the wavelength of the Hα line taken at different distances from the centre was measured. We found that the gas component, near the galactic centre, rotates as a rigid body. Going further from the centre, the rotation curve does not behave according to the typical keplerian profile, as we expected, but it shows a flat profile. We can infer, therefore, the presence of dark matter.

1. Introduction

Throughout this work we will analyse the kinematic properties of a spiral galaxy: this kind of galaxy is characterised by the presence of a bulge in the centre and by a disc in which the great presence of gas enhances the possibilities of star formation.
We studied the galaxy NGC 7331, shown in Figure 1, which is part of a group of three galaxies, named after NGC 7331 itself, because it is the brightest (Materne et al. 1974).

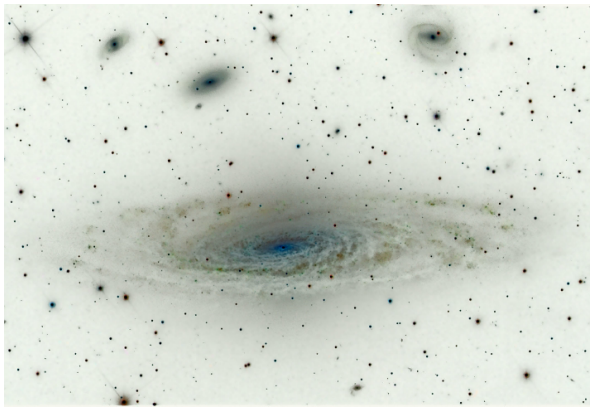

Fig. 1. The NGC 7331 group of galaxies.

We analysed two emission lines: Hα and [N II]. More specifically, the shift of H$\alpha$was analysed, and when this line was not visible, we studied the [N II] line. We measured the position of the emission lines, at different distances from the centre, in order to obtain the gas velocity by using the Doppler effect.
Due to the distance of the galaxy from Earth, lines are redshifted. Furthermore, because of the galactic rotation and as a result of the inclination that affects our observations of the galaxy, different redshifts are registered. Cini, Coppola, Derossi & Lappon (2012) analysed the stellar component of the same galaxy, allowing a comparison between the two components.

2. Observational Data

NGC 7331 is a galaxy that appears to be in the Pegasus constellation, whose coordinates (J2000) are:
RA = $22^h\ 37^m\ 04^h$
DEC= $+34°\ 24'59''$
Its distance from Earth is approximately 12 Mpc.
For this work, we used a spectrum (see Figure 2) obtained with the Galileo telescope at the Asiago Astrophysical Observatory. The telescope has a Cassegrain configuration and a 120 cm diameter. In order to obtain the galactic spectrum the Boller & Chivens spectrograph with a grating of 300 gr/mm was used. The grating has a 250 μm wide rift, which results in an angle of 4.3″. The range of wavelength goes from 3500 to 8100Å. The spectrum was acquired on October, 30th 2011, with an exposure time of 1200s.
We also used an image of the galaxy taken from the archive ESO-DSS I/II and obtained through the software DS9.

3. Work description

The first part of the work mainly consisted in using IRAF and some of its tasks. First, we zoomed the spectrum around the Hαline through the task SPLOT (see Figure 3).

Performing a gaussian fit, we were able to accurately measure the Hα wavelength at the distance from centre taken into analysis. The gaussian fit technique creates a gaussian curve that best approximates the data,

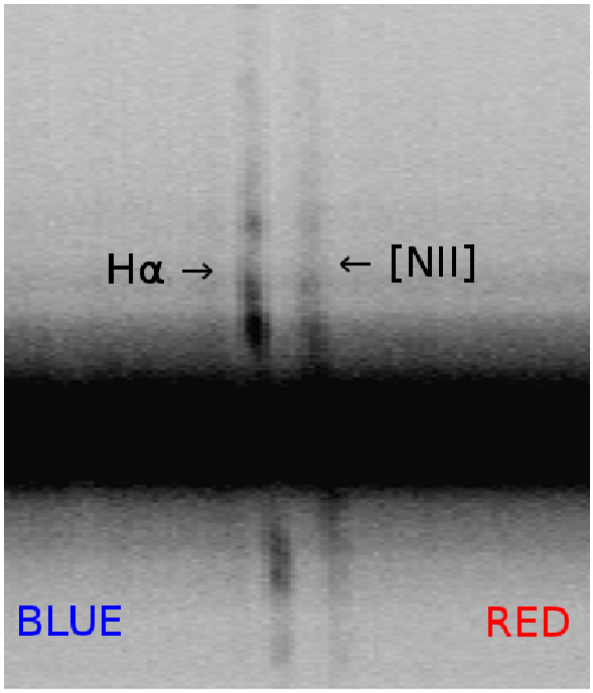

Fig. 2. The Hα and [N II] emission lines taken into account for the analysis.

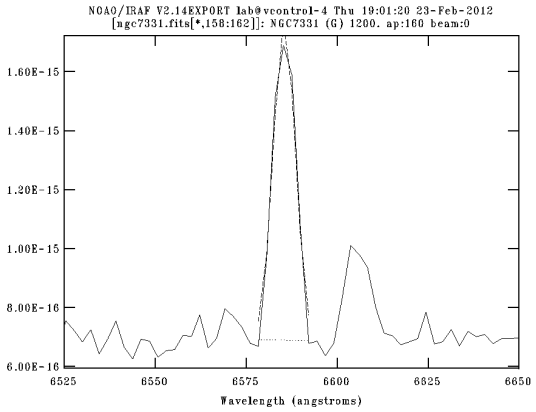

Fig. 3. IRAF window during the analysis with SPLOT.

using interpolation. If the Hα line was not visible, the [N II] line was studied. A text file was compiled in order to have two columns: the first one with the position along the slit and the second one with the measured wavelength.

The next step was obtaining the measures of the gas velocity at different distances from the centre, and of the distances as well.

Using the software TOPCAT recession velocities of the Hα and [N II] lines were computed using Eq. 1.

$$v_{recessional} = c \times z = c \times \frac{\lambda_{oss} - \lambda_0}{\lambda_0} \quad (1)$$

The obtained recessional velocity is 780.25 km s^{-1}.

At this point we could calculate the distance in Mpc between the galaxy and Earth using Hubble's law (Eq. 2), and then estimate the distance of every point of the galaxy from the centre of it, setting H_0 = 75 km s^{-1}Mpc^{-1}.

$$d = \frac{v_{recessional}}{H_0} \quad (2)$$

Our calculation gave us a distance from Earth of 10.4 Mpc.

We calculated the distances in parsec between the various regions and the centre of the galaxy, using Eq. 3 and knowing that the scale is that 1 pixel equals to 1 arcsecond.

$$r(pc) = r('')\frac{d(pc)}{206265''} \quad (3)$$

We could analyse the gas only within a range of 9 kpc from the centre.

In order to draw the rotation curve, we first computed the difference between measured wavelengths and at-rest ones, which are 6562.8 Å (Hα) and 6584 Å ([N II]). Then, we computed the observed velocities with Eq. 4. Doing so, we were able to create the graph (see Figure 4) placing on the x axis the different values of distance from the centre and on the y axis the different velocities obtained.

$$v_{obs}(r) = c \cdot \frac{\lambda_{oss} - \lambda_0}{\lambda_0} - v_{recessional} \quad (4)$$

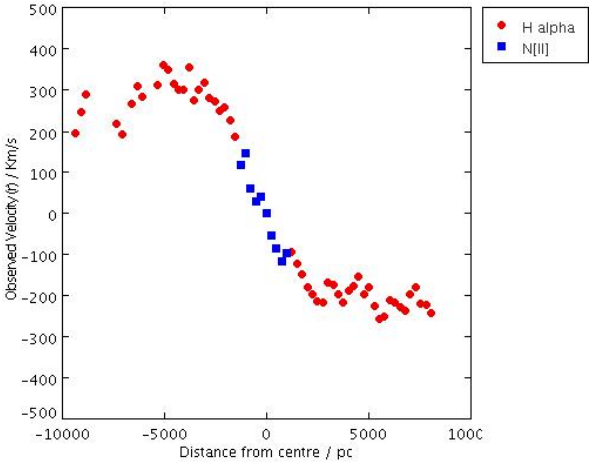

Fig. 4. The rotation curve graph with observed velocity.

The so computed velocity is only the component along the line of sight of the rotation velocity. Therefore, it had to be deprojected, taking into account the inclination of the disc of the galaxy with respect to the line of sight.

In order to do this, we recovered an image of the galaxy through the software DS9 and we tried to reproduce the shape of the galaxy with an ellipse that best fitted

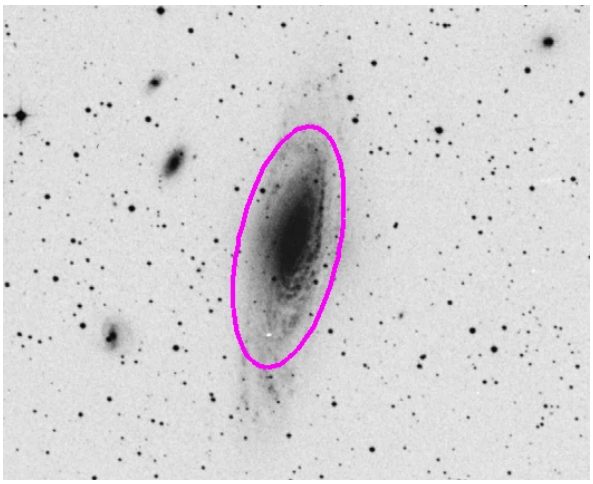

Fig. 5. NGC 7331 with overlapped the ellipse that best fitted the entire light.

the light of our object (see Figure 5). The values of the semi major axis and semi minor axis of the ellipse were edited by the software and were used to compute the inclination of the galaxy using Eq. 5.

$$i = \arccos\left(\frac{b}{a}\right) \tag{5}$$

At this point, we were able to deproject the velocity of NGC 7331 using Eq. 6.

$$v_{dep} = \frac{v_{obs}}{\sin i} \tag{6}$$

Deprojected velocities were then used to build the rotation curve reported in Figure 6. As it can be seen, these velocities are in the order of hundreds of km s^{-1}.

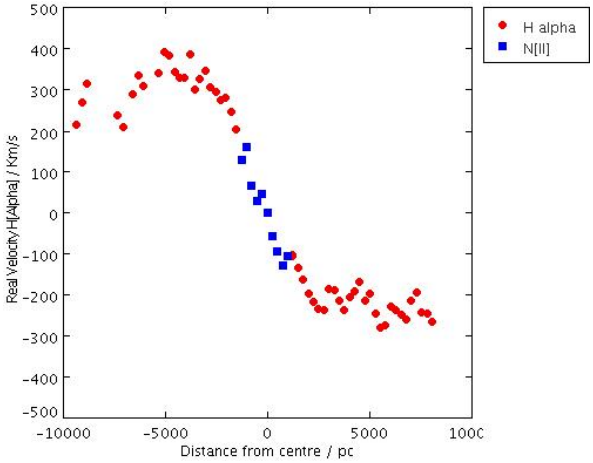

Fig. 6. The updated rotation curve with the deprojected velocity.

At this point we were able to model our rotation curve by fitting the deprojected velocities using Eq. 7 (see Figure 7).

$$v_c(r) = \frac{a \cdot r}{(r^2 + c_0^2)^{p/2}} \tag{7}$$

We had to assign values to the parameters a, c_0 and p by successive approximations, so as to best fit the data. We found that the value of a is correlated to the amplitude of the rotation curve, c_0 is in the order of thousands and p is between 1/2 and 3/2.

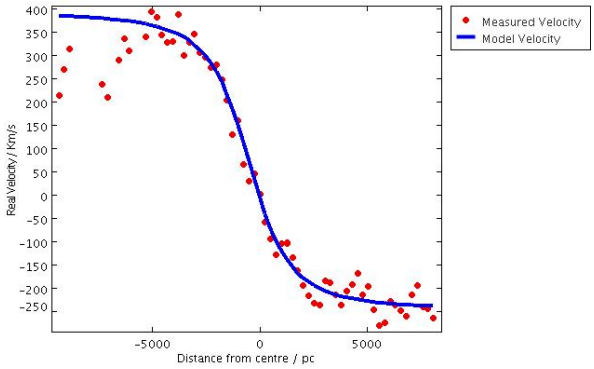

Fig. 7. rotation curve model fitting the deprojected velocities.

The deprojected velocities obtained with Eq. 6 were used to compute the mass of the galaxy through Eq. 8.

$$M = \frac{R \times v^2}{G} \tag{8}$$

The value for the mass of NGC 7331 in a radius of 9kpc from the centre is 2×10^{41} kg, which means about $10^{11} M_\odot$. With the values of the parameters a, c_0 and p previously found, we were able to model the mass of the galaxy using Eq. 9 (see Figure 8).

$$M(r) = \frac{r}{G} v_c^2(r) = \frac{a^2 r^3}{G(r^2 + c_0^2)^p} \tag{9}$$

4. Results

We studied the kinematic of gas in the galaxy NGC 7331.

We measured the wavelength of the Hαemission line at different positions along the slit, and where it was not possible, we used the [N II] emission line. We computed the redshifts for every position taken into account in order to find the rotational velocities, which had to be deprojected. then, we built the rotation curve of the galaxy and computed the mass of the galaxy within a radius of 9 kpc. We obtained a mass of about $10^{11} M_\odot$, in agreement with the value of mass of $8 \times 10^{10} M_\odot$ in a 10 Kpc radius found by Rubin et al. (1964).

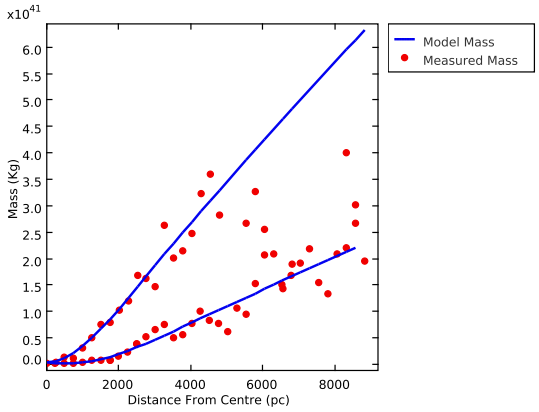

Fig. 8. Comparison between model and measured mass.

As far as velocities are concerned, we found an asymmetric rotation curve. This could be due to a particular distribution of the mass inside the galaxy itself.

References

Cini, D., Coppola, M., Derossi, C., Lappon, E., Stellar kinematics in NGC 7331: velocity dispersion and bulge mass, The Sky As a Laboratory, 2012

Materne, J., Tammann, G.A., The NGC 7331 Group, a stable group of galaxies projected on Stephan's Quartet, 1974, A&A, 35, 441

Rubin, V.C., Burbidge, E.M., Burbidge, G.R., Crampin, D.J., Prendergast, K.H., The rotation and mass of NGC 7331, 1965, ApJ, 141, 759

Wikipedia, http://en.wikipedia.org/wiki/

Index

Spectral classification of stars in the open cluster NGC 2420	p.	1
Temperature of the stars in the open cluster NGC 2420	p.	5
Photometric determination of the age and the distance of the open cluster NGC 2420	p.	9
Photometric analysis of the globular cluster NGC 5272	p.	15
Spectroscopic analysis of the planetary nebula NGC 7009	p.	19
Spectroscopic anaysis of the planetary nebula NGC 7662	p.	27
Spectroscopy of the planetary nebula NGC 7354	p.	33
The morphology of galaxy NGC 2768	p.	39
The morphology of galaxy NGC 2768	p.	43
Morphological analysis of spiral galaxy NGC 7331	p.	49
Stellar kinematics in NGC 7331: velocity dispersion and mass of the bulge	p.	55
Kinematics of gas in NGC 7331	p.	61